Pontifícia Universidade Católica
do Rio de Janeiro

Caio Filippo Ramalho Leite

Numerical Study of Spark-Assisted Compression Ignition Engines (SACI)

Dissertação de Mestrado

Dissertation presented to the Programa de Pós-Graduação em Engenharia Mecânica of PUC-Rio in partial fulfillment of the requirements for the degree of Mestre em Engenharia Mecânica.

Advisor : Prof. Sergio Leal Braga
Co-advisor: Prof. Florian Alain Yannick Pradelle

Rio de Janeiro
October 2021

Pontifícia Universidade Católica
do Rio de Janeiro

Caio Filippo Ramalho Leite

Numerical Study of Spark-Assisted Compression Ignition Engines (SACI)

Dissertation presented to the Programa de Pós-Graduação em Engenharia Mecânica of PUC-Rio in partial fulfillment of the requirements for the degree of Mestre em Engenharia Mecânica. Approved by the Examination Committee:

Prof. Sergio Leal Braga
Advisor
Departamento de Engenharia Mecânica – PUC-Rio

Prof. Florian Alain Yannick Pradelle
Co-advisor
Departamento de Engenharia Mecânica – PUC-Rio

Prof. José Alberto dos Reis Parise
Departamento de Engenharia Mecânica – PUC-Rio

Prof. José Eduardo Mautone Barros
Departamento de Engenharia Mecânica – UFMG

Rio de Janeiro, October 4th, 2021

Caio Filippo Ramalho Leite

Caio Leite graduated in mechanical engineering in 2020 from Pontifícia Universidade Católica do Rio de Janeiro (PUC-Rio) as well as in engineering from École Centrale Paris (CentraleSupélec) in Paris, France. Currently, he is a student researcher at the Instituto Tecnológico PUC-Rio (PUC-Rio) in the field of energy and combustion.

Bibliographic data

Leite, Caio Filippo Ramalho

Numerical Study of Spark-Assisted Compression Ignition Engines (SACI) / Caio Filippo Ramalho Leite; advisor: Sergio Leal Braga; co-advisor: Florian Alain Yannick Pradelle. – 2021.

151 f: il. color. ; 30 cm

Dissertação (mestrado) - Pontifícia Universidade Católica do Rio de Janeiro, Departamento de Engenharia Mecânica, 2021.

Inclui bibliografia

1. Engenharia Mecânica – Teses. 2. Motor de Ignição por Compressão Assistida por Centelha (SACI). 3. Modelagem de motor. 4. Gás Natural. 5. Planejamento Composto Central (CCD). I. Braga, Sergio Leal. II. Pradelle, Florian Alain Yannick. III. Pontifícia Universidade Católica do Rio de Janeiro. Departamento de Engenharia Mecânica. IV. Título.

CDD: 621

To my wife Beatriz and to my family,
for their support and encouragement.

Acknowledgments

To my wife, Beatriz, for her friendship, support, patience, generosity, and attention throughout the entire Master course.

To my parents, João Jorge and Simone, my brothers Hugo - and its fiancée Gabriela - and André, and my great friend and "second mother" Sônia for their support, encouragement, and companionship.

To my adviser professor Sergio Leal Braga for his ideas, confidence, and teaching since the beginning of this research.

To my co-adviser professor Florian Alain Yannick Pradelle for his dedication, attention, guidance, and friendship at all times.

To the Instituto Tecnológico (ITUC), PUC-Rio, and the ITUC team for the material support, attention, and ideas for solving the problems faced.

To all my friends for being always there for me: to listen, to advise, to work, to laugh.

To CAPES for its essential support in the development of this research. This study was financed in part by the Coordenação de Aperfeiçoamento de Pessoal de Nível Superior - Brasil (CAPES) - Finance Code 001.

To professor José Alberto dos Reis Parise and professor José Eduardo Mautone Barros for their advice that led to the final version of this document.

Abstract

Leite, Caio Filippo Ramalho; Braga, Sergio Leal (Advisor); Pradelle, Florian Alain Yannick (Co-Advisor). **Numerical Study of Spark-Assisted Compression Ignition Engines (SACI)**. Rio de Janeiro, 2021. 151p. Dissertação de Mestrado – Departamento de Engenharia Mecânica, Pontifícia Universidade Católica do Rio de Janeiro.

In the last few years, the automotive industry has reinvented itself to meet the demands of the international market, which has been increasingly competitive in a context with environmental laws each year more severe. One alternative to lower harmful greenhouse gases emissions over the life of the vehicle is electric cars. However, the production and disposal of electric batteries is still a major problem to be solved. Therefore, companies are also searching for other potentialities to increase the internal combustion engine's efficiency and develop green technology, such as Homogeneous Charge Compression Ignition (HCCI) or Spark-Assisted Compression Ignition (SACI). A MATLAB routine was created to predict the performance of SACI multi-mode combustion of natural gas using a two-zone thermodynamic model. This work performs sensitivity analysis for five performance parameters: thermal efficiency (η_{th}), indicated mean effective pressure (IMEP), NOx emissions, mean in-cylinder temperature ($\overline{T}_{avg}$), and auto-ignition timing (AIT), with several variables such as engine speed (RPM), fuel-air equivalence ratio (ϕ), spark timing (θ_s), compression ratio (r_c), and intake pressure (P_{int}), using the design of experiments tools to assess the factors' impact. The Central Composite Design indicates that RPM and ϕ were the most important SACI factors since they influence all engine performance parameters. The P_{int} was significant in three performance parameters (η_{th}, IMEP and $\overline{T}_{avg}$), as was θ_s (NOx, $\overline{T}_{avg}$ and AIT). The r_c, however, was relevant in only one of them (AIT). Furthermore, a Univariate Analysis (UA) was done to compare Spark-Ignition (SI) and SACI engines. The results show that SACI engines tend to be around 9% more efficient, NOx emissions drop notably, more than 90%, IMEP presents an increase of 76%, and $\overline{T}_{avg}$ decreases 200-300 K.

Keywords

Spark-Assisted Compression Ignition (SACI); Engine modeling; Natural Gas; Central Composite Design (CCD).

Resumo

Leite, Caio Filippo Ramalho; Braga, Sergio Leal; Pradelle, Florian Alain Yannick. **Estudo Numérico dos Motores à Ignição por Compressão Assistida por Centelha (SACI)**. Rio de Janeiro, 2021. 151p. Dissertação de Mestrado – Departamento de Engenharia Mecânica, Pontifícia Universidade Católica do Rio de Janeiro.

Nos últimos anos, a indústria automotiva se reinventou para atender às demandas do mercado, que tem se mostrado competitivo em um contexto com legislações ambientais severas. Uma alternativa para reduzir as emissões de gases de efeito estufa prejudiciais ao longo da vida do veículo são os carros elétricos. No entanto, a produção e o descarte de baterias elétricas ainda é um problema a ser resolvido. Por isso, as empresas também buscam alternativas para aumentar a eficiência do motor de combustão interna e desenvolver tecnologias verdes, como a Ignição por Compressão de Carga Homogênea ou a Ignição por Compressão Assistida por Centelha (SACI). Uma rotina MATLAB foi criada para prever o desempenho da combustão SACI de gás natural usando um modelo termodinâmico de duas zonas. Este trabalho realiza análise de sensibilidade para cinco parâmetros de desempenho: eficiência térmica (η_{th}), pressão efetiva média indicada (IMEP), emissões de NOx, temperatura média no cilindro ($\overline{T}_{avg}$) e tempo de autoignição (AIT), com várias variáveis como a velocidade do motor (RPM), a razão de equivalência combustível-ar (ϕ), o tempo da centelha (θ_s), a razão de compressão (r_c) e a pressão de admissão (P_{int}), usando planejamento de experimentos para avaliar o impacto dos fatores. O Planejamento de Composto Central indica que o RPM e o ϕ foram os fatores mais importantes no SACI, uma vez que influenciam todos os parâmetros de desempenho. A P_{int} foi significativa em três parâmetros de desempenho (η_{th}, IMEP e $\overline{T}_{avg}$), assim como o θ_s (NOx, $\overline{T}_{avg}$ e AIT). A r_c foi relevante em apenas um deles (AIT). Além disso, uma Análise Univariada foi feita para comparar as técnicas de ignição por centelha (SI) e SACI. Os resultados indicam que os motores SACI tendem a ser cerca de 9% mais eficientes e as emissões de NOx caem mais de 90%.

Palavras-chave

Motor de Ignição por Compressão Assistida por Centelha (SACI); Modelagem de motor; Gás Natural; Planejamento Composto Central (CCD).

Table of contents

List of figures

List of tables

Nomenclature

Acronyms

AIT	Auto-Ignition Timing
aBDC	After Bottom Dead Center
aTDC	After Top Dead Center
bBDC	Before Bottom Dead Center
BDC	Bottom Dead Center
BEV	Battery Electric Vehicle
bTDC	Before Top Dead Center
CAD	Crank Angle in Degrees
CI	Compression Ignition
EVC	Exhaust Valve Opens
EVO	Exhaust Valve Closes
FCEV	Hydrogen-based Fuel Cell Electric Vehicle
GHG	Greenhouse Gases
HCCI	Homogeneous Charge Compression Ignition
HEV	Hybrid Electric Vehicle
HRR	Heat Release Rate
ICE	Internal Combustion Engine
ICEV	Internal Combustion Engine Vehicle
IMEP	Indicated Mean Effective Pressure (kPa)
IVC	Intake Valve Opens
IVO	Intake Valve Closes
SACI	Spark-Assisted Compression Ignition
SI	Spark Ignition
SI-HCCI	Spark Ignition - Homogeneous Charge Compression Ignition
SICI	Spark-Induced Compression Ignition
SPCCI	Spark Controlled Compression Ignition
TDC	Top Dead Center
UHC	Unburned Hydrocarbon

Symbols

A	$[m^2]$	Cylinder lateral area
a_W	$[-]$	Wiebe efficiency factor
a_{AI}	$[-]$	Auto-ignition "a" coefficient
B	$[m]$	Cylinder bore
b_{AI}	$[K]$	Auto-ignition "b" coefficient
c_p	$[kJ/(kg.K)]$	Specific heat capacity at constant pressure
C_1 *and* C_2	$[-]$	Woschni constants

Ea_{AI}	$[J/mol]$	Auto-ignition activation energy coefficient
h	$[kJ/kg]$	Specific enthalpy
KI	$[-]$	Knock-integral
L	$[m]$	Connecting-rod length
MW	$[kg/kmol]$	Molecular weight
m	$[kg]$	In-cylinder mass
m_W	$[-]$	Wiebe form factor
N_{cyl}	$[-]$	Number of cylinders
Nu	$[-]$	Nusselt number
n	$[mol]$	Amount of substance
n_{AI}	$[-]$	Auto-ignition "n" coefficient
P	$[kPa]$	In-cylinder pressure
P_{int}	$[kPa]$	Pressure at the intake manifold
R	$[m]$	Crank radius
Re	$[-]$	Reynolds number
r	$[kJ/(kg.K)]$	Specific gas constant
r_c	$[-]$	Compression ratio
S	$[m]$	Cylinder stroke
$\overline{S_p}$	$[m/s]$	Mean piston speed
s	$[kJ/(kg.K)]$	Specific entropy
T	$[K]$	Temperature
t	$[s]$	Time
u	$[kJ/kg]$	Specific internal energy
v	$[m^3/kg]$	Specific volume
V	$[m^3]$	Cylinder volume
V_{BDC}	$[m^3]$	Bottom Dead Center volume
V_d	$[cm^3]$	Displacement volume
V_d^{tot}	$[cm^3]$	Total displacement volume
V_{TDC}	$[m^3]$	Top Dead Center volume
x	$[-]$	Mass fraction
w	$[m/s]$	Average cylinder gas velocity
y	$[-]$	Molar fraction

Greek letters

α	$[W/(m^2.K)]$	Heat transfer coefficient
γ	$[-]$	Heat capacity ratio
ϵ	$[-]$	Half-stroke to rod ratio
η	$[-]$	Efficiency
θ	$[^\circ]$	Crank angle
ξ	$[-]$	Nitric oxide concentration to its equilibrium value ratio
τ	$[s]$	Auto-ignition delay time
ϕ	$[-]$	Fuel-air equivalence ratio
ω	$[rad/s]$	Angular velocity
ζ	$[-]$	Extent of precursor reaction

Subscripts and superscripts

amb	Ambient
avg	Average
b	Burned gas
c	Critical
d	Combustion duration
exh	Exhaust
int	Intake
IVC	Intake Valve Closing
m	Motored
p	Precursor
s	Start of combustion
tot	Total
th	Thermal
u	Unburned gas
v	Volumetric
W	Wiebe function

"Crowns have their compass; length of day, their date;
Triumphs, their tomb; felicity, her fate;
Of nought but earth can earth make us partaker,
But knowledge makes a king most like his Maker."

William Shakespeare

1
Introduction

1.1
The Climate Issue

Since the ancient Greeks, many people had proposed that humans have an influence on their surroundings. It was thought that chopping down trees, plowing fields, or irrigating a desert, would change temperatures and influence rainfall. Accurate or not, those perceived climate effects were merely local. The idea that humans could somehow alter climate on a global scale would seem unreal for centuries. In the nineteenth century, however, some scientists started to study the effects of gases in the atmosphere and how they could absorb and reflect wavelengths of sunlight. At the end of the that century, Svante Arrhenius, a Swedish chemist, investigated the influence of different concentrations of CO_2 in the atmosphere. He calculated that doubling the CO_2 in the atmosphere would raise the Earth's temperature by 5-6°C. Although the majority of scientists at the time did not give credit to his predictions, modern climate modeling confirms that Arrhenius' numbers were not far from reality (WEART, 2008).

The year 1988 would be the turning point for the global warming discussion when it was first placed in the spotlight. Global temperatures had been increasing for almost a decade and the summer of 1988 was the hottest ever recorded at the time. The United States also saw widespread drought and wildfires. The media and the public start paying attention to the scientists' alarms and the news of climate change started to travel. NASA scientist James Hansen presented models to congress in June of 1988, saying he was "99 percent sure" that global warming had arrived (HISTORY, 2017).

Then, the World Meteorological Organization (WMO) and the United Nations Environment Programme (UNEP), created the Intergovernmental Panel on Climate Change (IPCC) whose objective is to provide governments at all levels with scientific information that they can use to develop climate policies. From its foundation, the IPCC has led more than 52 international sessions to discuss climate change, arranging agreements for emissions reduction (I.e., 1997's Kyoto Protocol and 2015's Paris Climate Agreement), and underlining the problem of climate change (UNFCCC, 2015).

1.2 Worldwide Energy Consumption

Despite the rise of global warming awareness, climate change problems are far from over. Energy production of all types accounts for 72 percent of all emissions. Globally, the primary sources of greenhouse gas emissions are electricity and heat (31%), agriculture (11%), transportation (15%), forestry (6%), and manufacturing (12%) (WRI, 2017). As the population grows and energy becomes a necessary part of human life, worldwide energy consumption tends to increase every year. Figure 1.1, from the Annual Energy Outlook 2021 (AEO 2021), indicates the history of the world energy consumption by end-use sector. Besides the effects of pandemics in 2020, one can notice that the transportation sector accounts for 25% of the world's energy consumption.

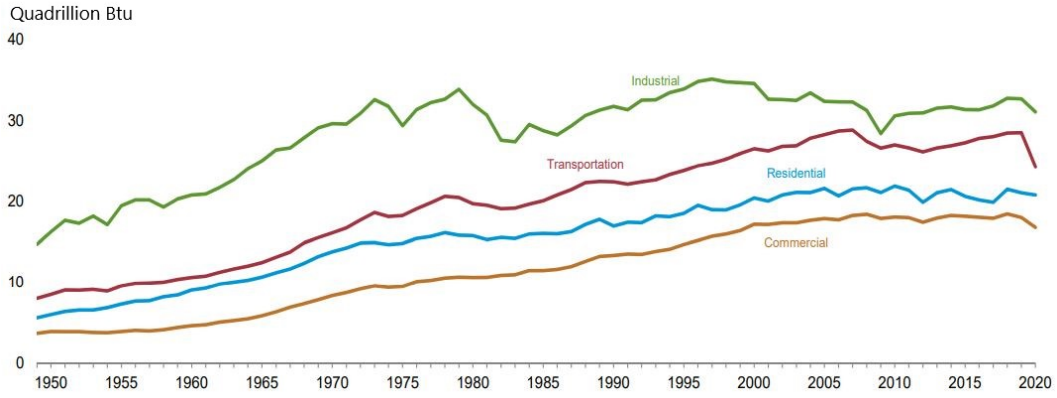

Figure 1.1: World energy consumption by sector from 1949 to 2020 (EIA, 2021).

To generate the energy required fuels must be used. And although nowadays the world is more sensitive to sustainable development, there is still a long way to reach it. The same study shows that the most common fuels used in the transportation sector are petroleum (80%), renewable energy (11%), and natural gas (7%), Figure1.2. The energy produced by renewables is growing fast, but projections estimate that petroleum and natural gas will remain in the lead for, at least, the next 30 years (EIA, 2021).

Considering that 25% of the world's energy consumption comes from the transportation sector and that 80% of it is petroleum, one can say that 20% of the energy consumption worldwide is for transport engines. Moreover, motor gasoline being 42% of the petroleum usage in the transportation sector, represents 8.4% of global energy consumption in gasoline engines. These numbers display the impact of internal combustion engines (ICE) in the world's energy matrix and explain the motivations behind the rigid government policies for ICEs and the research for future technologies.

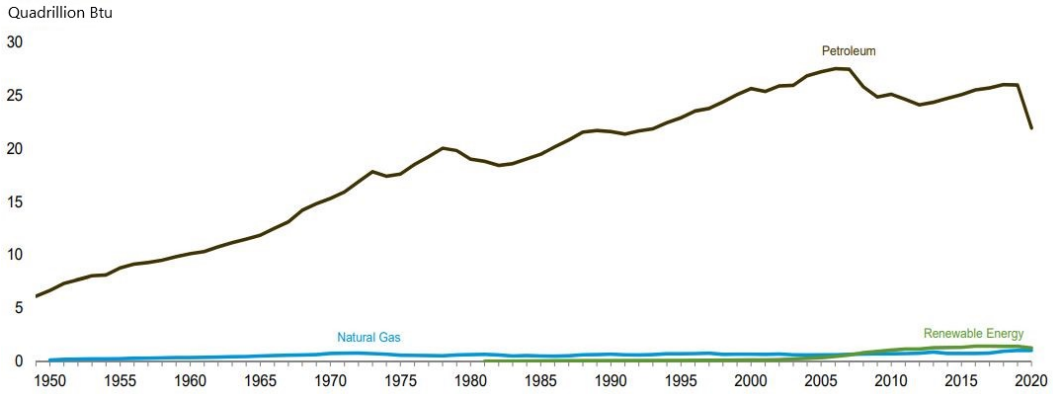

Figure 1.2: World's transportation sector consumption by source from 1949 to 2020 (EIA, 2021).

Figure 1.3, from the World Energy Outlook 2020, exhibits the world energy demand by fuel. The same behavior is seen on the graph: oil is the most used fuel in energy production. These data reinforce the world necessity of research in renewable energies for the future (IEA, 2020).

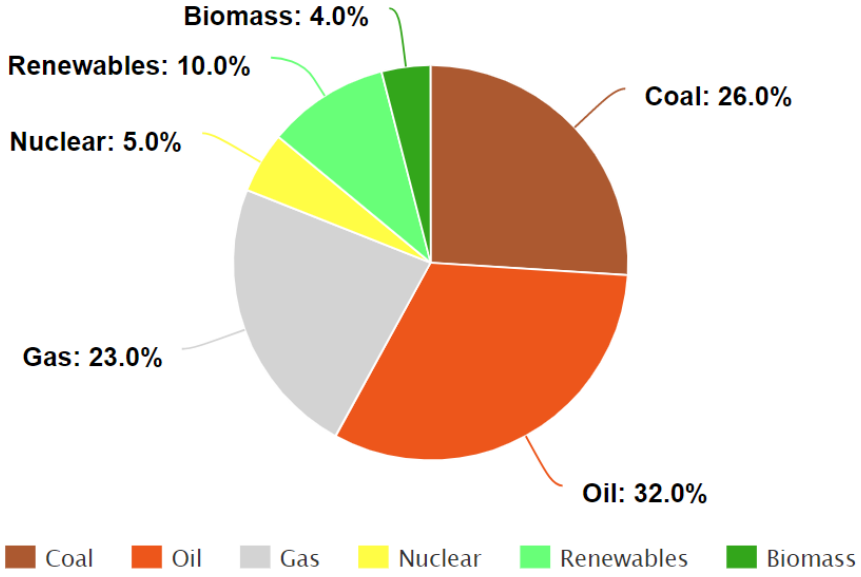

Figure 1.3: World energy demand by fuel in 2019 (IEA, 2020).

When it comes to the major fuel used in the domestic energy supply, Brazil functions similarly to other countries: with petroleum and its oil products accounting for 34% of its domestic energy supply. However, the Brazilian energy matrix is very distinct from the rest of the world. As Figure 1.4 shows, the second most used fuel in Brazil, even more than natural gas, is the sugarcane product, which is responsible for 18% of all energy supply in the country.

It is noteworthy that 82.9% of the electric energy produced in Brazil

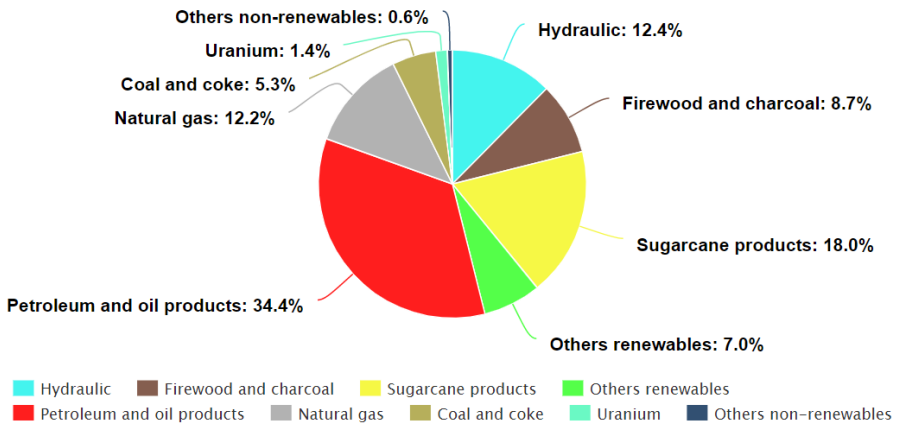

Figure 1.4: Brazil's domestic energy supply in 2019 (EPE, 2020).

proceeds from renewables. It is one of the greener electric matrices of the world. A study made by the EPE (*Empresa de Pesquisa Energética*) in 2020, Figure 1.5, demonstrates that the percentage of renewable used for domestic energy supply in Brazil is three times bigger than in the rest of the world (EPE, 2020).

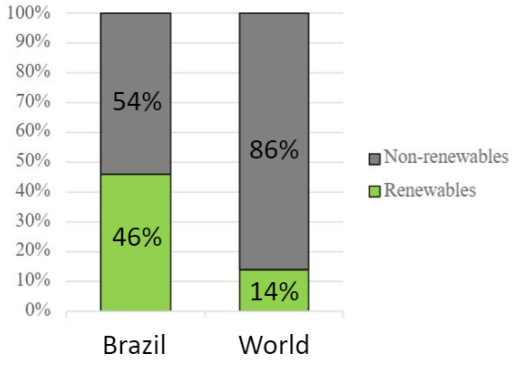

Figure 1.5: Brazil's renewables compared to the world in 2019 (EPE, 2020).

Since the worldwide fuel crisis of the 1970s, the Brazilian government has been searching for alternatives forms of energy production. That's the reason why it is considerably advanced in sugarcane products and hydraulic power (UNTV, 2008).

The research for a low-carbon economy is a major concern of the modern world. Brazil continues to look for other sustainable ways to make its energy matrix even greener. Looking at the non-renewable fuel with the most impact in the country, one sees, as presented in Figure 1.6, that it is used primarily for the transportation sector, exactly how it happens in the rest of the world.

New technologies in the transport sector that can minimize gas emissions and contribute to the world's low-carbon agenda are a subject that will have a great impact in the upcoming future. Studying the new method of combustion

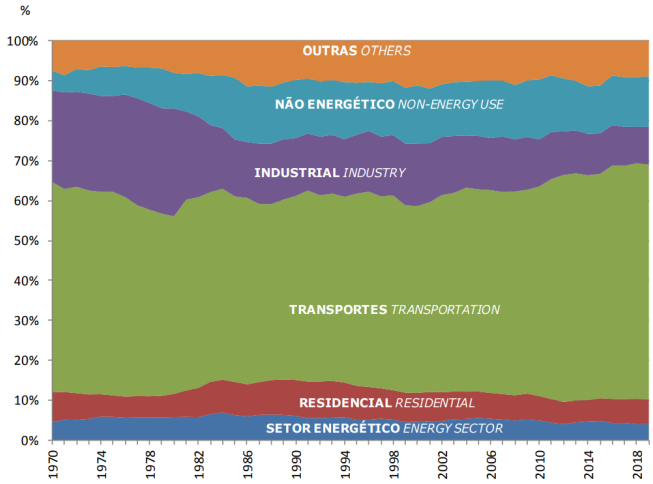

Figure 1.6: Brazil's oil consumption by sector in the period 1970-2019 (EPE, 2020).

in ICEs with natural gas and biofuels, like ethanol, in which Brazil has already production and distribution expertise, is a strategy that countries can adopt in the short and mid-term to reduce pollutants for the next decades.

A program called *RenovaBio* was launched in December 2016 by the Ministry of Mines and Energy (MME) to help Brazil meet its commitments under the COP21 Paris Agreement, as well as contributing to the reduction of GHG emissions in the production, commercialization, and use of biofuels. It also promotes the expansion of the production and use of biofuels in the national energy matrix, emphasizes the fuel supply's continuity, and contributes to the predictability of various biofuels in the national fuel market (BARROS, 2021).

1.3 Electric Vehicles as the Green Solution

Battery electric vehicles (BEVs) are today's most promising technology to substitute internal combustion engine vehicles (ICEVs). Many governments have announced the desire to eventually ban ICEVs shortly, leading to the belief that all transport can and will be powered only by electricity and that the ICE would quickly disappear (ECONOMIST, 2017). However, the world demand for transport energy and the commercial projections of vehicles' expansion in countries like China and India (EXXONMOBIL, 2017) makes one wonder if this massive and increasing demand could be met entirely by powertrains that do not rely on combustion.

The future of the transport energy sector is determined by an intricate interplay between many drivers, as shown in Figure 1.7. These depend on

political, energetic, and regional players, which are different all over the world. Even though predictions are complex in those contexts, projections suggest that even by 2050 around 80% of the transport energy will come from combustion engines powered by petroleum (WEC, 2017).

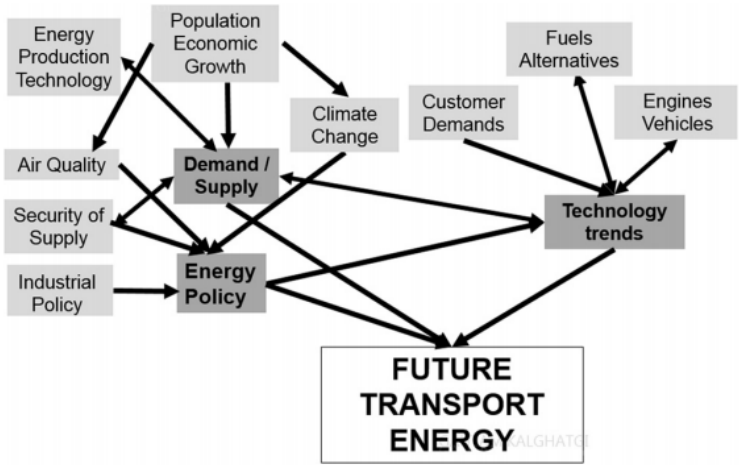

Figure 1.7: The complex interplay between drivers for the future of the transport energy sector (KALGHATGI, 2018).

BEVs produce no carbon dioxide (CO_2), carbon monoxide (CO), nitrogen oxides (NO_x), unburned hydrocarbons (UHCs), and particulates at the tailpipe. So, the impact of BEVs on GHG depends entirely on how the electricity used to power the BEV is produced (MA et al., 2012). In China and India, where transport energy demand grows faster than elsewhere, coal plays an important role in electricity generation, permitting carbon intensity to be high. We can recall that India recently reiterated that coal will continue to produce roughly three-quarters of India's electricity for decades to come (MATHIESEN, 2017). In China, GHG emission from BEVs' production is 50% higher than that for a comparable ICEV (QIAO et al., 2017).

In areas where coal, or another pollutant fuel, is a big part of the energy matrix, BEVs can have a higher emission impact than similar ICEVs. Thus, it is better to promote full-Hybrid Electric Vehicles (HEVs) than BEVs until the power sector is sufficiently decarbonized. In this type of vehicle, all the energy comes from an ICE, and the battery and an electric motor manage the energy flow, enabling it to run more efficiently (HAWKINS et al., 2013).

Finally, to allow BEVs to be a part of the future, the infrastructure of the transport sector will have to change entirely. The extra demand for electricity from BEVs is often met from a marginal generation, which can respond quickly to changing demand. It usually comes from fossil fuels – since solar is not available at night, and wind and hydro-power output cannot be changed at will. Furthermore, full electrification impacts directly on the power sector's

charging infrastructure, and materials needed for battery production are concentrated primarily in China, making the future of BEVs also geopolitical (KALGHATGI, 2018).

The bars to the left in Figure 1.8 show how different means of electricity production give altered Well-to-Wheel GHG emissions for the BEV category. It is clear that carbon-intensive electricity production results in strikingly higher emissions than renewable electricity, in this case represented by wind energy (NORDELöF et al., 2014).

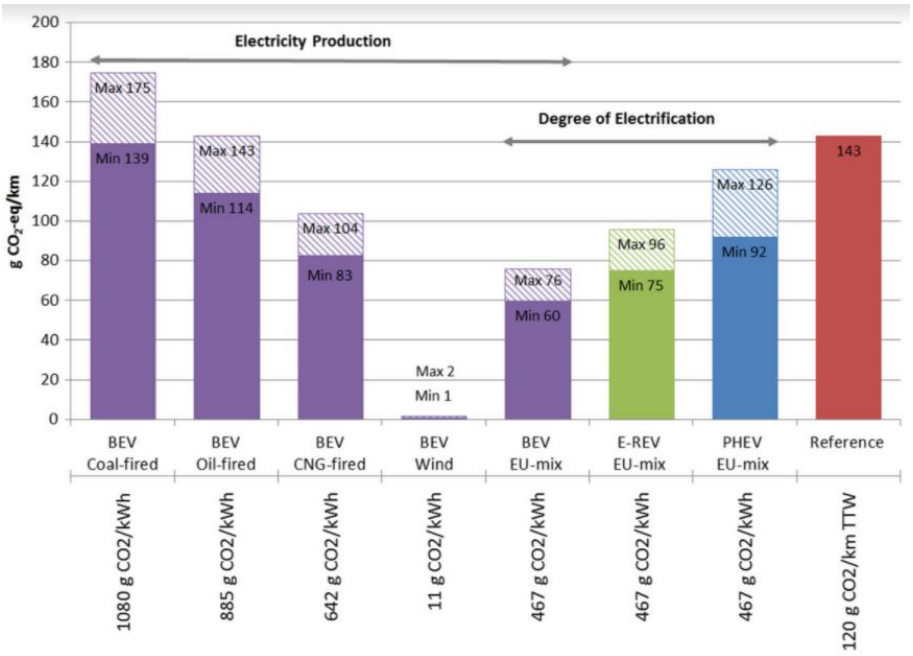

Figure 1.8: Well-to-Wheel Analysis of GHG emissions for different electricity production and degrees of electrification vehicles. The reference vehicle corresponds to the 2012 EU fleet target for tailpipe emissions of sold cars (European Parliament 2008) (NORDELöF et al., 2014).

Because of plentiful supplies, convenience, and affordability, ICEs have been dominant in the transports of goods and people since the first half of the 20th century. Moreover, stationary ICEs are omnipresent in industries and in power generation facilities, which promote the world's standard of living. There are still no real alternatives that can compete with ICEs and the entire range of applications that they cover today (IJER, 2019).

Throughout the history of the ICE, researchers have been studying tirelessly to improve its efficiency. Nowadays, alongside the pursuit of maximum performance, the reduction of pollutant emissions is the point of great interest. Over the last four decades, in response to the climate change concerns, research on engine combustion, exhaust after-treatment, and controls has led to demonstrably cleaner energy with a 1000-fold reduction in exhaust emissions (particulates, NO_x, CO, and UHCs) (SAGE, 2019).

The preference for alternative low-carbon technologies to reduce the impact of transport in the atmosphere is still discussed to this day. The three main options are BEV, Hydrogen-based Fuel Cell Electric Vehicle (FCEV), and ICEV with decarbonized fuels. The disagreement between the supporters of each one of these solutions is due to their uncertainties. A study made in Germany, mapping, characterizing, and comparing these three options shows that the uncertainty of each group is similar, making the choice of only one of them unjustified. That's why all options should advance alongside each other now to avoid lock-in decisions (WANITSCHKE; HOFFMANN, 2020).

Future mobility will likely be characterized by a mix of solutions, involving BEVs, HEVs, FCEVs, and ICEVs, depending on consumer acceptance (e.g., cost) and its application (city, country, personal, freight, etc.). In the next decades, the combustion engine will still play a central role, whether used for power generation or for powering the vehicle itself, even in strongly electrified powertrain configurations. Because of this, there is great interest in improving its' thermal efficiency and reducing GHG emissions without significant increases in the purchase and operating costs in the short-to-medium term. These goals can be achieved in many ways. The most promising ones are improvements in combustion, after-treatment and control systems, and electrification in the form of hybridization, together with vehicle weight reduction and more efficient ancillary systems (IJER, 2019).

1.4 The Spark-Assisted Compression Ignition Engine

Internal combustion engines are best known for two forms of combustion: Spark Ignition engines (SI) and Compression Ignition engines (CI). These operate with the cycles designed by Nikolaus Otto and Rudolf Diesel, respectively, which are the most used combustion techniques for ICEs. For this reason, they are also called Otto and Diesel-cycle engines (OBERT, 1971).

In the last few years, a new form of combustion has been widely studied and is now present in the automotive industry. This technology is called Homogeneous Charge Compression Ignition (HCCI). HCCI engines combine characteristics of both SI and CI, trying to profit from the best aspects of each. In these engines, the air-fuel mixture enters the cylinder at the intake stroke (as in SI engines), then it is compressed until a major part of it has the exact conditions of pressure and temperature to enter compression ignition (auto-ignition) at the Top Dead Center (TDC), as illustrates Figure 1.9. At this moment, all homogeneous mixture ignites spontaneously, accelerating combustion and resulting in higher pressure inside the cylinder. This condition

favors the work of the piston and increases thermal efficiency. Besides, HCCI engines work with lean mixtures, leading to a lower mean mixture temperature and, therefore, a decrease in NOx formation (FERGUSON; KIRKPATRICK, 2016).

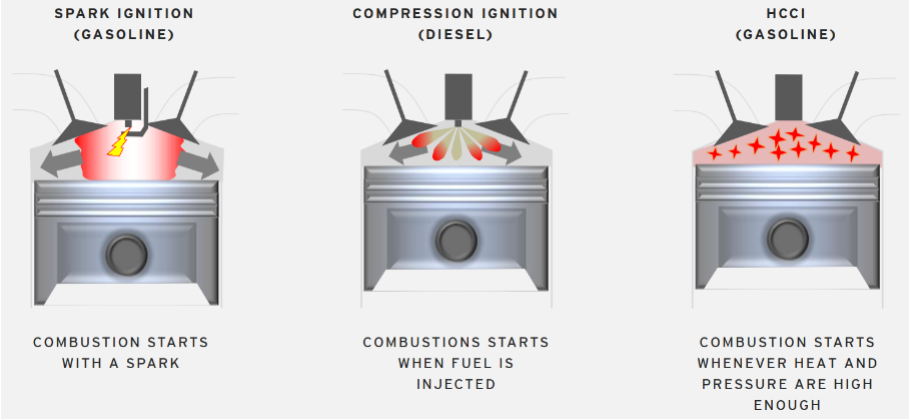

Figure 1.9: The difference between SI, CI and HCCI combustions (MAZDA, 2019).

The HCCI technology brings the best of both worlds: fast ignition, higher compression ratio and greater efficiency (compared to CI engines), and lower emission of pollutants (compared to SI engines). However, HCCI engines are sensitive to operating conditions, and their best performance is obtained in a narrow range of conditions. If the air-fuel mixture ignites spontaneously before the TDC as desired to achieve greater efficiency, the phenomenon of knock occurs. This event is harmful to the engine parts and causes high amounts of negative work, dropping efficiency substantially. On the other hand, if the air-fuel mixture does not reach the thermodynamic state necessary for auto-ignition, there is a misfire: combustion does not occur, and the admitted fuel is wasted (HAIRUDDIN; WANDEL; YUSAF, 2014).

Aiming for better control of the auto-ignition in HCCI engines, the Spark-Assisted Compression Ignition (SACI), also called Spark Controlled Compression Ignition (SPCCI) by Mazda Motor Company, was born. It uses both types of combustion, being called SI-HCCI combustion, and works as follows: at the final of the compression stroke, when the air-fuel mixture is already close to the auto-ignition condition, a spark is released, causing the air-fuel mixture to ignite in the spark-plug surroundings, and creating a flame-front that propagates in the cylinder (SI combustion). The burned gases raise the engine pressure so that, after a small increment, the unburned gases have sufficient pressure and temperature to ignite spontaneously (HCCI combustion). Figure 1.10 displays the SACI (SPCCI) combustion technology present in Mazda's *SkyActiv-X* engine (MAZDA, 2019).

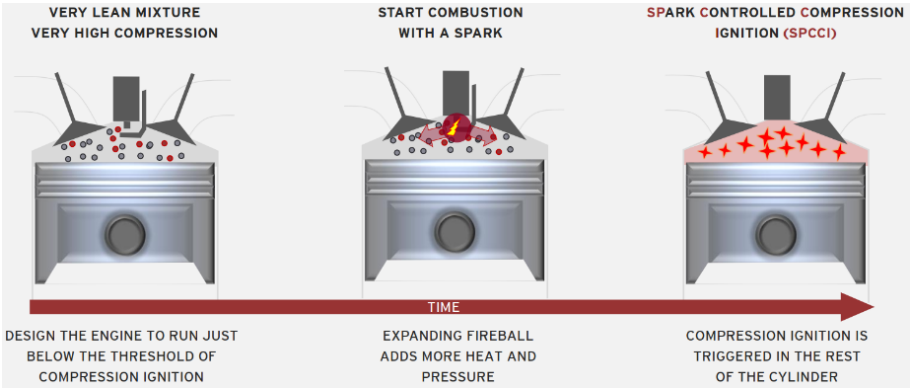

Figure 1.10: Schematic representation of the SACI combustion (MAZDA, 2019).

The spark-ignition (start of combustion) controls the HCCI combustion time, making it possible to operate in different regimes, increasing engine efficiency, and decreasing gas emissions. These engines are also capable to run with common fuels/biofuels and could be adopted as a short-term solution to reduce emissions as well as equipped with batteries to function in HEV in the mid-term (ORTIZ-SOTO et al., 2019).

1.5 Objectives

The present thesis has the objective of investigating the Spark-Assisted Compression Ignition engine with natural gas as fuel. Thus, we will develop a two-zone thermodynamic 0D simulator that can operate with multiple combustion methods (SI, CI, HCCI, and SACI) and different fuels at brief simulation time. This program will assist us in understanding the engine's key performance parameters, i.e., thermal efficiency, indicated mean effective pressure, NOx emissions, mean in-cylinder temperature, and auto-ignition timing.

We will variate, for this study, the engine speed, the fuel-air equivalence ratio, the spark timing, the compression ratio, and the intake pressure. A Matlab routine with numerous variables makes the engine's performance and emission studies possible and easy and can be a powerful tool in innovative engineering pre-projects.

Good SACI performance parameters in this simulator would justify the application of this engine in the short and mid-term as a substitute for gasoline engines. It would promptly reduce air pollution and gain time for the study and development of other long-term green strategies, such as BEVs and their infrastructure, and FCEVs.

For this, this work has four specific goals:

1. Prediction of the SACI engine classic parameters: Indicated Mean Effective Pressure (IMEP), Maximum Indicated Pressure, Maximum Power, Heat Release, Heat Release Rate (HRR), Emissions, etc.

2. Comparision with SI, CI, and HCCI engines in therms of thermal efficiencies, mean effective pressure profiles, mean temperature, NOx emissions, and combustion duration.

3. Use of design of experiments to map the optimal SACI operating points.

1.6 Organization of the Thesis

A bibliographic review about SACI engines technology is presented in Chapter 2, underlining the differences between its combustion and the ones from SI, CI, and HCCI engines. The impact of some parameters of this type of engine is also accessed for further comparisons.

In Chapter 3, the modeling of the SI, HCCI, and SACI engines is presented. The hypothesis adopted, and the thermodynamic and chemical approaches for each of the four strokes are discussed. The criterion for the auto-ignition and the combustion curve for SI-HCCI combustion is also proposed.

The calculation procedure and the examples analyzed are described in Chapter 4. In Chapter 5, the operating point's mapping is studied for optimized ICE systems with SACI vs. SI comparison. Thus, the SACI operation results are shown and discussed.

Finally, Chapter 6 provides the main conclusions of this work and suggests future research on the theme.

2
Literature Review

In this chapter, internal combustion engine technology is presented. Different types of engines and combustion techniques are discussed and the state-of-the-art studies in ICEs and, more particularly, in the SACI combustion are examined. The literature review is, then, employed to develop an accurate numerical model on Chapter 3.

2.1
Internal Combustion Engines

An engine is defined as a machine that converts other forms of energy into mechanical work, generating movement. Throughout mankind's history, several sources have been used to generate work, such as human strength, animal traction, water currents, wind power, and steam pressure. However, a combustion engine transforms thermal energy, released during the chemical reaction of a fuel, into mechanical energy. Therefore, an internal combustion engine is a combustion engine in which the fuel is burned inside the engine, in a combustion chamber.

Internal combustion engines first appeared in the 19th century and were soon adopted in preference to steam engines due to their versatility, efficiency, less weight per horsepower, fast initial operation, and the possibility of adapting to different machines (OBERT, 1971).

They are essentially composed of the following parts (FURLANI, 2006):

2.1.1
Engine block

The engine block is the largest part of the engine, which supports its other parts. It contains circular tubes for the passage of cooling water and lubricating oil, as shown in Figure 2.1.

It is usually made of cast iron to which other elements can be added in order to improve desired properties.

2.1.2
Cylinder head

The engine head, Figure 2.2, is the component that covers the upper part of the engine block. Being made of the same material as the engine block, it facilitates the maintenance of the engine, determines the shape of

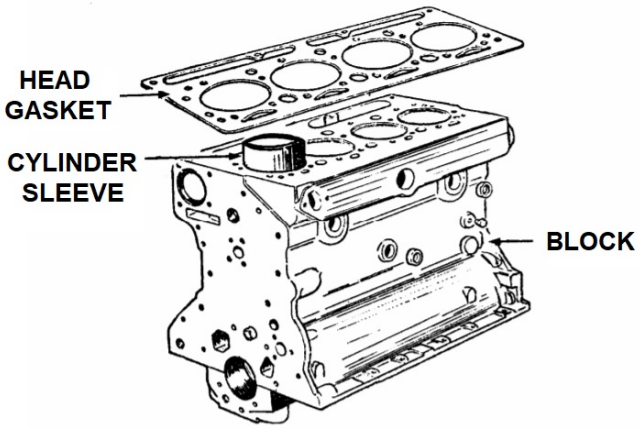

Figure 2.1: Engine block illustration (CBT, 1982).

the combustion chamber, and allows the passage of the intake and exhaust gases through the valves.

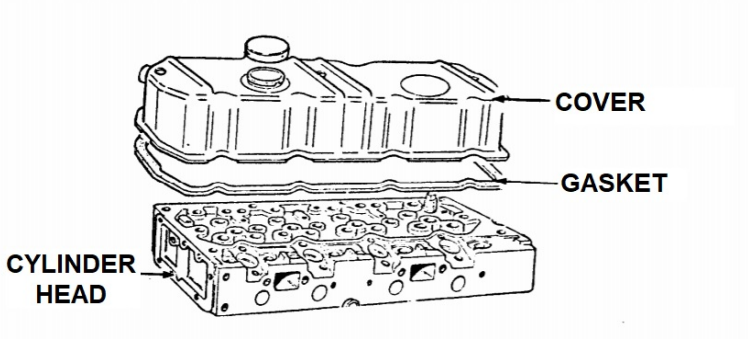

Figure 2.2: Cylinder head scheme (CBT, 1982).

Between the engine block and the cylinder head, there is a gasket to block the penetration of the air-fuel mixture, water, or oil into the adjacent circuits.

2.1.3 Crankcase

The crankcase, Figure 2.3, surrounds the lower part of the engine, housing the crankshaft and protecting the moving parts from foreign objects.

It also serves as a lubricating oil tank. It is made of a hard plate through the press forging process.

2.1.4 Piston

The piston is a cylindrical piece that moves inside the engine cylinders and is usually made of aluminum alloys, illustrated in Figure 2.4.

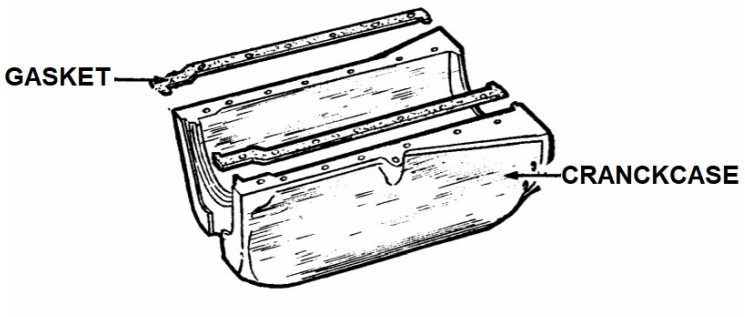

Figure 2.3: Crankcase drawing (CBT, 1982).

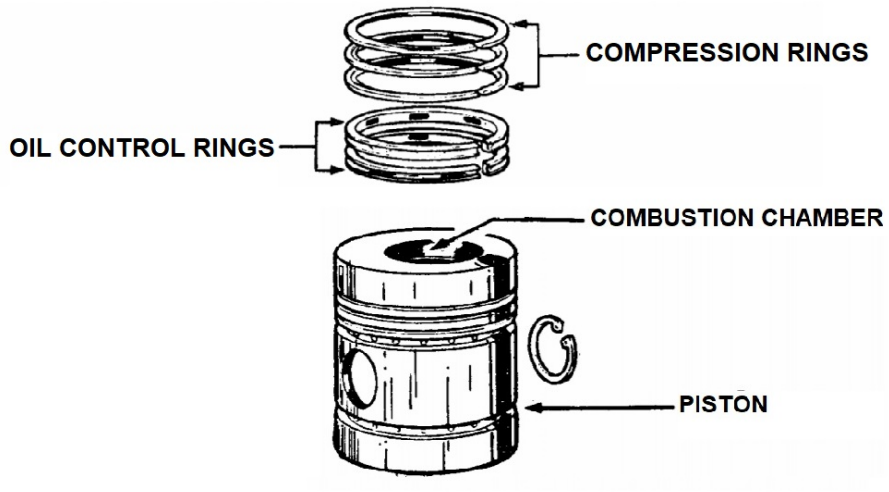

Figure 2.4: Piston elements (CBT, 1982).

It is the part that receives the compression and expansion of the gases and has a reciprocating motion. It contains two types of rings: the compression rings, for sealing the combustion chamber, and the oil control rings, for controlling the supply of oil to the cylinder wall, to lubricate itself and the piston skirt.

2.1.5 Connecting rod

The connecting rod, Figure 2.5, is the part of the engine that connects the piston to the crankshaft, transforming the linear movement of the piston into a rotational movement on the crankshaft.

It is made of forged steel and divided into three parts: the small end, the rod, and the big end. The small end is connected to the piston by a pin (made of case-hardened steel) and the big end is connected to the crankshaft using a bearing, an anti-friction material.

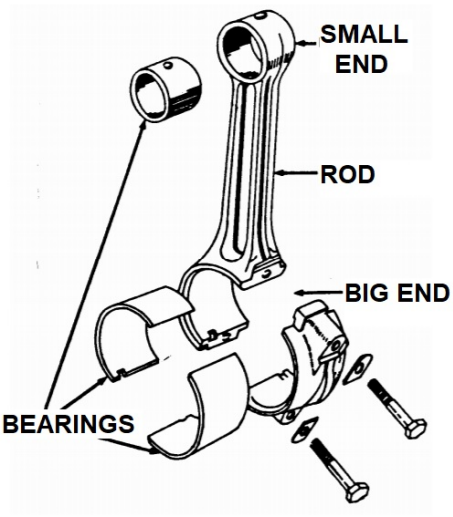

Figure 2.5: Connecting rod illustration (CBT, 1982).

2.1.6 Crankshaft

The crankshaft is the engine component that performs the conversion between the reciprocating motion of the piston and the rotational motion of the motor shaft, as shown in Figure 2.6.

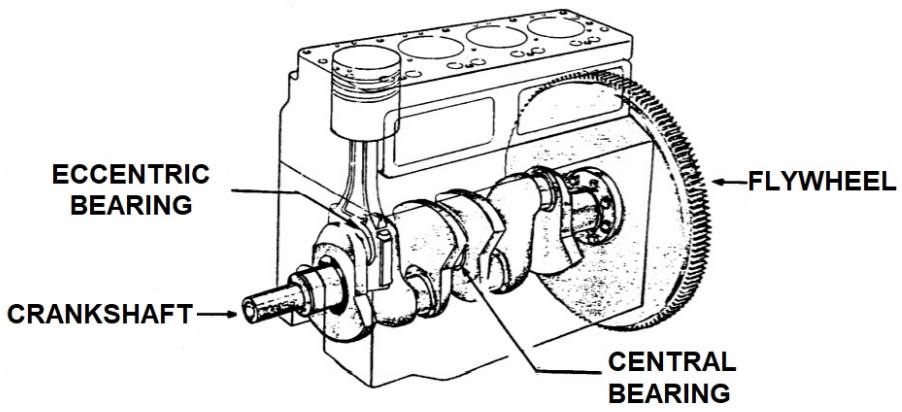

Figure 2.6: Crankshaft design (CBT, 1982).

It is connected to the foot of the connecting rods and has two types of bearings: the center ones, which support the crankshaft to the engine block, and the eccentric ones, which are connected to the connecting rod of each cylinder. It is usually made of forged or cast steel.

2.1.7 Flywheel

The flywheel, also illustrated in Figure 2.6, is a mass of cast iron connected to the crankshaft to accumulate kinetic energy, transmitting a uniform angular speed to the motor shaft. The absorption of kinetic energy occurs at the moment of combustion in each cylinder and the release occurs by inertia at the other strokes. It reduces engine vibrations, caused by rapid in-cylinder pressure oscillations.

2.1.8 Valvetrain

The valvetrain, Figure 2.7, is a mechanical system that controls the operation of the engine valves. The valves are devices that allow or block the entry and exit of gases in the engine cylinder. There are two types of valves in an internal combustion engine: the intake valves and the exhaust valves.

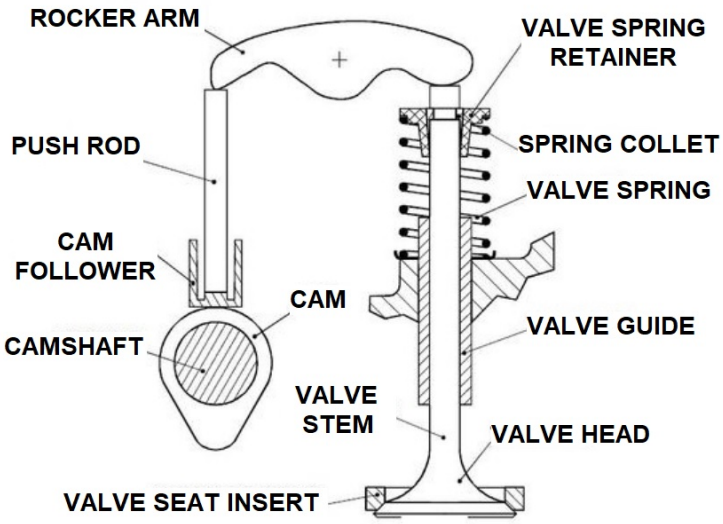

Figure 2.7: Valvetrain scheme (SRIVASTAVA, 2020).

The intake valves control the flow of air/fuel mixture into the combustion chamber, while the exhaust valves control the flow of exhaust gasses out of the combustion chamber once combustion is completed. The valves can be controlled in many different ways. The most common one is the camshaft mechanics, where a shaft of cams is designed to allow the opening and closure of valves in specific crank angles for better engine performance.

2.2 ICE Common Cycles

Internal combustion engines are commonly divided into two groups: two-stroke engines and four-stroke engines. This division is made by the cycle's type when producing work. The two-stroke engine completes a power cycle with two strokes (up and down movements of the piston) during only one crankshaft revolution. The four-stroke engine consists of four main phases during two crankshaft revolutions: intake, compression, power, and exhaust. There are many different types of four-stroke engine cycles. In the following subsections, the most relevant ones for studying Spark-Assisted Compression Ignition Engines are described.

2.2.1 Four-Stroke Spark Ignition Engine (SI)

The Four-Stroke Spark Ignition Engine works with the following sequence of operations, as shown in Figure 2.8.

1. Intake Stroke:

   At the intake stroke, air enters the engine through the intake manifold where it is mixed with the fuel, typically gasoline, by a fuel injector or carburetor (fuel can also be injected directly into the cylinder with the new direct-injection technology), resulting in a homogeneous mixture. That mixture enters the cylinder by the intake valves. During this stroke, intake valves are opened and exhaust valves, closed.

2. Compression Stroke:

   The up movement of the piston compresses the air-fuel mixture. The cylinder's pressure and temperature rise. Both intake and exhaust valves are closed.

3. Power Stroke:

   At the end of the compression stroke, a spark ignites the air-fuel mixture. A turbulent flame develops and propagates through the cylinder until it is extinguished at the cylinder walls. The gas expands with the downward movement of the piston. At this stage, the cylinder's temperature and pressure rise significantly.

4. Exhaust Stroke:

   The burned gases exit the engine past the exhaust valves through the exhaust manifold. The exhaust manifold channels the exhaust from individ-

ual cylinders into a central exhaust pipe (FERGUSON; KIRKPATRICK, 2016).

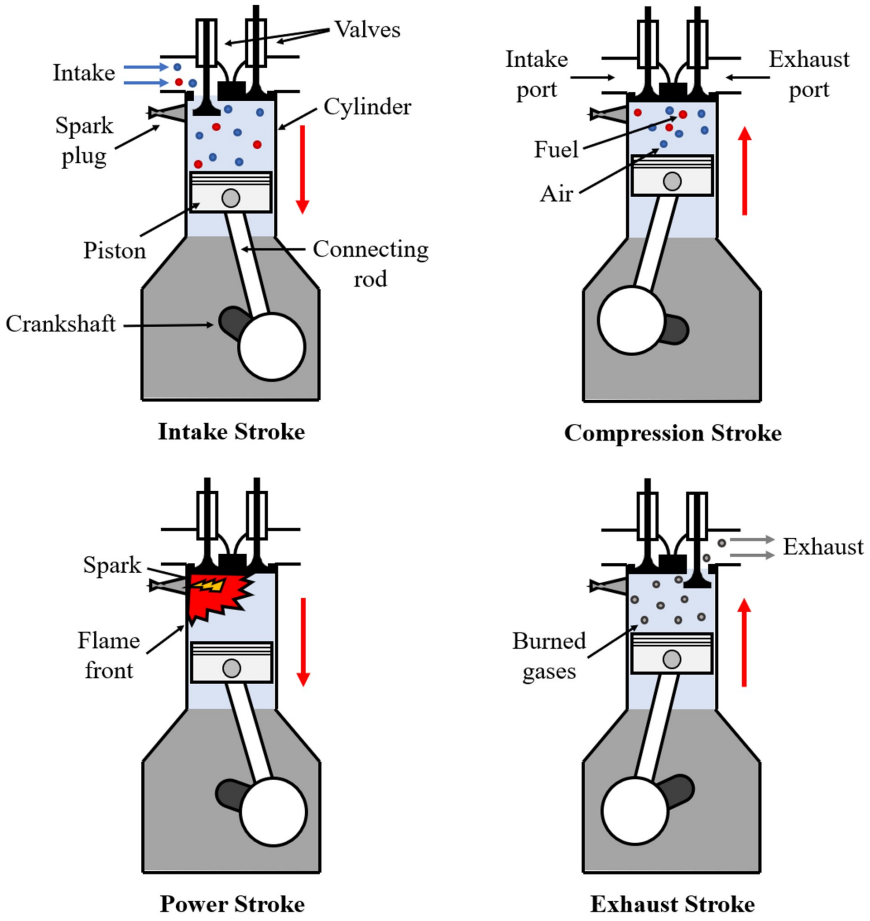

Figure 2.8: Four-stroke spark ignition cycle. Source: Authors own elaboration.

This cycle was first conceived by the German engineer Nikolaus Otto who, in 1876, built the first four-stroke spark ignition engine. The Otto cycle, named after him, studies the thermodynamic processes in function of pressure, temperature, volume, and the addition and removal of heat that a mass of air is subjected to. It represents the functioning of spark ignition engines and illustrates the main ideas of this type of engine.

The *idealized* Otto cycle, shown in Figure 2.9, is determined by its main five points, in which six processes are defined.

Process $0 \rightarrow 1$ represents the intake stroke. The air mass is aspirated in an isobaric process while the piston moves from the TDC to the BDC. The compression stroke is expressed by Process $1 \rightarrow 2$, where the piston compresses the air-fuel until the TDC. The air, representative of the mixture, undergoes an isentropic process. At $2 \rightarrow 3$, there is the isochoric addition of heat at the TDC, symbolizing the combustion at the combustion chamber. Process $3 \rightarrow$

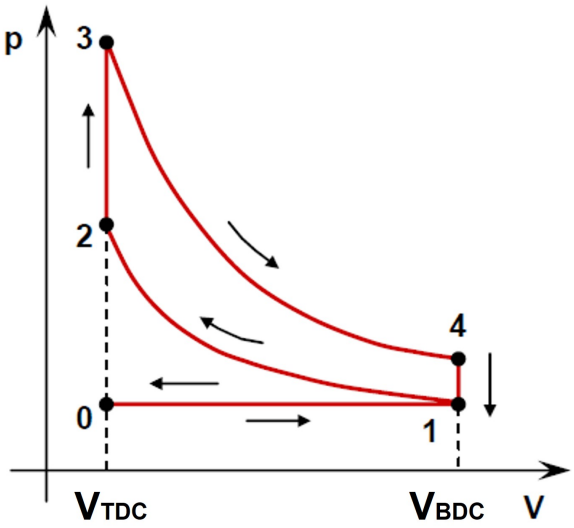

Figure 2.9: *Idealized* Otto cycle (FURLANI, 2006).

4 is the isentropic expansion of gases until BDC. Later, there is an isochoric heat rejection process at $4 \rightarrow 1$. Finally, there is an isobaric exhaust while the piston rises from BDC to TDC at $1 \rightarrow 0$.

It is noteworthy that the fuel used in a spark ignition engine must be sufficiently volatile to facilitate its vaporization, increase engine acceleration and reach a shorter time for the ideal operating temperature, without allowing the formation of steam bubbles in the supply circuit. In addition, a high-temperature auto-ignition fuel is also expected to prevent knock and thus considerably decrease its efficiency, as will be explained later. Thus, gasoline, ethanol and natural gas are usually used as fuel for a spark ignition engine close to stoichiometry (OBERT, 1971).

As advantages, these engines have lower cost; generate high rpm at low torque; pollute less; are light in weight, and require less space. On the other hand, SI engines have low efficiency, are not economical at high load, and have higher fuel consumption (HEYWOOD, 1988).

2.2.2 Four-Stroke Compression Ignition Engine (CI)

In 1882, Rudolph Diesel designed a new type of engine. In its process sequence, the Diesel cycle is similar to the Otto cycle, except for the admission of pure air at the intake stroke and the fuel's injection at the end of the compression stroke, Figure 2.10. This change enables a high engine compression ratio, increasing the cycle's efficiency (OBERT, 1971).

The compression of the air raises the cylinder pressure and temperature and provokes the auto-ignition (compression ignition) of the air-fuel mixture

when the fuel is injected into the combustion chamber.

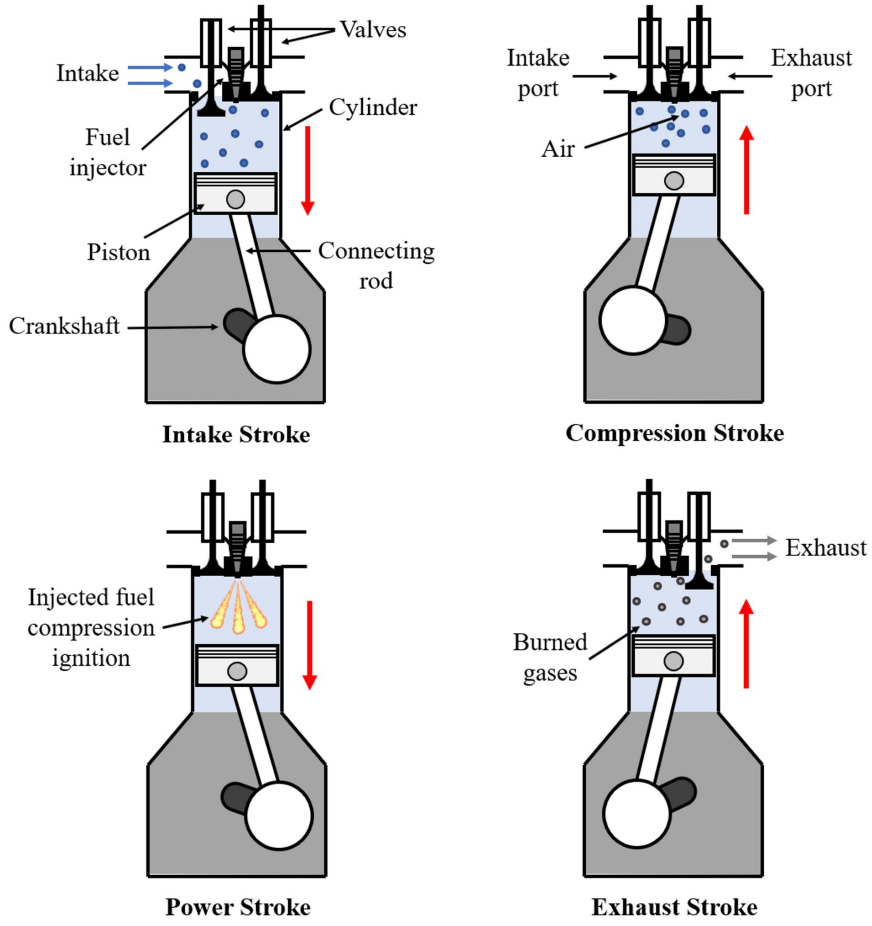

Figure 2.10: Four-stroke compression ignition cycle. Source: Authors own elaboration.

The diesel engine works according to the following cycle of operations:

1. Intake Stroke:

   At the intake stroke, pure air is admitted into the cylinder by the intake valves.

2. Compression Stroke:

   The air pressure and temperature are raised above the auto-ignition temperature of the fuel (high compression ratio). Diesel is, then, injected at the end of the compression stroke.

3. Power Stroke:

   The fuel vaporizes, mixes and self-ignites simultaneously. It is noteworthy that exists a time for which a homogeneous mixture must be maintained at temperature, T, and pressure, p, before it auto-ignites, it is called auto-ignition delay.

4. Exhaust Stroke:

   The burned gases are pushed out of the cylinder past the exhaust valves (FERGUSON; KIRKPATRICK, 2016).

The *idealized* Diesel cycle assumes the air as an ideal gas and ignores combustion chemistry, exhaust, recharge procedures, and mechanical losses. It is composed of five points and six processes. as shown in Figure 2.11.

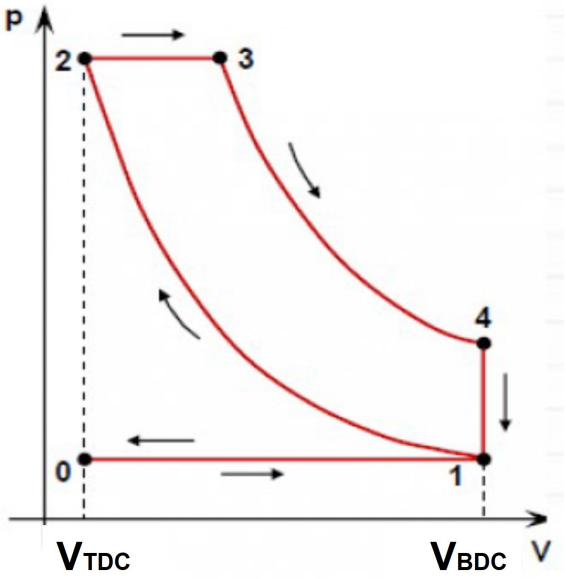

Figure 2.11: *Idealized* Diesel cycle (FURLANI, 2006).

As seen in the *idealized* Otto cycle, process 0→1 represents the intake stroke. The air is aspirated in an isobaric process while the piston moves from the TDC to the BDC. The compression stroke is expressed by Process 1→2, where the piston compresses the air adiabatically and reversibly until the TDC. One can note that the air pressure at the end of the compression stroke in a Diesel engine is much greater than the one in the Otto engine. At 2→3, the isobaric addition of heat designates the combustion process. It outlines the ignition of the fuel as it is injected into the combustion chamber. Process 3→4 is the isentropic expansion of gases until BDC. Processes 4→1 and 1→0 are similar to the SI engine.

These engines are more efficient than SI engines; have higher load carrying capability, and generate high power. Nevertheless, CI engines are higher in weight; produce more vibration; release more air pollutants, and present higher cost (HEYWOOD, 1988).

2.2.3 Homogeneous Charge Compression Ignition Engine (HCCI)

Homogeneous Charge Compression Ignition engines are internal combustion engines whose well-mixed air-fuel mixture is compressed to the point of auto-ignition. Like other combustion engines, the chemical reaction releases energy, producing work and heat.

The HCCI combustion is one of the first low-temperature combustion techniques developed (FERGUSON; KIRKPATRICK, 2016). It is a relatively new technology if compared to the other two discussed previously. This engine operates with very lean mixtures (fuel-air equivalence ratio of 0.4-0.7) and a high-octane fuel (such as gasoline and natural gas). For that reason, it has a lower peak temperature than those found in SI and CI engines (typically around 1500 K). Due to this low-temperature cycle, there is less NO_X formation, leading to limited environmental pollution (DEC, 2009).

The four-stroke cycle of an HCCI engine works as follows:

1. Intake Stroke:

   As in SI engines, the intake valves admit the air-fuel mixture, which is very lean, as indicated beforehand.

2. Compression Stroke:

   At the compression stroke, the cylinder's pressure and temperature increase. The cylinder and piston's geometry is designed to produce a homogeneous mixture at the time of ignition.

3. Power Stroke:

   The mixture reacts spontaneously, without the need for a spark or the injection of fuel. The multi-point auto-ignition augments combustion speed, illustrated at Figure 2.12. The cylinder peak temperature is low, controlling the formation of NOx.

4. Exhaust Stroke:

   The exhaust stroke works as the other engines studied previously. The piston expels the burned gases from the cylinder to the exhaust port. Inlet valves are closed and discharge valves are opened (HAIRUDDIN; WANDEL; YUSAF, 2014).

In a spark-ignition engine, the phenomenon of knock can occur. This event happens when the mixture reaches the thermodynamic state to ignite spontaneously, not resulting from the propagation of the flame front ignited by

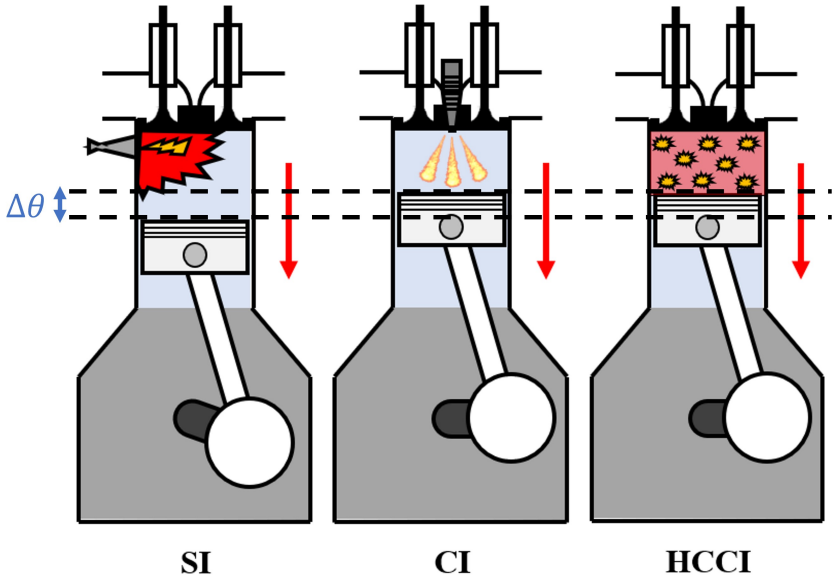

Figure 2.12: Comparison of SI, CI and HCCI combustion mechanisms. Source: Authors own elaboration.

the spark plug. It is harmful to the engine's efficiency and mechanical structure for two reasons: it can occur before the TDC, which works against the ascent of the cylinder in the compression stroke; or at a pocket of fuel-air outside the flame front in the power stroke, which results in high pressure inside the cylinder, damaging its components (NATES; YATES, 1994).

An HCCI engine, however, applies auto-ignition as a technique to reduce pollutants and augment efficiency. In this type of engine, the homogeneous compressed charge ignites spontaneously and simultaneously at different regions, eliminating any shock wave or pin strike.

Furthermore, for optimal operation of the HCCI engine, the combustion timing must be precise. If simultaneous compression ignition takes place before the desired moment, knock occurs. On the other hand, if the mixture does not enter the thermodynamic state for auto-ignition, there is a misfire, which does not produce work and ruins the engine's efficiency, as it is illustrated in Figure 2.13.

The HCCI fuel must behave in a way that the reaction takes place at the TDC. So, the fuel must be injected, evaporate, enter in an auto-ignition temperature and pass the ignition delay right before the TDC. Thus, HCCI engines commonly use high octane fuels (low reactivity) or others like Fischer-Tropsch (FT) Naphtha, which have self-ignition characteristics compatible with standard compression ratios (RYAN; MATHEAUS, 2003).

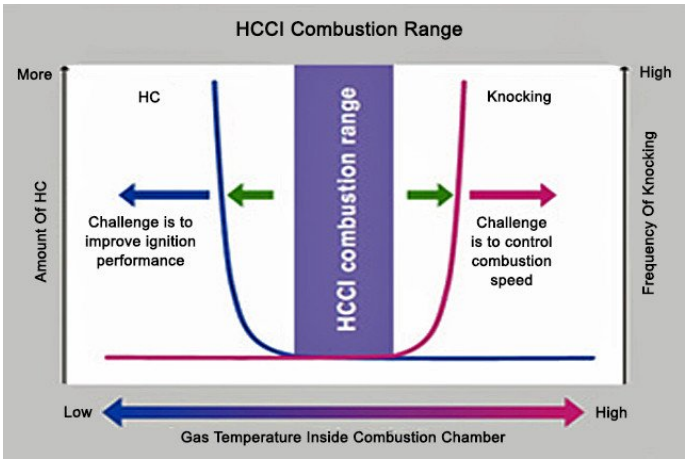

Figure 2.13: Combustion range in HCCI engines (MATSUDA et al., 2008).

2.3 Spark-Assisted Compression Ignition Engine (SACI)

The Spark-Assisted Compression Ignition engine is a new internal combustion engine technology that acts similarly to HCCI, but with the help of the spark plug to control the combustion timing (ZHAO, 2007). It is also known as Spark-Controlled Compression Ignition (SPCCI), Spark-Induced Compression Ignition (SICI), Spark Assisted Homogeneous Charge Compression Ignition (SA-HCCI), and Spark Ignition - Homogeneous Charge Compression Ignition (SI-HCCI).

This technology is based on a two combustion step, shown in Figure 2.14. During the compression phase, the air-fuel mixture temperature and pressure increase until the verge of self-ignition. At this moment, a spark ignites a part of the mixture. There is the creation of a flame front near the spark plug, similar to an SI engine. The cylinder pressure rises, allowing the unburned gases to reach elevated pressure and temperature to auto-ignite. The second step starts at the compression ignition, speeding up combustion and improving performance (MAZDA, 2018).

As seen earlier, the HCCI engine works in a narrow range of optimal performance: between two opposites that considerably weaken the engine's efficiency (knock and misfire). The SACI alternative allows better control of the combustion time and, as a result, more regular administration of the energy response (PERSSON et al., 2008).

The greater the compression ratio of an engine, the higher is its thermal efficiency. However, SI engines cannot reach elevated compression ratios due to their high octane fuels, which attain the compression ignition point and lead to knock. However, the proposed technology seeks auto-ignition. So, it succeeds in uniting the octane fuel with a high compression ratio, managing

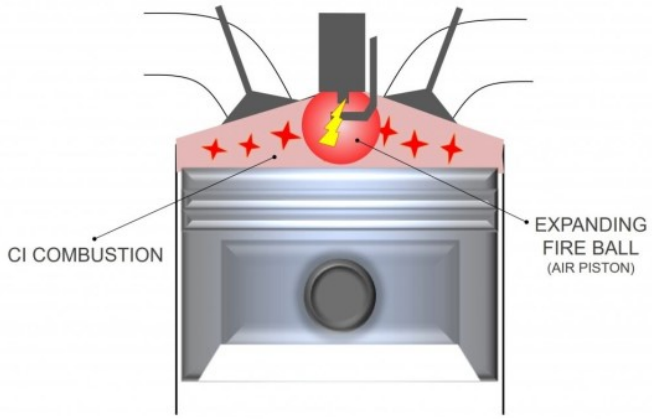

Figure 2.14: Schematic representation of the combustion process in a SACI engine (MAZDA, 2019).

the auto-ignition timing with the spark.

Furthermore, the SPCCI combustion achieves to increase the work produced by the chemical reaction. While ignition in an Otto cycle happens from a spark, creating a flame front that must go throughout the entire mixture for the fuel to burn completely and produce work, the SACI cycle, like the Diesel, provides simultaneous combustion inside the cylinder. Therefore, during the entire descent of the piston, it applies most of the energy generated into the production of work, as one can observe in Figure 2.15.

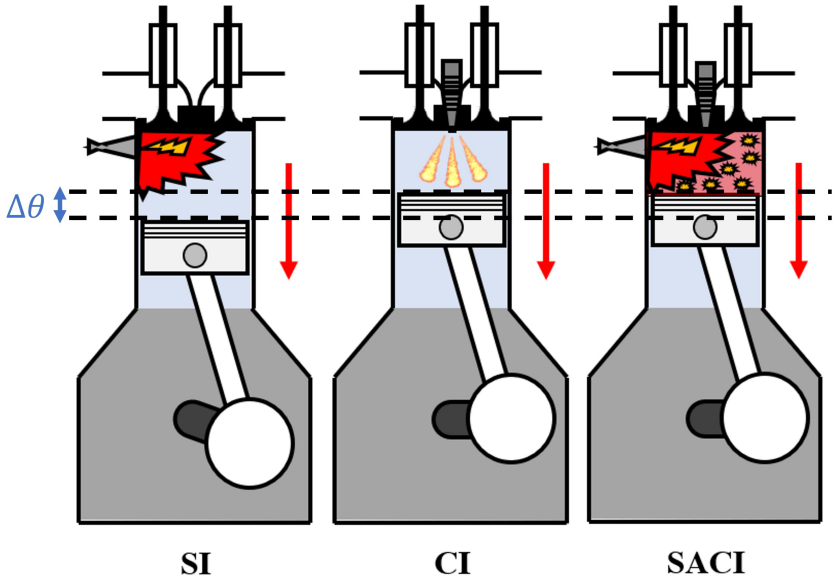

Figure 2.15: Comparison of SI, CI and SACI combustion mechanisms. Source: Authors own elaboration.

An ideal engine works so that there is less thermal energy loss and fewer pollutants emissions. Therefore, SACI technology opts for a very lean mixture (fuel-air equivalence ratio of 0.3-0.5), which reduces the engine's temperature,

heat loss, and NOx emissions. Thus, a turbocharger is placed before the inlet manifold, making possible the disposition of amounts of air into the cylinder.

As done for the previous cycles, one can analyze the four-stroke SACI engine:

1. Intake Stroke:

   As in SI and HCCI engines, the air-fuel mixture enters the cylinder by the intake valves. This mixture is very lean with the help of the turbocharger, which drives the air into the cylinder.

2. Compression Stroke:

   The mixture is compressed, raising its temperature and pressure, as in SI, CI, and HCCI engines. SACI engines, however, have a fuel injector near the spark plug that permits stratification of the fuel. Fuel is injected during the compression stroke, making the mixture richer around the spark plug. It allows the development of the flame front at the section before the autoignition of the unburned gases.

3. Power Stroke:

   The electric discharge ignites the mixture close to the spark plug. This combustion increases the pressure throughout the cylinder so that the unburned gases self-ignites simultaneously. The schematic drawing in Figure 2.16 illustrates SACI combustion inside the cylinder by separating the spark ignition (SI) flame front from the spontaneous ignition (or compression ignition, CI).

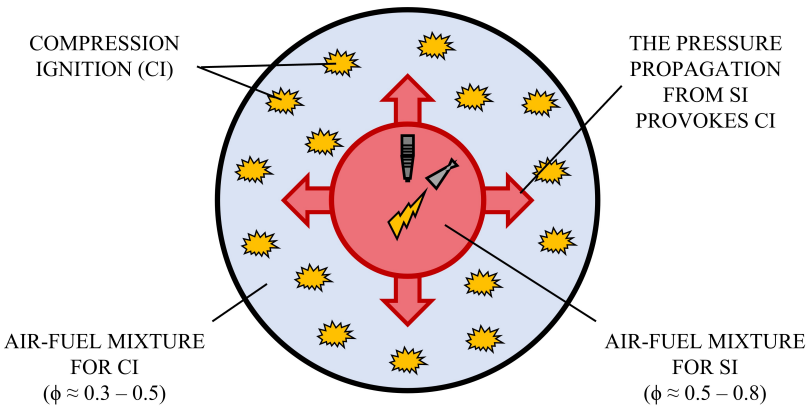

Figure 2.16: SACI combustion scheme. Source: Authors own elaboration.

4. Exhaust Stroke:

   As in other engines, the piston expels the burned gases. While inlet valves are closed, discharge valves are opened.

In a SACI engine, one can define a transition point between the phase in which the SACI engine works as an SI and when it starts to behave as an HCCI. This point is called SOHCCI (Start Of HCCI), as illustrated in Figure 2.17. The graph shows the mass fraction burned as a function of the crankshaft angle. One can notice the variation of the Wiebe curve after the autoignition point, exhibiting faster combustion, like an HCCI.

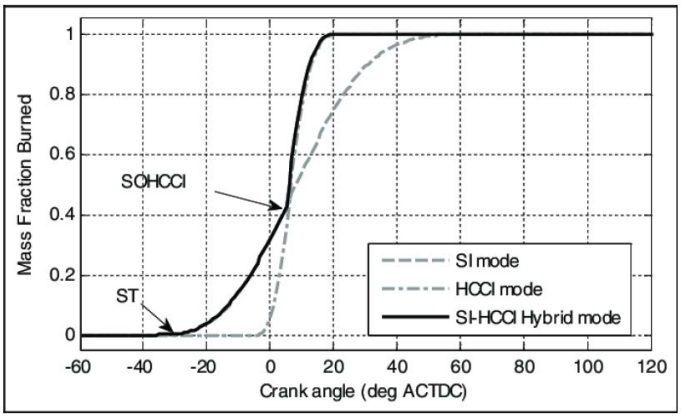

Figure 2.17: Comparison of the mass fraction burned as a function of the crank angle for SI, HCCI and SACI combustion modes (YANG; ZHU, 2012).

2.3.1 State-of-the-art research in SACI engines

SACI engines were first studied in 2005 by Wang et al. (WANG et al., 2005). The goal was to analyze the effects of spark-ignition and stratified charge in HCCI gasoline engines. Their idea was a success: the adapted HCCI engine working in SACI combustion mode stabilized HCCI engine operation, augmented the average IMEP about 39%, and reduced NOx, HC, and CO emissions in 74%, 82% and 32% respectively, Figure 2.18. However, at the time the authors were thinking about SACI combustion merely as a strategy to better stabilize HCCI to SI transition in a specific HCCI engine operation.

After the discovery of this new association of modes of combustion, researchers started studying the effects of this multi-mode combustion method on several engine performance parameters, and some authors say that this type of combustion is the future of ICEs (WHITELEY, 2017).

Taking the software *Dimensions*, from Digital Science, we can analyze the SACI publications throughout the years (since there are not that many), we can generate Figure 2.19 (DIGITALSCIENCE, 2021). We see that the number of publications on this topic in scientific reviews has been growing ever since.

Bunting, in 2006, analyzed SACI combustion with different spark timings and fuels. He noticed that the early exhaust valve closing ("negative overlap")

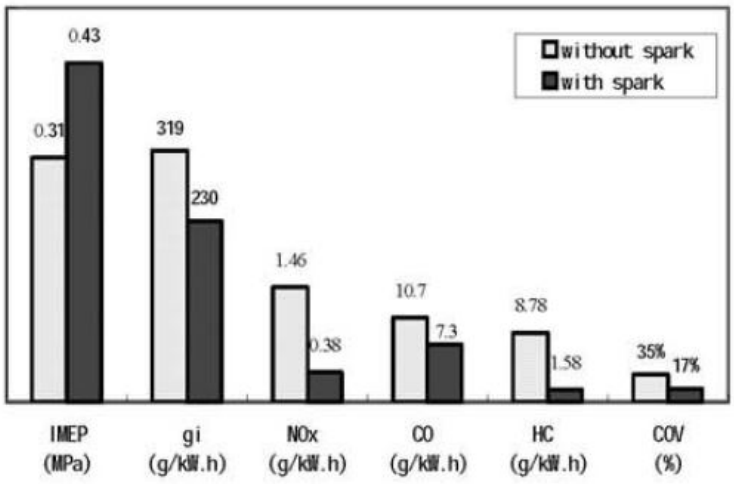

Figure 2.18: Effects of SI in HCCI engines (WANG et al., 2005).

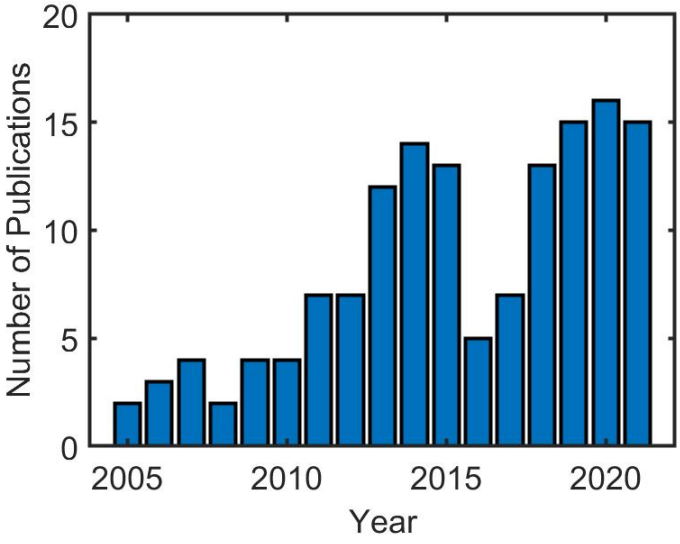

Figure 2.19: The history of publications on SACI engines. Source: Authors own elaboration.

strategy helps to better define the mixture's auto-ignition time. Furthermore, fuels with higher octane numbers were found to ignite more easily and to burn more quickly than fuels with lower octane sensitivity (BUNTING, 2006).

The effects of swirl and fuel stratification were studied later by Persson, Johansson and Remón. In these studies, they showed that in-cylinder turbulence affects the mixture's auto-ignition timing and, therefore, SACI combustion as a whole. However, the authors clarified that more experiments were needed in order to fully understand this influence (PERSSON; JOHANSSON; REMóN, 2007). Afterwards, they were able to outline that the rise of mixture stratification increases combustion timing (PERSSON et al., 2008).

Then, Keros et al. started to study SACI emissions compared to other

combustion modes. They analyzed SI, HCCI, and SACI technologies for a limited range of conditions. In these experiments, HC emissions were weakly sensitive to the engine operating mode. Moreover, NOx emissions were a strong function of spark timing for SACI engines, as it can be seen in Figure 2.20. It is important to notice that low NOx emissions (under 100 ppm) could be found at both HCCI and SACI combustion modes (KEROS et al., 2009).

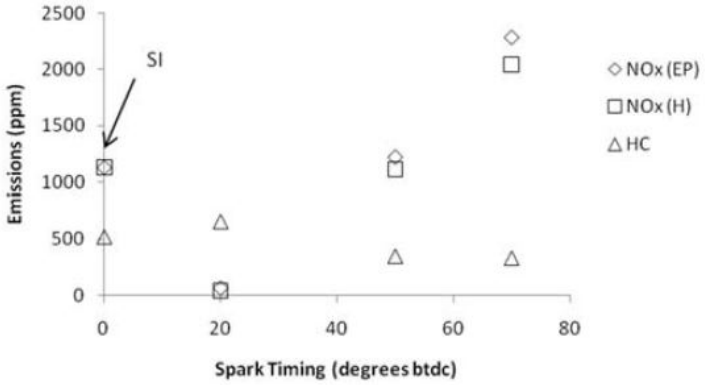

Figure 2.20: Spark timing influence on SACI emissions (KEROS et al., 2009).

In 2010, Wang et al. analyzed SACI combustion visually. They modified a gasoline engine to enter in HCCI combustion after a first SI flame development, and took multiple pictures of the flame (WANG et al., 2010). Figure 2.21 illustrates the difference between the SI and the SACI combustion. In SI, the authors observed the flame propagation after the spark ignition. It develops until all the mixture is burned inside the cylinder. In SACI, however, before the full propagation of the flame, the unburned volume reaches the condition of auto-ignition and then self-ignites almost simultaneously.

In the last decade, SACI combustion has been widely investigated. These studies present promising experimental and numeric results for this new type of combustion compared to traditional techniques.

Ortiz-Soto's studies in Figure 2.22 show that, while the net thermal efficiency of SI engines varies from 24 to 32% and CI engines from 37 to 43%, at their optimal range, SACI engines have an efficiency of 41 to 43%, more constant than HCCI as a function of the MEP (ORTIZ-SOTO et al., 2019).

Furthermore, Chang displays the difference in emissions between SI, HCCI, and SACI combustion as a function of intake air temperature. While SI engines emit around 9.5 g/kWh of NOx, HCCI and SACI engines have, on average, an emission of 3.5 g/kWh, i.e., 63% lower (CHANG et al., 2017), as shown in Figure 2.23.

This technique has also been the center of multiple sensitivity analysis. Many parameters have been studied, such as the influence of ambient temper-

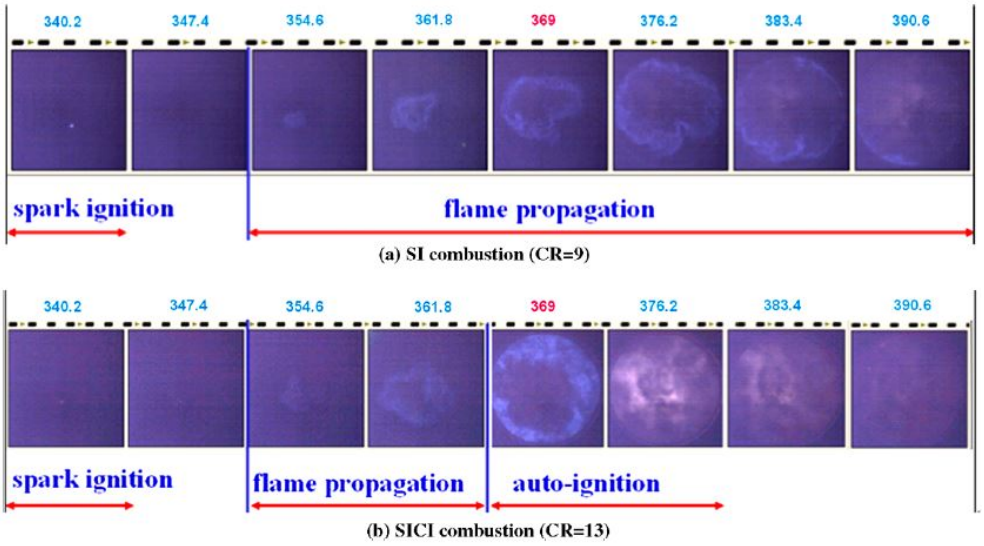

Figure 2.21: Visual comparison between SI and SACI combustion (WANG et al., 2010).

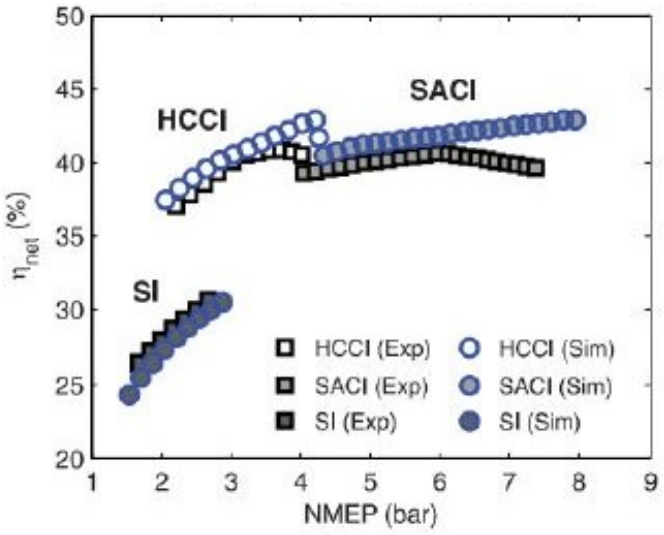

Figure 2.22: Comparison of the net thermal efficiency versus engine load for SI, HCCI and SACI engines (ORTIZ-SOTO et al., 2019).

ature and humidity in the SACI combustion, affirming that higher ambient temperature formates higher NOx (CHANG et al., 2017); the addition of substances into the fuel to stabilize autoignition such as heptane (CHEN et al., 2020); spark timing for better efficiency (MIDDLETON et al., 2015); EGR injection strategy in autoignition control (ZHOU et al., 2018); and the numerical study of the flame front in H_2 SACI engines (ZHANG et al., 2017).

Despite the multiple studies in this new type of multi-mode combustion, there is still a lot to learn from this technique. This technology does not even reach 1% of the studies done on ICEs per year, which sounds weird when we compare it to the idea of being the savior of ICEs (DIGITALSCIENCE,

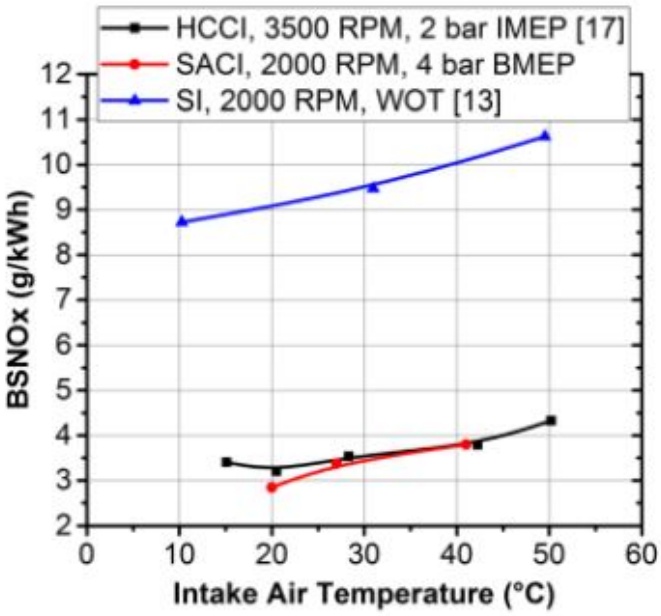

Figure 2.23: Engine types brake specific NOX emissions comparison (CHANG et al., 2017).

2021). As it starts to be noticed, researchers from all over the world in the internal combustion and heat engines area become interested in the SACI studies results. The industry, not wanting to be left behind, launches itself in research and development to integrate this system into its knowledge portfolio.

2.3.2 SkyActiv-X

The SACI technology was introduced to the industry in 2013 by Mazda Motor Corporation, who has been developing it ever since (MAZDA, 2019). In 2019, the company released the engine prototype and in July of the same year, they started selling the Mazda 3 car in Europe, which already had the SkyActiv-X engine with SACI/SPCCI technology, Figure 2.24.

(a) Mazda 3. (b) SkyActiv-X engine.

Figure 2.24: Mazda's SACI/SPCCI new engine (MAZDA, 2018).

Tables 2.1 and 2.2 show the data issued by Mazda for the SkyActiv-X 2.0 engine in the European version (2019) and its update (2021).

Table 2.1: Mazda SkyActiv-X - Engine Details (MAZDA, 2019)

Parameter	**Unit**	**Value**
Displacement	cm^3	1,998
Compression Ratio	-	16.3
Max. Power	kW (rpm)	132 (6,000)
Max. Torque	N.m (rpm)	224 (3,000)
Recommended fuel type	-	95 RON
CO_2 Emissions	g/km	11
Fuel-Air Equivalence Ratio	-	0.4

Table 2.2: Mazda e-SkyActiv X - Engine Details (MAZDA, 2021)

Parameter	**Unit**	**Value**
Displacement	cm^3	1,998
Compression Ratio	-	15.0
Max. Power	kW (rpm)	137 (6,000)
Max. Torque	N.m (rpm)	240 (4,000)
Recommended fuel type	-	95 RON
CO_2 Emissions	g/km	5
Fuel-Air Equivalence Ratio	-	0.4

3
Numerical Modeling

The thermodynamics of an internal combustion engine is governed by the engine's geometry, the conservation laws of mass and energy, and the combustion reaction. In this chapter, the engine's main geometric parameters will be introduced, followed by the thermodynamic hypotheses adopted. Then, the derivation of the conservation equations will be presented with the selected models for their calculation, such as the chemical equilibrium of the combustion reaction, the intake and exhaust flow, the blowby, the heat transfer, the combustion progress, and the auto-ignition. Finally, the emission calculation and the numerical method employed will be explained.

3.1
Engine Geometry

The geometry of an internal combustion engine is fundamental for understanding its thermodynamics. The following parameters, shown in Figure 3.1, are of particular interest: cylinder bore, B (m); connecting rod length, L (m); crank radius, R (m); cylinder stroke, S (m); and crank angle, θ (°). One can notice that the crank radius is one-half of the stroke and that when the piston is at the TDC, the crank angle is 0º.

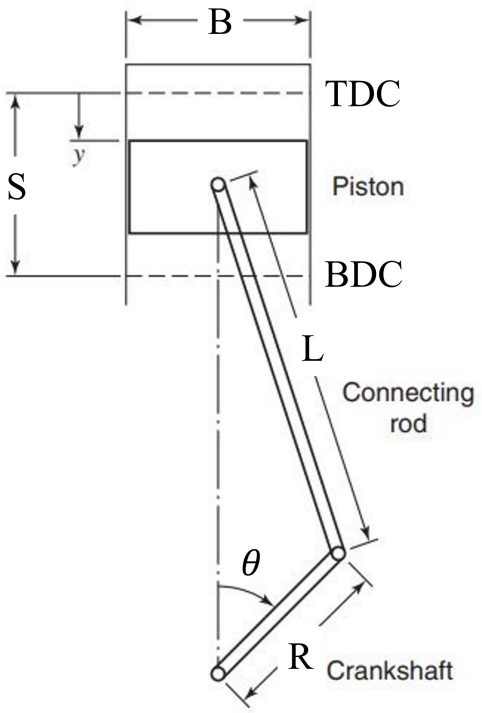

Figure 3.1: Engine's geometry schema (FERGUSON; KIRKPATRICK, 2016).

The first geometric relation of an engine to be presented in this chapter is the compression ratio, r_c, which is the ratio of the maximum and minimum cylinder volume.

$$r_c = \frac{V_{BDC}}{V_{TDC}} \ [-] \tag{3-1}$$

Another vital parameter is the displacement volume, V_d, the difference between the maximum and minimum volume for a single cylinder.

$$V_d = V_{BDC} - V_{TDC} = \frac{\pi B^2}{4} S \ [m^3] \tag{3-2}$$

It is noteworthy that the total displacement volume, V_d^{tot}, is calculated as the displacement volume for single-cylinder times the number of cylinders in an engine.

After defining the compression ratio, one can calculate the Top Dead Center Volume, V_{TDC}, as a function of the bore, the stroke, and the compression ratio.

$$V_{TDC} = \frac{\pi B^2}{4} \cdot \frac{S}{(r_c - 1)} \ [m^3] \tag{3-3}$$

The cylinder volume, V, can be written as a function of the crank angle and the geometric parameters cited above.

$$V(\theta) = V_{TDC} \cdot \left[1 + \frac{(r_c - 1)}{2} \cdot \left[1 - cos(\theta) + \frac{1}{\epsilon} \cdot \left[1 - \sqrt{(1 - \epsilon^2 sin^2(\theta)} \right] \right] \right] \ [m^3] \tag{3-4}$$

Where ϵ is the ratio between the half-stroke and the connecting rod length:

$$\epsilon = \frac{S}{2 \cdot L} = \frac{R}{L} \ [-] \tag{3-5}$$

Figure 3.2 illustrates the variation of the cylinder volume as a function of the crank angle for the Engine Specification A, in Appendix A. As one can see, the compression ratio is the higher value in the graph by definition. Furthermore, the cylinder's lateral area can be calculated with the cylinder volume and the cylinder bore.

$$A(\theta) = V(\theta) \cdot \frac{4}{B} \ [m^2] \tag{3-6}$$

As we have seen so far, to well-define the engine geometry, one needs five parameters: the cylinder bore (B), the compression ratio (r_c), the total displacement volume (V_d^{tot}), the number of cylinders (N_{cyl}) and the half-stroke to rod ratio (ϵ). These five parameters specify the engine geometry.

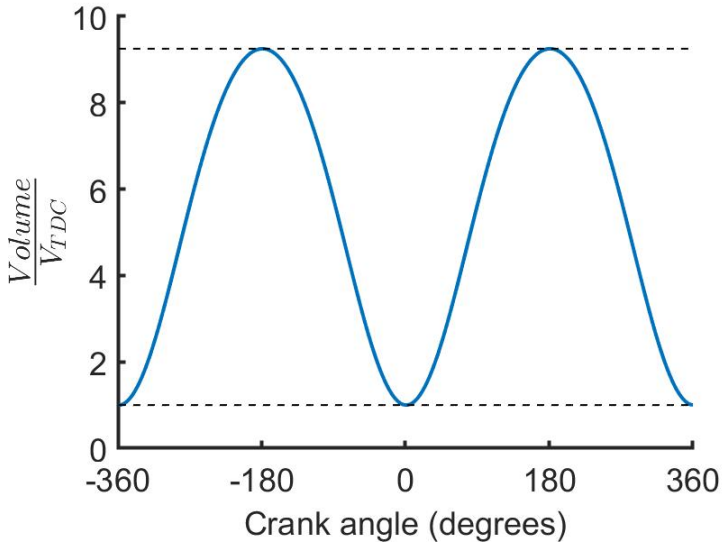

Figure 3.2: Cylinder volume in Engine Specification A (Appendix A).

However, some geometric relations can be changed by another without losing any information: i.e., one can choose to use the cylinder stroke instead of the total displacement volume. Thus, to have a complete view of the engine studied in this project, a description based on six parameters was adopted, as shown in Table 3.1, even though there is redundant information.

Table 3.1: Engine main geometric parameters

Parameter	Symbol	Unit
Bore	B	mm
Stroke	S	mm
Compression Ratio	r_c	-
Total Displacement Volume	V_d^{tot}	cm^3
Number of Cylinders	N_{cyl}	-
Half-Stroke to Rod Ratio	ϵ	-

3.2 Thermodynamics

To compute the parameters involved in an internal combustion engine's thermodynamic cycle, it is necessary to consider the state changes at every stage, such as intake, compression, power, and exhaust. To simplify the analysis, the fuel-air mixture and the products of combustion are modeled as ideal gases. An ideal gas has a simplified relation between pressure, temperature, and volume.

$$PV = mrT \tag{3-7}$$

Where P is the pressure in kPa, V is volume in m^3, m is the mass of gas in kg, r is the mass-specific gas constant in $kJ/(kg.K)$, and T is the temperature in K. The mass-specific gas constant can be calculated as

$$r = \frac{R_{univ}}{M} \left[\frac{kJ}{kg.K}\right] \tag{3-8}$$

where R_{univ} is the universal gas constant ($R_{univ} = 8.314kJ/(kmol.K)$) and M is the molar mass of the mixture in $kg/kmol$.

The mass fraction, x_i, of any given species is defined as

$$x_i = \frac{m_i}{m} \ [-] \tag{3-9}$$

resulting in

$$\sum_{i=1}^{n} x_i = 1 \tag{3-10}$$

And the molar fraction, y_i, of a given species, is

$$y_i = \frac{n_i}{n} \ [-] \tag{3-11}$$

also resulting in

$$\sum_{i=1}^{n} y_i = 1 \tag{3-12}$$

To better define the chemical species and properties of the mixture, a two-zone combustion model is used. This representation divides the gas mixture into two control volumes: burned and unburned.

In this approach, each part has its own: mass, volume, temperature, chemical species, internal energy, entropy, and enthalpy. However, the in-cylinder pressure is assumed to be the same at both zones.

Therefore, it is possible to formulate:

$$V = V_u + V_b \ [m^3] \tag{3-13}$$

$$v = \frac{V}{m} = x_b v_b + x_u v_u \left[\frac{m^3}{kg}\right] \tag{3-14}$$

where v is the specific volume in m^3/kg, and x_b and x_u are the mass fraction of burned and unburned gases, respectively. It is noteworthy that $x_b + x_u = 1$.

Assuming the two zones to be ideal gases,

$$Pv_u = r_u T_u \tag{3-15}$$

$$Pv_b = r_b T_b \tag{3-16}$$

where,

$$r_i = \frac{R_{univ}}{MW_i} \tag{3-17}$$

and MW_i is the molecular weight of species i in $kg/kmol$.

Finally, the properties of each zone (specific volume v, specific internal energy u, and specific enthalpy h) are a function of the in-cylinder pressure and its zone temperature.

$$v_u = v_u(P, T_u);\;\; u_u = u_u(P, T_u);\;\; h_u = h_u(P, T_u) \tag{3-18}$$

$$v_b = v_b(P, T_b);\;\; u_b = u_b(P, T_b);\;\; h_b = h_b(P, T_b) \tag{3-19}$$

These relations will be helpful to simplify the conservation equations and, consequently, calculate the in-cylinder pressure and temperatures at every numerical step.

3.2.1 Thermodynamic Properties

The calculation of the engine's pressure and temperatures from the conservation laws depends on some thermodynamic properties of the gas mixture and its chemical species. These properties (c_p, h, and s) are a function of temperature and were determined by numerous institutions of research. In the present work, we calculate the thermodynamic properties with the data of two researches: NASA (MCBRIDE; GORDON; RENO, 1993), and Perry (MALONEY, 2008). We also compare the properties values with the model utilized by Ferguson (FERGUSON; KIRKPATRICK, 2016).

NASA model was used for almost all the species. It had consistent predictions of the heat capacity, enthalpy, and entropy at the temperature range needed. It also considers the intermediate species, such as H, O, and OH radicals, differently from Perry's model who has only species at chemical equilibrium as we can see in Table 3.2.

$$c_p(T) = r\Big(a_1 T^{-2} + a_2 T^{-1} + a_3 + a_4 T + a_5 T^2 + a_6 T^3 + a_7 T^4\Big)\;\; [-] \tag{3-20}$$

$$h(T) = r\Big[-a_1 T^{-1} + a_2 ln(T) + a_3 T + a_4 \frac{T^2}{2} + a_5 \frac{T^3}{3} + a_6 \frac{T^4}{4} + a_7 \frac{T^4}{5} + b_1\Big]\;\; [-] \tag{3-21}$$

$$s(T) = r\left[-a_1\frac{T^{-2}}{2} - a_2T^{-1} + a_3ln(T) + a_4T + a_5\frac{T^2}{2} + a_6\frac{T^3}{3} + a_7\frac{T^4}{4} + b_2 \right][-] \tag{3-22}$$

Perry's model is used to predict the fuel's thermodynamic properties. In it, the c_p is modeled and the enthalpy and entropy are calculated using the enthalpy and entropy of formation in the temperature of reference. Table 3.3 shows this model's constants for methane.

$$c_p(T) = C_1 + C_2\left[\frac{C_3/T}{sinh(C_3/T)}\right] + C_4\left[\frac{C_5/T}{cosh(C_5/T)}\right] \left[\frac{kJ}{kmol.K}\right] \tag{3-23}$$

$$h(T) - h(T_{ref}) = \int_{T_{ref}}^{T} c_p dT \left[\frac{kJ}{kmol}\right] \tag{3-24}$$

$$s(T) - s(T_{ref}) = \int_{T_{ref}}^{T} \frac{c_p}{T} dT \left[\frac{kJ}{kmol.K}\right] \tag{3-25}$$

Since Perry's model gives the specific heat capacity, enthalpy, and entropy on a molar basis, these properties will have to be divided by the fuel's molecular weight (in $kg/kmol$). That's where they will be in the format wanted in the conservation laws, i.e., $kJ/(kg.K)$, $kJ/(kg)$, and $kJ/(kg.K)$, respectively.

Figures 3.3, and 3.4 show the difference in the values of c_p and h in each model.

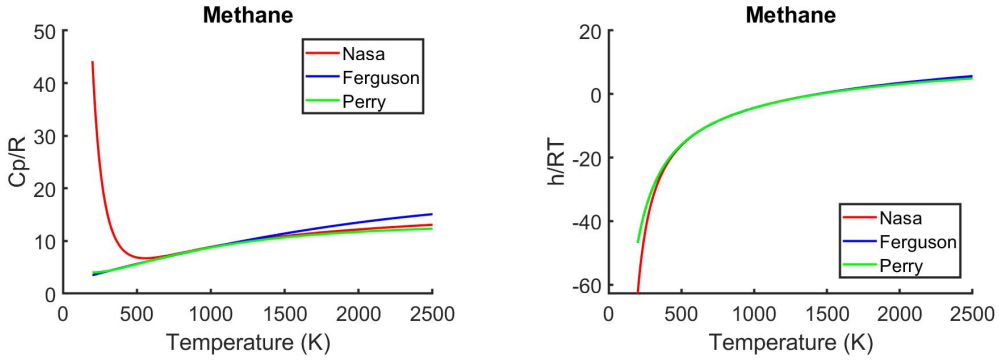

(a) Heat capacity model comparison for methane.

(b) Enthalpy model comparison for methane.

Figure 3.3: Fuel's heat capacity and enthalpy models.

Table 3.2: NASA model constants (MCBRIDE; GORDON; RENO, 1993)

Species	Range	a_1	a_2	a_3	a_4	a_5	a_6	a_7	b_1	b_2
CO_2	$T \leq 1000$	+4.94E+04	−6.26E+02	+5.30E+00	+2.50E−03	−2.12E−07	−7.68E−10	+2.84E−13	−4.52E+04	−7.04E+00
	$T > 1000$	+1.17E+05	−1.78E+03	+8.29E+00	−9.22E−05	+4.86E−09	−1.89E−12	+6.33E−16	−3.90E+04	−2.65E+01
H_2O	$T \leq 1000$	−3.94E+04	+5.75E+02	+9.31E−01	+7.22E−03	−7.34E−06	+4.95E−09	−1.33E−12	−3.30E+04	+1.72E+01
	$T > 1000$	+1.03E+06	−2.41E+03	+4.64E+00	+2.29E−03	−6.83E−07	+9.42E−11	−4.82E−15	−1.38E+04	−7.97E+00
N_2	$T \leq 1000$	+2.21E+04	−3.81E+02	+6.08E+00	−8.53E−03	+1.38E−05	−9.62E−09	+2.51E−12	+7.10E+02	−1.07E+01
	$T > 1000$	+5.87E+05	−2.23E+03	+6.06E+00	−6.13E−04	+1.49E−07	−1.92E−11	+1.06E−15	+1.28E+04	−1.58E+01
O_2	$T \leq 1000$	−3.42E+04	+4.84E+02	+1.11E+00	+4.29E−03	−6.83E−07	−2.02E−09	+1.03E−12	−3.39E+03	+1.84E+01
	$T > 1000$	−1.03E+06	+2.34E+03	+1.81E+00	+1.26E−03	−2.18E−07	+2.05E−11	−8.19E−16	−1.68E+04	+1.73E+01
CO	$T \leq 1000$	+1.48E+04	−2.92E+02	+5.72E+00	−8.17E−03	+1.45E−05	−1.08E−08	+3.02E−12	−1.30E+04	−7.85E+00
	$T > 1000$	+4.61E+05	−1.94E+03	+5.91E+00	−5.66E−04	+1.39E−07	−1.78E−11	+9.62E−16	−2.46E+03	−1.38E+01
H_2	$T \leq 1000$	+4.07E+04	−8.00E+02	+8.21E+00	−1.26E−02	+1.75E−05	−1.20E−08	+3.36E−12	+2.68E+03	−3.04E+01
	$T > 1000$	+5.60E+05	−8.37E+02	+2.97E+00	+1.25E−03	−3.74E−07	+5.93E−11	−3.60E−15	+5.33E+03	−2.20E+00
H	$T \leq 1000$	+0.00E+00	+0.00E+00	+2.50E+00	+0.00E+00	+0.00E+00	+0.00E+00	+0.00E+00	+2.54E+04	−4.46E−01
	$T > 1000$	+6.07E+01	−1.81E−01	+2.50E+00	−1.22E−07	+3.73E−11	−5.68E−15	+3.41E−19	+2.54E+04	−4.48E−01
O	$T \leq 1000$	−7.95E+03	+1.60E+02	+1.96E+00	+1.01E−03	−1.11E−06	+6.51E−10	−1.58E−13	+2.84E+04	+8.40E+00
	$T > 1000$	+2.61E+05	−7.29E+02	+3.31E+00	−4.28E−04	+1.03E−07	−9.43E−12	+2.72E−16	+3.39E+04	−6.67E−01
OH	$T \leq 1000$	−1.99E+03	+9.30E+01	+3.05E+00	+1.52E−03	−3.15E−06	+3.31E−09	−1.13E−12	+2.99E+03	+4.67E+00
	$T > 1000$	+1.01E+06	−2.50E+03	+5.11E+00	+1.30E−04	−8.28E−08	+2.00E−11	+1.55E−15	+2.01E+04	−1.10E+01
NO	$T \leq 1000$	−1.14E+04	+1.53E+02	+3.43E+00	−2.66E−03	+8.48E−06	−7.68E−09	+2.38E−12	+9.09E+03	+6.72E+00
	$T > 1000$	+2.23E+05	−1.28E+03	+5.43E+00	−3.65E−04	+9.88E−08	−1.41E−11	+9.38E−16	+1.75E+04	−8.50E+00

Table 3.3: Perry fuel model constants (ROWLEY et al., 2007), $T_{ref} = 298.15\ K$

Fuel	C_1	C_2	C_3	C_4	C_5	$h(T_{ref})(kJ/(kmol.K))$	$s(T_{ref})(kJ/(kmol.K))$
Methane	+0.33298E+05	+0.79933E+05	+2.0869E+03	+0.41602E+05	+991.96	−7.452E+07	+1.8627E+05

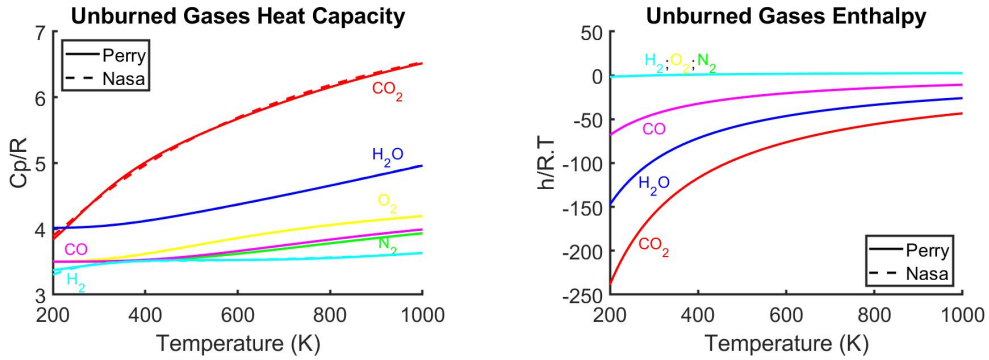

(a) Heat capacity model comparison for the unburned gases.

(b) Enthalpy model comparison for the unburned gases.

Figure 3.4: Unburned gases' heat capacity and enthalpy models.

The choice of Perry's model for the fuel's heat capacity is explained by NASA's unexpected negative slope under 500 K in Figure 3.3a. Ferguson and NASA models show a monotonical increase of the adimensional heat capacity with temperature. However, as we can see in Figure 3.3b, the difference in the values of the heat capacity at lower temperatures does not affect the similarity of the enthalpy values in all three models.

The Perry and NASA's unburned gases models are alike, as we can see in Figure 3.4. The choice of NASA's model for the most of the chemical species was, as described earlier in this work, primarily due to the species that do not appear in the equilibrium state such as the radicals H, OH, O, and NO.

3.2.2 Maxwell's relations

One of the tools used for the simplification of the conservation laws equations is Maxwell's relations. The four most common Maxwell relations are the following:

$$\left(\frac{\partial T}{\partial v}\right)_s = -\left(\frac{\partial P}{\partial s}\right)_v \tag{3-26}$$

$$\left(\frac{\partial T}{\partial P}\right)_s = +\left(\frac{\partial v}{\partial s}\right)_P \tag{3-27}$$

$$\left(\frac{\partial s}{\partial v}\right)_T = +\left(\frac{\partial P}{\partial T}\right)_v \tag{3-28}$$

$$\left(\frac{\partial s}{\partial P}\right)_T = -\left(\frac{\partial v}{\partial T}\right)_P \tag{3-29}$$

These equations represent the equalities of the second derivatives of each of the four thermodynamic potentials (FERGUSON; KIRKPATRICK, 2016),

concerning their thermal variable (temperature T, or entropy s) and their mechanical variable (pressure P, or volume V):

Maxwell's relation makes quantifying entropy changes possible, which cannot be directly measured. Moreover, it facilitates the solution of conservation laws by letting all thermal and mechanical changes be transformed into a single parameter of each nature. In this work, the parameters chosen are pressure and temperature. That's why all change will be ultimately explicit by differentiation in pressure or temperature.

The mixture's specific internal energy can be divided into two specific internal energies (burned and unburned) weighted by their mass fraction.

$$u = u(T, P) = \frac{U}{m} = x_b u_b + (1 - x_b)u_u \ \ [kJ/kg] \tag{3-30}$$

We can now apply the chain rule to both zones. Thus, we must consider the relations 3-18 and 3-19, that highlight the dependence of the internal energy of each zone on in-cylinder pressure and its zone temperature.

$$\frac{du_u}{d\theta} = \frac{\partial u_u}{\partial T_u}\frac{dT_u}{d\theta} + \frac{\partial u_u}{\partial P}\frac{dP}{d\theta} \tag{3-31}$$

$$\frac{du_b}{d\theta} = \frac{\partial u_b}{\partial T_b}\frac{dT_b}{d\theta} + \frac{\partial u_b}{\partial P}\frac{dP}{d\theta} \tag{3-32}$$

To simplify these equations, one can derive an expression for the differentiation of the specific internal energy. Considering pressure and temperature as independent variables and differentiating the definition of enthalpy as a function of temperature, and the fundamental thermodynamic relation as a function of pressure,

$$\frac{\partial h}{\partial T} = \frac{\partial u}{\partial T} + P\frac{\partial v}{\partial T} \rightarrow \frac{\partial u}{\partial T} = c_p - P\frac{\partial v}{\partial T} \tag{3-33}$$

$$\frac{\partial u}{\partial P} = T\frac{\partial s}{\partial P} - P\frac{\partial v}{\partial P} \rightarrow \frac{\partial u}{\partial P} = -T\frac{\partial v}{\partial T} - P\frac{\partial v}{\partial P} \tag{3-34}$$

Substituting these expressions in the equations, 3-31 and 3-32,

$$\frac{du_u}{d\theta} = \left(c_{p,u} - P\frac{\partial v_u}{\partial T_u}\right)\frac{dT_u}{d\theta} - \left(T_u\frac{\partial v_u}{\partial T_u} + P\frac{\partial v_u}{\partial P}\right)\frac{dP}{d\theta} \tag{3-35}$$

$$\frac{du_b}{d\theta} = \left(c_{p,b} - P\frac{\partial v_b}{\partial T_b}\right)\frac{dT_b}{d\theta} - \left(T_b\frac{\partial v_b}{\partial T_b} + P\frac{\partial v_b}{\partial P}\right)\frac{dP}{d\theta} \tag{3-36}$$

Now, these equations are only in function of the specific volume derivatives, temperature, and pressure.

3.3 Conservation Equations

The engine model is based on the equations for mass, energy, and entropy conservation. The independent variables are the derivatives of pressure and temperatures (burned and unburned) regarding the crank angle. The following subsections show the equations that were integrated into the Matlab routine.

3.3.1 Conservation of Mass

The first conservation law to be studied is the conservation of mass. This equation is derived from the equality of cylinder volume and the volumes of the burned and unburned gases (Equation 3-13). If we differentiate the specific volume we find a helpful form of the conservation of mass.

$$\frac{d}{d\theta}\left(\frac{V}{m}\right) = \frac{d}{d\theta}\left(x_b v_b + (1-x_b)v_u\right) \tag{3-37}$$

Expanding the differentiation,

$$\frac{1}{m}\frac{dV}{d\theta} - \frac{V}{m^2}\frac{dm}{d\theta} = x_b\frac{dv_b}{d\theta} + v_b\frac{dx_b}{d\theta} + (1-x_b)\frac{dv_u}{d\theta} - v_u\frac{dx_b}{d\theta} \tag{3-38}$$

Applying the chain rule and rearranging,

$$\left[\frac{1}{m}\frac{dV}{d\theta} - \frac{V}{m^2}\frac{dm}{d\theta}\right] = (v_b - v_u)\frac{dx_b}{d\theta} + x_b\left[\frac{\partial v_b}{\partial T_b}\frac{dT_b}{d\theta} + \frac{\partial v_b}{\partial P}\frac{dP}{d\theta}\right] + (1-x_b)\left[\frac{\partial v_u}{\partial T_u}\frac{dT_u}{d\theta} + \frac{\partial v_u}{\partial P}\frac{dP}{d\theta}\right] \tag{3-39}$$

To simplify resolving the equation, one can put the independent variables in evidence and find the constants that multiply each one of them.

$$A_1\frac{dP}{d\theta} + B_1\frac{dT_u}{d\theta} + C_1\frac{dT_b}{d\theta} = D_1 \tag{3-40}$$

The constant that multiplies the derivative of pressure is

$$A_1 = x_b\frac{\partial v_b}{\partial P} + (1-x_b)\frac{\partial v_u}{\partial P} \tag{3-41}$$

The term that multiplies the unburned temperature derivative is

$$B_1 = (1-x_b)\frac{\partial v_u}{\partial T_u} \tag{3-42}$$

The burned temperature derivative expression is

$$C_1 = x_b \frac{\partial v_b}{\partial T_b} \tag{3-43}$$

Finally, the independent term is

$$D_1 = \frac{1}{m}\frac{dV}{d\theta} - \frac{V}{m^2}\frac{dm}{d\theta} - \frac{dx_b}{d\theta}(v_b - v_u) \tag{3-44}$$

To calculate, the following models are needed: combustion progress, the intake, and the exhaust flows, and the blowby.

3.3.1.1 Combustion Progress

The characteristic feature of the mass fraction burned curve is an initial low slope region beginning with spark ignition and the start of energy release at θ_s, followed by a section of rapid growth and then a more gradual decay. The three regions correspond to the initial ignition development of the flame, the rapid burning region, and the burning completion region.

This S-shaped curve can be represented analytically by an exponential relation, known as a Wiebe function, as given in Equation 3-45:

$$x_b(\theta) = 1 - \exp\left[- a_W \left(\frac{\theta - \theta_s}{\theta_d} \right)^{m_W+1} \right] \ [-] \tag{3-45}$$

where x_b is the mass fraction burned (fraction of energy released), θ is the crank angle (in rad), θ_s is the start of energy release, θ_d is the duration of energy release, m_W is the Wiebe form factor, and a_W is the Wiebe efficiency factor.

Since the cumulative energy release curve asymptotically approaches a value of 1, the end of combustion needs to be defined by an arbitrary limit. In the present work, this limit is defined as 99.9% (FERGUSON; KIRKPATRICK, 2016). Corresponding values of the Wiebe efficiency factor a_W are 2.302, 4.605, and 6.908, respectively. The value of the efficiency factor $a_W = 6.908$ was used by Wiebe in his engine modeling calculations and will also be used in this work (GHOJEL, 2010). It is good to note that the Wiebe parameters depend on the fuel, the engine speed, and the engine load. The proposed model does not consider the Wiebe parameters change with these variables, which augments its errors.

Figure 3.5 plots the cumulative mass fraction burned x_b versus the crank angle for the Engine Specification A (Appendix A). In this case, $a_W = 6.908$, $m_W = 3.0$, $\theta_s = -18\ ^\circ aTDC$, and $\theta_d = 47\ CAD$.

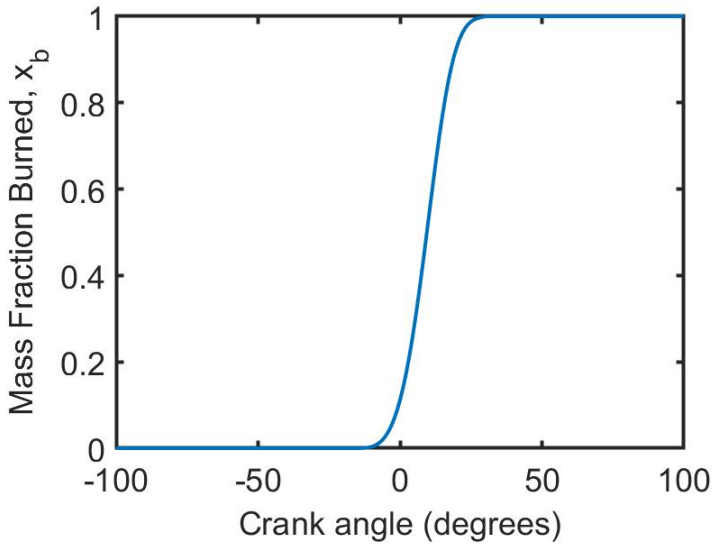

Figure 3.5: Mass fraction burned versus crank angle (Engine Specification in Appendix A).

3.3.1.2 Intake and Exhaust Flow

The most significant airflow restriction in an internal combustion engine is the flow through the intake and exhaust valves (FERGUSON; KIRKPATRICK, 2016). So, it is necessary to have a good valve model to predict the in-cylinder mass and, consequently, the engine's performance parameters.

Yin, in 2017, did extensive work on four-stroke ICEs valve modeling (YIN, 2017). In the present thesis, we use his results to create a simple and robust valve model.

The valve lift motion L_V as a function of the crank angle can be simplified by

$$L_V(\theta) = L_{V_{max}} sin\left[\pi \frac{(\theta - \theta_{VO})}{(\theta_{VC} - \theta_{VO})}\right] \ [m] \tag{3-46}$$

where $L_{V_{max}}$ is the maximum valve lift in m, and θ_{VO} and θ_{VC} are the opening and closing's valve crank angle. Figure 3.6, from the Engine Specification A (Appendix A) illustrates the valve lift model in the Matlab routine. In this engine geometry, the exhaust valve lifts slightly higher than the intake valve. One can notice that there is no valve overlap (intake and exhaust valves opened at the same time).

With the valve geometry, we can calculate the valve's seat area.

$$A_V = \frac{\pi D_V^2}{4} \ [m^2] \tag{3-47}$$

where D_V is the valve seat diameter in m.

Table 3.4: Engine Specification A valve lift parameters

Parameter	Value	Unit
IVO	-360	CAD
IVC	-140	CAD
EVO	$+145$	CAD
EVC	$+360$	CAD
$L^{IV}_{V_{max}}$	8.75	mm
$L^{EV}_{V_{max}}$	8.80	mm

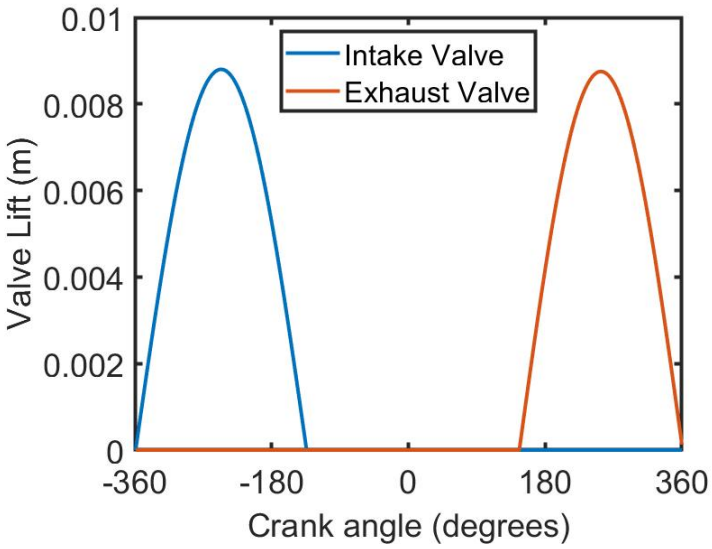

Figure 3.6: Matlab routine valve lift model (Appendix A).

However, not all the seat area is used in the mass flow. The effective valve area can be modeled by

$$A_f = C_f A_V \ \ [m^2] \tag{3-48}$$

where C_f is the flow coefficient. The flow coefficient in the present work will be modeled by the following equation (YIN, 2017):

$$C_f = -0.001 + 3.5477\left(\frac{L_V}{D_V}\right) - 6.566\left(\frac{L_V}{D_V}\right)^2 \ \ [-] \tag{3-49}$$

Assuming that the flow through the valves is one-dimensional quasi-steady compressible flow, we obtain the desired relationship.

$$\dot{m} = \rho_{up} A_f c_{up} \left[\frac{2}{\gamma - 1}\left(\left(\frac{P_{down}}{P_{up}}\right)^{\frac{2}{\gamma}} - \left(\frac{P_{down}}{P_{up}}\right)^{\frac{\gamma+1}{\gamma}}\right)\right]^{\frac{1}{2}} \ \left[\frac{kg}{s}\right] \tag{3-50}$$

where $\dot{m}$ is the mass flow in kg/s, γ is the heat capacity ratio, ρ_{up} is the

upstream gas density, c_{up} is the upstream gas sound speed ($c = \sqrt{\gamma R_{univ} T}$), and P_{up} and P_{down} are the valve's upstream and downstream pressure.

For the intake valve, the upstream conditions are calculated at the intake manifold, and the downstream, are at the cylinder. For the exhaust valve, however, the upstream is at the cylinder, and the downstream is at the exhaust manifold.

3.3.1.3 Blowby

Since the cylinder rings do not provide a complete seal of the combustion chamber, there is leakage of combustion gases or blowby past them. The blowby can affect the indicated performance, the friction and wear, and the hydrocarbon emissions of the engine. The mass flow is assumed to be blowby past the rings from the combustion chamber at a rate proportional to the mass of the cylinder contents (FERGUSON; KIRKPATRICK, 2016).

$$\dot{m}_{bb} = Cm \ \ [kg/s] \tag{3-51}$$

where C is the blowby coefficient in s^{-1}.

New engines will typically have an initial life with 0.5% blowby, then operate for most of their days at a level of 1% blowby, and gradually reach a maximum blowby of 2.5–3.0% at the end of their useful life (FERGUSON; KIRKPATRICK, 2016).

We need to specify h_{bb} (kJ/kg), the enthalpy of the mass loss due to blowby. Early in the combustion process, unburned gas leaks past the rings. Late in the combustion process, burned gas leaks past the rings. Since a larger portion of burned gas will be leaking more than the unburned mass fraction, we will assume after Ferguson (2016) and Kirkpatrick that:

$$h_{bb} = x_b^2 h_b + (1 - x_b^2) h_u \ \ [kJ/kg] \tag{3-52}$$

3.3.2 Conservation of Energy

The differentiation form of the conservation of energy equation is the following:

$$\frac{dU}{d\theta} = \frac{dQ}{d\theta} - P\frac{dV}{d\theta} - \frac{\dot{m}_I h_I}{\omega} \tag{3-53}$$

where U is the internal energy in kJ, Q is the heat transfer in kJ and $\dot{m}_I h_I$ is the liquid energy entering the cylinder in kJ/s, calculated by

$$\dot{m}_I h_I = \dot{m}_{int} h_{int} - \dot{m}_{exh} h_{exh} - \dot{m}_{bb} h_{bb} \tag{3-54}$$

Expanding the internal energy differentiation,

$$\frac{dm}{d\theta}u + m\frac{du}{d\theta} = \frac{dQ}{d\theta} - P\frac{dV}{d\theta} - \frac{\dot{m}_I h_I}{\omega} \tag{3-55}$$

Now, the mass and internal energy can be divided into burned and unburned.

$$\frac{dm}{d\theta}\Big[x_b u_b + (1-x_b)u_u\Big] + m\frac{d}{d\theta}\Big[x_b u_b + (1-x_b)u_u\Big] = \frac{dQ}{d\theta} - P\frac{dV}{d\theta} - \frac{\dot{m}_I h_I}{\omega} \tag{3-56}$$

Expanding,

$$\frac{dm}{d\theta}\Big[x_b u_b + (1-x_b)u_u\Big] + m\left[\frac{dx_b}{d\theta}u_b + x_b\frac{du_b}{d\theta} - \frac{dx_b}{d\theta}u_u + (1-x_b)\frac{du_u}{d\theta}\right] = \frac{dQ}{d\theta} - P\frac{dV}{d\theta} - \frac{\dot{m}_I h_I}{\omega} \tag{3-57}$$

Now, we can substitute the specific internal energy derivative.

$$\begin{aligned}&\frac{dm}{d\theta}\Big[x_b u_b + (1-x_b)u_u\Big] + \\ &\quad m\Bigg\{\frac{dx_b}{d\theta}(u_b - u_u) + x_b\left[\Big(c_{p,b} - P\frac{\partial v_b}{\partial T_b}\Big)\frac{dT_b}{d\theta} - \Big(T_b\frac{\partial v_b}{\partial T_b} + P\frac{\partial v_b}{\partial P}\Big)\frac{dP}{d\theta}\right] + \\ &\qquad (1-x_b)\left[\Big(c_{p,u} - P\frac{\partial v_u}{\partial T_u}\Big)\frac{dT_u}{d\theta} - \Big(T_b\frac{\partial v_u}{\partial T_u} + P\frac{\partial v_u}{\partial P}\Big)\frac{dP}{d\theta}\right]\Bigg\} \\ &\qquad = \frac{dQ}{d\theta} - P\frac{dV}{d\theta} - \frac{\dot{m}_I h_I}{\omega}\end{aligned} \tag{3-58}$$

As done in the conservation of mass equation, we can put in evidence the independent variables.

$$A_2\frac{dP}{d\theta} + B_2\frac{dT_u}{d\theta} + C_2\frac{dT_b}{d\theta} = D_2 \tag{3-59}$$

The multiplying constants A_2, B_2, C_2, and D_2 are the following:

$$A_2 = -m\left[x_b\left(T_b\frac{\partial v_b}{\partial T_b} + P\frac{\partial v_b}{\partial P}\right) + (1-x_b)\left(T_u\frac{\partial v_u}{\partial T_u} + P\frac{\partial v_u}{\partial P}\right)\right] \tag{3-60}$$

$$B_2 = m(1-x_b)\left(c_{p,u} - P\frac{\partial v_u}{\partial T_u}\right) \tag{3-61}$$

$$C_2 = mx_b\left(c_{p,b} - P\frac{\partial v_b}{\partial T_b}\right) \tag{3-62}$$

$$D_2 = \frac{dQ}{d\theta} - P\frac{dV}{d\theta} - \frac{\dot{m}_I h_I}{\omega} - \frac{dm}{d\theta}\Big[x_b u_b + (1-x_b)u_u\Big] - m\frac{dx_b}{d\theta}(u_b - u_u) \tag{3-63}$$

To solve this equation, four models must be considered: the heat transfer, the burned mass initial temperature, the auto-ignition, and the SACI combustion technique.

3.3.2.1 Heat Transfer

A classic correlation for the instantaneous cylinder average heat transfer coefficient, α, between the cylinder and the coolant was developed by Woschni (WOSCHNI, 1967).

The Woschni correlation uses a variable characteristic gas velocity to account for the increased gas velocity induced by combustion. The Woschni correlation is

$$Nu = 0.035\ Re^{0.8}\ [-] \tag{3-64}$$

where Nu is the Nusselt number of the gas, and Re is the flow's Reynolds number, calculated by

$$Re = \frac{\rho_f S_f L_c}{\mu_f}\ [-] \tag{3-65}$$

where ρ_f is the fluid's density in kg/m^3, S_f is the characteristic fluid velocity in m/s, L_c is the characteristic length in m, and μ_f is the fluid's dynamic viscosity in $Pa.s$.

The characteristic gas velocity in the Woschni correlation is proportional to the mean piston speed during intake, compression, and exhaust. During combustion and expansion, when the valves are closed, we assume that the gas velocities are higher because of the combustion process. The average cylinder gas velocity, in m/s, is modeled with the following equation:

$$w = C_1\ \overline{S_p} + C_2\ T_{IVC} \cdot \frac{V_d}{V_{IVC}} \cdot \frac{P - P_m}{P_{IVC}}\ [m/s] \tag{3-66}$$

where $\overline{S_p}$ is the mean piston speed (m/s), T_{IVC} is the temperature at intake valve closing (K), V_{IVC} is the cylinder volume at intake valve closing (m^3), P_{IVC} is the pressure at intake valve closing (kPa), P_m is the motored pressure (kPa), and C_1 and C_2 are the Woschni constants.

Table 3.5 shows the Woschni constants for each cycle phase (HEYWOOD, 1988).

Table 3.5: Woschni constants (HEYWOOD, 1988)

	C_1	C_2
Gas exchange period	6.18	0
Compression period	2.28	0
Combustion and expansion period	2.28	$3.24 \cdot 10^{-3}$

Finally, the heat transfer coefficient is calculated by the following equation:

$$\alpha = 3.26\ B(m)^{-0.2}\ P(kPa)^{0.8}\ T(K)^{-0.55}\ w(m/s)^{0.8}\ \ [kW/(m^2.K)] \qquad (3\text{-}67)$$

Both burned and unburned volumes have their own Woschni heat transfer coefficient. To find the average heat transfer coefficient, we calculate

$$\alpha = \sqrt{x_b}\ \alpha_b(P, T_b) + (1 - \sqrt{x_b})\ \alpha_u(P, T_u)\ \ [kW/m^2.K] \qquad (3\text{-}68)$$

Figure 3.7 shows the cylinder's instantaneous average heat transfer coefficient plotted along the crank angle. The heat transfer will be higher at the power stroke, when the crank angle is closer to the TDC. We can note that due to the change in the Woschni constants at every phase, the heat transfer coefficient is not continuous.

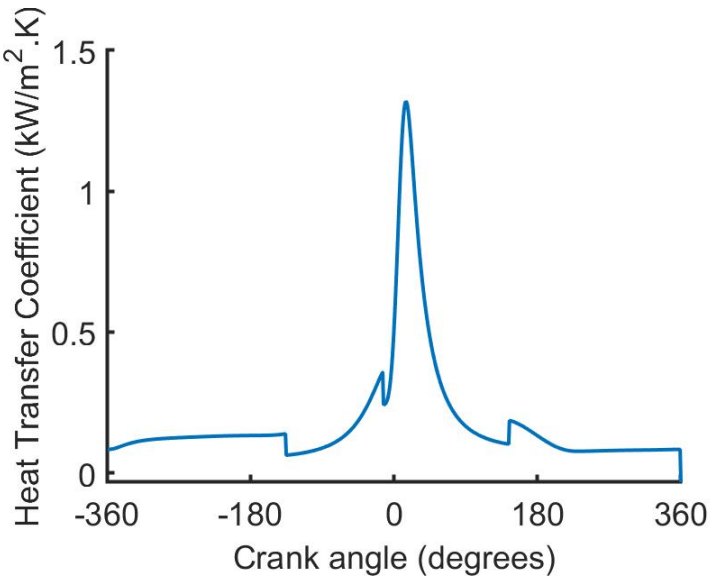

Figure 3.7: Instantaneous Cylinder Average Heat Transfer Coefficient (Engine Specification in Appendix A).

3.3.2.2 Burned Mass Initial Temperature

When the chemical reaction starts, one needs to define the temperature of the first mass burned. A common approach is to set the first burned mass temperature as the adiabatic flame temperature. It is defined as the temperature of the combustion products when completely burned with no shaft work ($W = 0$) or heat transfer ($Q = 0$) to the surroundings.

Since the product temperature is generally unknown in first law combustion calculations, iteration with an initial temperature estimate is required to determine the product mixture enthalpy. For constant pressure combustion, the first law of thermodynamics with no work or heat transfer to the surroundings is

$$H_p = H_r \tag{3-69}$$

where H_p is the enthalpy of the product gases in kJ and H_r is the enthalpy of the reactant gases, also in kJ. From this equation, the adiabatic flame temperature can be found.

3.3.2.3 Auto-ignition

According to the current scientific literature, two different approaches may be followed for auto-ignition prediction in thermodynamic simulations: the detailed chemical kinetic approach and the auto-ignition delay approach. The first takes the basic reaction steps that occur during combustion into account, but, due to the great number of reactions to consider, these models require a great computational effort and are often difficult to implement. The auto-ignition delay approach, instead, is based on the unburned gas pressure and temperature history and, although less accurate than the first approach, is quite easy to implement in zero-dimensional simulations; for this reason, this approach is often preferred for the estimation of the auto-ignition time of fuel-air mixtures (PIPITONE; BECCARI, 2018).

One way to model knock is to suppose that there is a critical mass fraction of combustion precursors that if attained anywhere within the unburned gas, will cause auto-ignition. Knock will occur prior to the end of the normal flame-front propagation if the integrated rate of formation equals this critical mass fraction.

The extent of precursor reaction is defined as

$$\zeta = \frac{x_p}{x_c} \ [-] \tag{3-70}$$

where x_p is the precursor mass fraction and x_c is the critical mass fraction to auto-ignition.

The normalized rate of formation of precursors is represented by the following equation:

$$\frac{d\zeta}{dt} = \frac{1}{x_c}\frac{dx_p}{dt} = \frac{1}{\tau} \ [s^{-1}] \tag{3-71}$$

where τ is the auto-ignition delay time in s. This property is commonly modeled based on Arrhenius type equations:

$$\tau = a_{AI} \ P^{-n_{AI}} \ \exp\left[\frac{Ea_{AI}}{RT}\right] = a_{AI} \ P^{-n_{AI}} \ \exp\left[\frac{b_{AI}}{T}\right] \ [s] \tag{3-72}$$

where, P (bar) and T (K) are the pressure and temperature of the air-fuel mixture inside the engine cylinder, a_{AI} and n_{AI} are auto-ignition constants, and Ea_{AI} $(kJ/kmol)$ and b_{AI} (K) are auto-ignition activation energy constants.

Pipiton and Beccari (2018) did multiple experiments with methane and approximated the auto-ignition constants as the following: $a_{AI} = 0.0056$, $b_{AI} = 11875$, and $n_{AI} = 3.25$ (PIPITONE; BECCARI, 2018). This model is the Knock-Integral mechanism that is used in the Matlab routine. Once we have the auto-ignition constants, it is possible to calculate the knock-integral.

$$KI(t) = \zeta(t) = \int_{t_{IVC}}^{t} \frac{d\zeta}{dt}dt = \int_{t_{IVC}}^{t} \frac{1}{\tau}dt \ [-] \tag{3-73}$$

According to this approach, the knock integral reaches the value of 1 when auto-ignition occurs (i.e., when the radical species in the unburned gas reach the critical concentration), hence:

$$KI(t_{AI}) = \int_{t_{IVC}}^{t_{AI}} \frac{1}{\tau}dt = 1 \tag{3-74}$$

Equations 3-72 and 3-74 together allow to determine the time t_{KO} at which knock occurs.

One can notice that the Knock-Integral and the extent of precursor reaction can be calculated as a function of the crank angle, instead of the time, as we see in Equation 3-75.

$$\zeta = \frac{1}{\dot{\theta}} \int_{\theta_{IVC}}^{\theta} \frac{d\zeta}{dt}d\theta \tag{3-75}$$

3.3.2.4 SACI technique

To model the SACI combustion technique, we will divide the combustion into two zones: SI and HCCI. The engine will start in SI mode. In this mode,

the flame-front will propagate in the cylinder volume represented by the Wiebe function (with Wiebe constants related to SI combustion). The program will then recalculate the extent of precursor reaction (Knock-integral) at every crank angle step.

If the Knock-Integral reaches one before the end of combustion, the rest of the unburned mass will burn with an HCCI combustion rate (with Wiebe constants related to HCCI combustion).

This schema is represented in the Equation 3-76.

$$x_b = \begin{cases} 1 - \exp\left[- a_W^{\mathrm{SI}} \left(\frac{\theta - \theta_s^{\mathrm{SI}}}{\theta_d^{\mathrm{SI}}} \right)^{m_W^{\mathrm{SI}}+1} \right], \text{ if } \zeta < 1 \\ 1 - \exp\left[- a_W^{\mathrm{HCCI}} \left(\frac{\theta - \theta_s^{*}}{\theta_d^{\mathrm{HCCI}}} \right)^{m_W^{\mathrm{HCCI}}+1} \right], \text{ if } \zeta = 1 \end{cases} \tag{3-76}$$

where,

$$\theta_s^* = \theta_{\mathrm{SOHCCI}} - \theta_d^{\mathrm{HCCI}} \cdot \left(\frac{\theta_{\mathrm{SOHCCI}} - \theta_s^{\mathrm{SI}}}{\theta_d^{\mathrm{HCCI}}} \right)^{\frac{m_W^{\mathrm{SI}}+1}{m_W^{\mathrm{HCCI}}+1}} \ [CAD] \tag{3-77}$$

and,

$$\zeta(\theta_{\mathrm{SOHCCI}}) = 1 \tag{3-78}$$

3.3.3 Conservation of Entropy (Unburned Volume)

Since three independent variables and two equations (conservation of mass and energy) are already defined, another equation is necessary. Because of its simplicity, the conservation of entropy on the unburned volume is chosen. Treating it as an open system losing mass via leakage and combustion, it can be showed that

$$\frac{dS_u}{d\theta} = \frac{d}{d\theta}(m_u s_u) = -\frac{1}{T_u}\frac{\dot{Q}_u}{\omega} \tag{3-79}$$

where $\dot{Q}_u$ is the heat loss in the unburned volume in kW, calculated by

$$\dot{Q}_u = \alpha_u A_u (T_u - T_w) \ [kW] \tag{3-80}$$

and

$$A_u = (1 - \sqrt{x_b}) A(\theta) \ [m^2] \tag{3-81}$$

Expanding the derivatives on the left-hand side of the equation,

$$\frac{dm}{d\theta}(1 - x_b)s_u - m\frac{dx_b}{d\theta}s_u + m(1 - x_b)\frac{ds_u}{d\theta} = -\frac{1}{T_i}\frac{\dot{Q}_u}{\omega} \tag{3-82}$$

Substituting the entropy derivative by the expressions obtained in Maxwell's relations,

$$\frac{dm}{d\theta}(1-x_b)s_u - m\frac{dx_b}{d\theta}s_u + m(1-x_b)\left[\frac{c_{p,u}}{T_u}\frac{dT_u}{d\theta} - \frac{\partial v_u}{\partial T_u}\frac{dP}{d\theta}\right] = -\frac{1}{T_i}\frac{\dot{Q}_u}{\omega} \quad (3\text{-}83)$$

Now, we can obtain the same type of equation as in the conservation of mass and energy.

$$A_3\frac{dP}{d\theta} + B_3\frac{dT_u}{d\theta} + C_3\frac{dT_b}{d\theta} = D_3 \quad (3\text{-}84)$$

The A_3, B_3, C_3, and D_3 constants are:

$$A_3 = -m(1-x_b)\frac{\partial v_u}{\partial T_u} \quad (3\text{-}85)$$

$$B_3 = m(1-x_b)\frac{c_{p,u}}{T_u} \quad (3\text{-}86)$$

$$C_3 = 0 \quad (3\text{-}87)$$

$$D_3 = -\frac{1}{T_u}\frac{\dot{Q}_u}{\omega} + m\frac{dx_b}{d\theta}s_u - \frac{dm}{d\theta}(1-x_b)s_u \quad (3\text{-}88)$$

3.4 Chemical Equilibrium

In this work, the chemical combustion reaction is based on an equilibrium constant method (OLIKARA; BORMAN, 1975).

3.4.1 Equilibrium Constant Method

When we use equilibrium constants to solve chemical reactions instead of the minimization of the Gibbs free energy, the algebra performed is less complex than the Lagrange multiplier approach (minimization of Gibbs free energy), considering that the species list is restricted. Assuming that the only product species of importance resulting from dissociation are the radicals O, H, OH, and NO, the present work considers only ten product species. The chemical reaction per mole of fuel is

$$\begin{aligned}\mathrm{C}_a\mathrm{H}_b\mathrm{O}_c\mathrm{N}_d + \frac{a_s}{\phi}(\mathrm{O}_2 + 3.76\mathrm{N}_2) \rightarrow\ & n_1\mathrm{CO}_2 + n_2\mathrm{H}_2\mathrm{O} + n_3\mathrm{N}_2 \\ & + n_4\mathrm{O}_2 + n_5\mathrm{CO} + n_6\mathrm{H}_2 + n_7\mathrm{H} + n_8\mathrm{O} + n_9\mathrm{OH} + n_{10}\mathrm{NO} \quad (3\text{-}89)\end{aligned}$$

The fuel is initially mixed with air with an equivalence ratio ϕ, temperature T_u and pressure P. After combustion, the products of the reaction are assumed to be in equilibrium at temperature T_b and pressure P. The composition and thermodynamic properties of the product mixture are to be determined.

Atom balancing yields the following four equations:

$$\begin{cases} \text{C} : a = (y_1 + y_5)\ n \\ \text{H} : b = (2y_2 + 2y_6 + y_7 + y_9)\ n \\ \text{O} : c + 2\frac{a_s}{\phi} = (2y_1 + y_2 + 2y_4 + y_5 + y_8 + y_9 + y_{10})\ n \\ \text{N} : d + 7.52\frac{a_s}{\phi} = (2y_3 + y_{10})\ n \end{cases} \tag{3-90}$$

where n is the amount of substance in the gaseous phase.

From these equations, we can define three constants:

$$\begin{cases} d_1 = \frac{b}{a} \\ d_2 = \frac{c}{a} + 2\frac{a_s}{\phi} \\ d_3 = \frac{b}{a} + 7.52\frac{a_s}{\phi} \end{cases} \tag{3-91}$$

Upon substitution into the atom balance equations, and with some rearrangement,

$$\begin{cases} 2y_2 + 2y_6 + y_7 + y_9 + d_1 y_1 - d_1 y_5 = 0 \\ 2y_1 + y_2 + 2y_4 + y_5 + y_8 + y_9 + y_{10} - d_2 y_1 - d_2 y_5 = 0 \\ 2y_3 + y_{10} - d_3 y_1 - d_3 y_5 = 0 \\ \sum_{i=1}^{10} y_i = 1 \end{cases} \tag{3-92}$$

For now, we have ten variables and only four equations. We need six more equations to have an independent system. These equations come from six gas-phase equilibrium reactions. These reactions include the dissociation of hydrogen, oxygen, water, and carbon dioxide, and the formation of OH and NO radicals:

$$\begin{aligned} \tfrac{1}{2}\text{H}_2 &\rightleftharpoons \text{H} & K_1 &= \frac{y_7 P^{1/2}}{y_6^{1/2}} \\ \tfrac{1}{2}\text{O}_2 &\rightleftharpoons \text{O} & K_2 &= \frac{y_8 P^{1/2}}{y_4^{1/2}} \\ \tfrac{1}{2}\text{H}_2 + \tfrac{1}{2}\text{O}_2 &\rightleftharpoons \text{OH} & K_3 &= \frac{y_9}{y_4^{1/2} y_6^{1/2}} \\ \tfrac{1}{2}\text{O}_2 + \tfrac{1}{2}\text{N}_2 &\rightleftharpoons \text{NO} & K_4 &= \frac{y_{10}}{y_4^{1/2} y_3^{1/2}} \\ \text{H}_2 + \tfrac{1}{2}\text{O}_2 &\rightleftharpoons \text{H}_2\text{O} & K_5 &= \frac{y_2}{y_4^{1/2} y_6 P^{1/2}} \\ \text{CO} + \tfrac{1}{2}\text{O}_2 &\rightleftharpoons \text{CO}_2 & K_6 &= \frac{y_1}{y_4^{1/2} y_5 P^{1/2}} \end{aligned} \tag{3-93}$$

The unit of pressure in the above six equations is in units of atmospheres (atm). Olikara and Borman (OLIKARA; BORMAN, 1975) have curve fitted the equilibrium constants ($K_i(T)$) to JANAF Table data for the temperature range 600 < T < 4000 K.

$$log_{10}K_i(T) = A_i ln(T/1000) + \frac{B_i}{T} + C_i + D_i T + E_i T^2 \qquad (3\text{-}94)$$

where T is in Kelvin. The equilibrium constant $K_i(T)$ curve-fit coefficients are listed in Table 3.6.

Table 3.6: Equilibrium constant K_i curve-fit coefficients

K_i	A_i	B_i	C_i	D_i	E_i
K_1	+0.432E+00	−0.112E+05	+0.267E+01	−0.745E−04	+0.242E−08
K_2	+0.310E+00	−0.129E+05	+0.321E+01	−0.738E−04	+0.344E−08
K_3	−0.141E+00	−0.213E+04	+0.853E+00	+0.355E−04	−0.310E−08
K_4	+0.150E−01	−0.470E+04	+0.646E+00	+0.272E−05	−0.154E−08
K_5	−0.752E+00	+0.124E+05	−0.260E+01	+0.259E−03	−0.162E−07
K_6	−0.415E−02	+0.148E+05	−0.475E+01	+0.124E−03	−0.900E−08

With the mixture mole fraction composition known, one can proceed to compute the thermodynamic properties of interest: specific heat, enthalpy, entropy, specific volume, and internal energy for the given conditions.

Figure 3.8 shows the result from the created Matlab routine for the in-cylinder chemical species. We can promptly see the influence of intake, combustion, and exhaust strokes on the species.

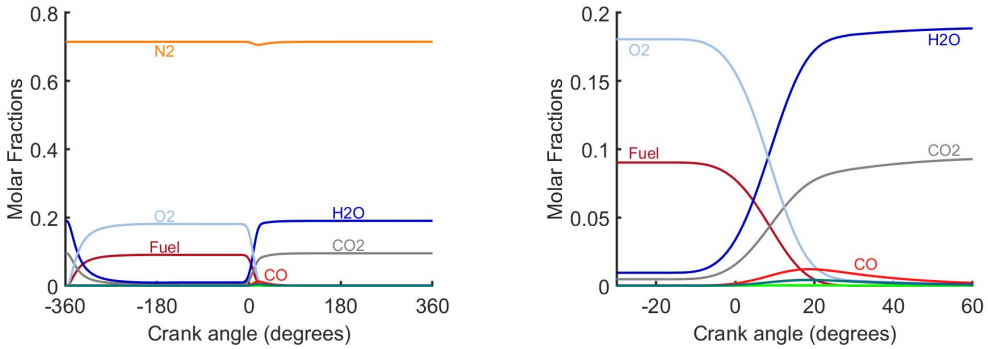

(a) Major species molar fractions.

(b) Combustion phase zoom.

Figure 3.8: ICE species molar fractions over the crank angle (Engine Specification A) - Appendix A

The air-fuel mixture that is directly impacted by the combustion (Fuel and O_2) see their molecular fraction augment in the intake stroke. Then, they

are consumed in the combustion and their molecular fraction are transformed into the burned gases (primarily H_2O, CO_2, and CO).

The minor species are illustrated in Figure 3.9. It is possible to see their behavior with oxygen consumption as a reference. Since the scale is large, the minor species molar fractions are multiplied to fit the graph.

The minor species with the highest molar fraction is the radical OH, followed by the radical NO and H_2. The greatest growth of these minor species happens at the moment of maximum consumption of oxygen. Furthermore, their maximum values are reached at the end of the O_2 consumption.

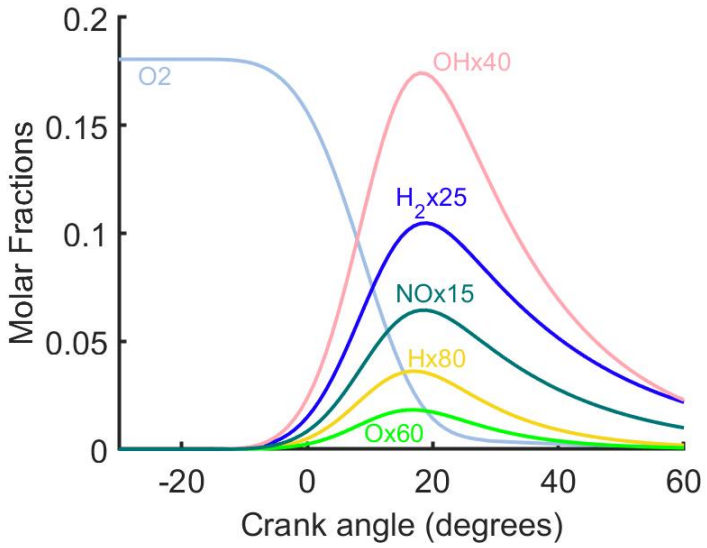

Figure 3.9: Minor species molar fractions as a function of the crank angle.

It is important to say that the fuel and the combustion products are predicted on the unburned and burned volume. So, if the fuel or the oxygen does not react, it is accounted as a burned mass at the end of the combustion. Thus, everything in the cylinder is *burned* at the end of the combustion phase. Similarly, when the intake valves open at the start of the cycle, there is burned mass inside the cylinder. This burned mass (burned residual) is considered an *unburned* mass with combustion products species. It means that inside the cylinder at the start of the cycle there is *unburned* gas, even though the mixture presents burned species.

3.4.2 NOx Emissions - Zeldovich Mechanism

The most important chemical tool for internal combustion engines that produce NO is the Zeldovich mechanism, also called the thermal mechanism. I this model, NO is formed in the high-temperature burned gases behind the flame front.

The following three chemical equations form the extended Zeldovich reaction mechanism (MILLER; BOWMAN, 1989):

$$\mathrm{O} + \mathrm{N_2} \underset{k_{1,bwd}}{\overset{k_{1,fwd}}{\rightleftharpoons}} \mathrm{NO} + \mathrm{N} \tag{3-95}$$

$$\mathrm{N} + \mathrm{O_2} \underset{k_{2,bwd}}{\overset{k_{2,fwd}}{\rightleftharpoons}} \mathrm{NO} + \mathrm{O} \tag{3-96}$$

$$\mathrm{N} + \mathrm{OH} \underset{k_{3,bwd}}{\overset{k_{3,fwd}}{\rightleftharpoons}} \mathrm{NO} + \mathrm{H} \tag{3-97}$$

where k is the rate constant in $cm^3/(mol.s)$, and the subscripts fwd and bwd indicate the forward and backward reactions, respectively.

The rate constants for the extended Zeldovich reaction mechanism are given in Equation 3-98.

$$k_{Ze} = A_{Ze} \cdot 10^{n_{Ze}} \exp(-B_{Ze}/T) \ \ [cm^3/(mol.s)] \tag{3-98}$$

The coefficients for each rate constant are shown in Table 3.7, (HANSON; SALIMIAN, 1984).

Table 3.7: Zeldovich extended mechanism constants (HANSON; SALIMIAN, 1984)

Reaction	A_{Ze}	B_{Ze}	n_{Ze}
1 - Forward	1.8	38,370	14
1 - Backward	3.8	425	13
2 - Forward	1.8	4,680	10
2 - Backward	3.8	20,820	9
3 - Forward	7.1	450	13
3 - Backward	1.7	24,560	14

After Heywood (HEYWOOD, 1976), one can write the following expression for the rate of change of nitric oxide concentration in, with the brackets denoting molar concentrations in units of mol/cm^3.

$$\frac{d}{dt}[\mathrm{NO}] = +k_{1,fwd}[\mathrm{O}][\mathrm{N_2}] - k_{1,bwd}[\mathrm{NO}][\mathrm{N}] + k_{2,fwd}[\mathrm{N}][\mathrm{O_2}] - k_{2,bwd}[\mathrm{NO}][\mathrm{O}] + k_{3,fwd}[\mathrm{N}][\mathrm{OH}] - k_{3,bwd}[\mathrm{NO}][\mathrm{H}] \tag{3-99}$$

Two approximations are introduced: first, that the C-O-H system is in equilibrium and is not perturbed by N2 dissociation, and second, the N atoms change concentration by a quasi-steady process. With these approximations, it can be shown that

$$\frac{d[\mathrm{NO}]}{dt} = \frac{2R_1(1-\xi^2)}{1+\xi R_1/(R_2+R_3)} \ [mol/(cm^3.s)] \tag{3-100}$$

where where ξ is the ratio of the nitric oxide concentration to its equilibrium value ($\xi = \frac{[\mathrm{NO}]}{[\mathrm{NO}]_e}$), and R_i ($i = 1, 2, 3$) are rates of reaction, with the equilibrium concentrations with the subscript e:

$$\begin{cases} R_1 = k_{1,fwd}[\mathrm{O}]_e[\mathrm{N}_2]_e \\ R_2 = k_{2,bwd}[\mathrm{NO}]_e[\mathrm{O}]_e \\ R_3 = k_{3,bwd}[\mathrm{NO}]_e[\mathrm{H}]_e \end{cases} \tag{3-101}$$

Finally, the total amount of nitric oxide that appears in the exhaust is computed by summing the mass fractions for all the fluid elements ($\widetilde{x}_{\mathrm{NO}} = \int_0^1 x_{\mathrm{NO}} dx$).

3.5 Numerical Integration

To resolve a linear system of equations of three independent variables, we need three independent equations to have a single solution. In this work, the three independent variables are the pressure and temperatures (burned and unburned) derivatives concerning the crank angle. For these three variables, we have three equations: conservation of mass, conservation of energy, and conservation of entropy in the unburned zone.

Hence, we have a closed and well-defined problem called an "independent system". The system of equations to be solved represented in a matrix form is

$$\begin{bmatrix} A_1 & B_1 & C_1 \\ A_2 & B_2 & C_2 \\ A_3 & B_3 & C_3 \end{bmatrix} \cdot \begin{bmatrix} \frac{dP}{d\theta} \\ \frac{dT_u}{d\theta} \\ \frac{dT_b}{d\theta} \end{bmatrix} = \begin{bmatrix} D_1 \\ D_2 \\ D_3 \end{bmatrix} \tag{3-102}$$

Once we have the solution of this system of equations, we need to solve three differential equations to calculate the properties (P, T_u and T_b) of the next simulation step.

One can notice that the system of equations at the intake, compression, and exhaust strokes have only two independent variables, and therefore, two equations. In the intake and compression strokes, there are no burned gases, so there is no need to calculate the burned temperature. In the exhaust stroke, there are no unburned gases, making it only two independent variables as well. In these cases, only conservation of mass and energy equations are necessary to be calculated. At the power stroke, however, there are both burned and

unburned gases. In this case, we need all three conservation equations to resolve the problem.

$$\begin{bmatrix} A_1 & B_1 \\ A_2 & B_2 \end{bmatrix} \cdot \begin{bmatrix} \frac{dP}{d\theta} \\ \frac{dT_u}{d\theta} \end{bmatrix} = \begin{bmatrix} D_1 \\ D_2 \end{bmatrix} \tag{3-103}$$

$$\begin{bmatrix} A_1 & C_1 \\ A_2 & C_2 \end{bmatrix} \cdot \begin{bmatrix} \frac{dP}{d\theta} \\ \frac{dT_b}{d\theta} \end{bmatrix} = \begin{bmatrix} D_1 \\ D_2 \end{bmatrix} \tag{3-104}$$

These differential equations are solved in the Matlab routine by the function *ode45*, which is a Matlab differential equations solver that uses the Dormand–Prince (RKDP) method. This method, a member of the Runge–Kutta family of ODE solvers, uses six function evaluations to calculate fourth- and fifth-order accurate solutions.

3.5.1 Explicit Runge-Kutta Method

The explicit Runge–Kutta method is an iterative method that includes the Euler Method routine, used in temporal discretization for the approximate solutions of ordinary differential equations (ZHENG; ZHANG, 2017).

An initial value problem, as it is in the present work, is specified as

$$\frac{dy}{dt} = f(t, y), \; y(t_0) = y_0 \tag{3-105}$$

where y is an unknown function of time t, which we would like to approximate, the function f and the initial conditions t_0, y_0 are given.

The approximation of the next simulation step for P, T_u and T_b in the Runge-Kutta method is calculated by

$$y_{n+1} = y_n + h \sum_{i=1}^{s} b_i k_i \tag{3-106}$$

where y_{n+1} is the calculated approximation, y_n, the known previous step, h is the step size, and b_i and k_i are the weights and estimated slopes, respectively (ZHENG; ZHANG, 2017).

The estimated slopes' calculations are the following:

$$\begin{cases} k_1 = f(t_n, y_n), \\ k_2 = f(t_n + c_2 h, y_n + h(a_{21} k_1)), \\ \vdots \\ k_s = f(t_n + c_s h, y_n + h(a_{s1} k_1 + a_{s2} k_2 + \cdots + a_{s,s-1} k_{s-1})). \end{cases} \tag{3-107}$$

These pieces of information can be arranged in a unique table, called the Butcher Table.

Table 3.8: Runge-Kutta Butcher Table

0					
c_2	a_{21}				
c_3	a_{31}	a_{32}			
$\vdots$	$\vdots$	$\vdots$	$\ddots$		
c_s	a_{s1}	a_{s2}	$\dots$	$a_{s,s-1}$	
	b_1	b_2	$\dots$	b_{s-1}	b_s

3.5.2 Dormand–Prince method (RKDP)

The Dormand–Prince (RKDP) method's Butcher Table is

Table 3.9: RKDP Butcher Table

0							
1/5	1/5						
3/10	3/40	9/40					
4/5	44/45	−56/15	32/9				
8/9	19372/6561	−25360/2187	64448/6561	−212/729			
1	9017/3168	−355/33	46732/5247	49/176	−5103/18656		
1	35/384	0	500/1113	125/192	−2187/6784	11/84	
	35/384	0	500/1113	125/192	−2187/6784	11/84	0

with it, it is possible to calculate fourth- and fifth-order accurate Runge-Kutta solutions. The difference between these solutions is then taken to be the error of the (fourth-order) solution (KIMURA, 2009). The simulation step in this work is

$$h = \Delta\theta = 1^\circ = 1\,\text{deg} \tag{3-108}$$

It is noteworthy that this simulation step is used as the initial and final point of the *ode45* integration, with a relative error of 0.1 %. The Matlab

function optimises the step size within this simulation step: ff the error is above a given tolerance, the step size is decreased until the error is below that tolerance. If the error is far below that tolerance, the step size in increased to save time.

If we choose a small simulation step, the simulation will be more accurate. Nonetheless, the calculation will be slower. For this, the chosen time step for 0D internal combustion engines simulation is 1 deg (FERGUSON; KIRKPATRICK, 2016) with a relative error of 0.1 %. The simulation results with smaller simulation step sizes are not very different, and the calculation procedure is more demanding.

3.5.3 Convergence Criteria

The internal combustion engine is a heat engine that works in a cycle. So it has to present some cyclic properties. The mass, the pressure, and the temperature at the beginning must be the same as at the end. Furthermore, the initial unburned gas temperature (and molar fractions) must be the same, or at least similar, to the burned gas temperature at the end of the cycle. Thus, it was modeled convergence criteria to force these cyclic properties.

The engine simulation will run until the two convergence criteria are met simultaneously. Both pressure and temperature must have a maximum error of the relative difference between initial and final values of 5 %. These criteria are: $\left|\frac{P_i - P_f}{P_i}\right| < 5\%$ and $\left|\frac{T_{u,i} - T_{b,f}}{T_{u,i}}\right| < 5\%$.

The routine compares the initial and final values of pressure and temperature at the end of the cycle. If the convergence requirements are not met, it restarts with the new initial values as the final values. If the convergence is not satisfied until the 20^{th} try, the program stops.

The use of the simulator showed that the convergence is reached normally in the third or fourth cycle.

4
Methodology

Now that the internal combustion engine simulator is modeled, we need to develop a methodology for studying its parameters. The simplicity of the Matlab routine makes it the easy to change them. So, the study of multiple parameters sensitivity is simple to implement, but not as simple to interpret. Furthermore, the simulator gives several performance parameters to analyze, which significantly augment the data to be studied and the interpretations to be done.

There are multiple ways to study the parameters' sensibility in a process. The most common one is the Univariate Analysis (UA). In this method, the data has only one variable, which requires the analysis of each variable separately. This type of analysis needs a great amount of data to study multiple variables. Moreover, it does not consider the relations between these factors.

Another well-known approach is the use of a design of experiments (DoE) that allows the investigation of more than one variable and considers possible interaction between the factors in an empirical mathematical model. One of the most common design is the Central Composite Design (CCD), which considers data from fractional factorial design with center points and curvature points. It is commonly used in response surface methodology for building a second-order model for the response variable without needing to use a complete three-level factorial experiment (ANTHONY, 2003). Although it is harder to analyze than UA, it has two-factors relations and optimizes data operating points. That's why the simulator will operate in a CCD design.

4.1
Central Composite Design

A Box-Wilson Central Composite Design, also called "central composite design", is an experimental fractional (blue points in Figure 4.1) design, supplemented by additional ones such as center points and star points (red points).

If we define the distance from the center of the design space to a factorial point as ± 1 unit for each factor, the distance from the center of the design space to a star point is $|\alpha| > 1$. The precise value of α depends on some properties desired for the design and the number of factors involved (NIST/SEMATECH, 2012).

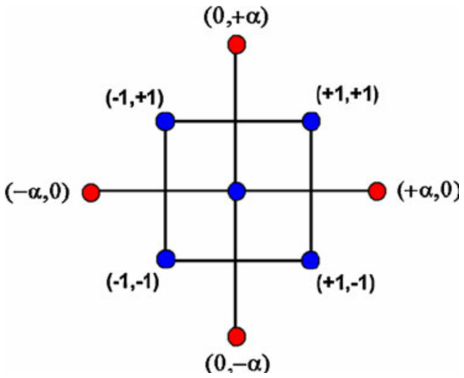

Figure 4.1: Central Composite Design of Experiments.

In this study, we want the main effects to be separately estimated. Thus, an Orthogonal Design (OD), in which the given factors (or a linear combination of them) are seen as statistically independent, is a good choice of property. Additionally, a Rotatable Design (RD), which has equal predictiveness in all directions from equidistant points from the center point, is an interesting trait to have in the design of experiments (DoE) (HAMI; POUGNET, 2015).

Figure 4.2 illustrates the different designs of CCD and their prediction variances into the domain studied.

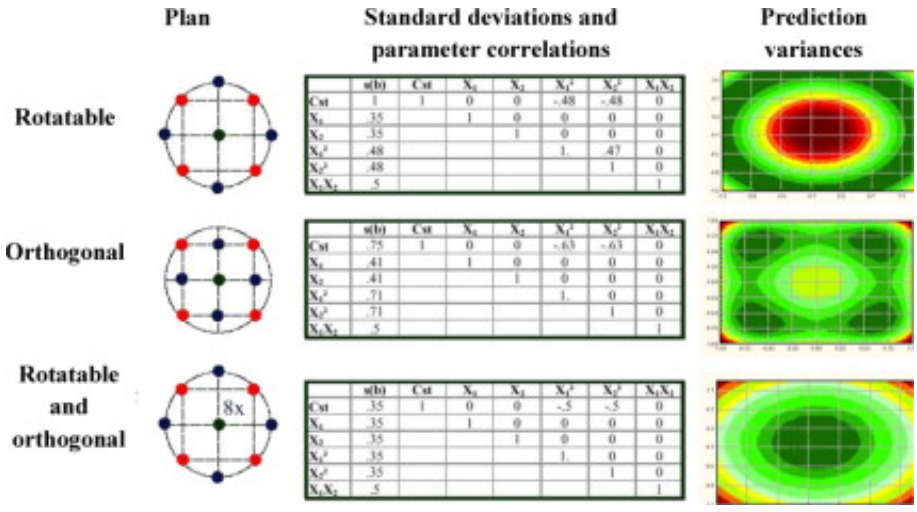

Figure 4.2: CCD types (HAMI; POUGNET, 2015).

The Rotatable and Orthogonal Central Composite Design (ROCCD) adds the equal predictive power in all directions from the RD with the statistical independence of variables from the OD. Then, the model has a good center domain prediction with equal prediction variance in all directions. The prediction variances augment from the center of the domain to its limits.

However, since the experiments realized are numerical simulations, which do not present random errors, it is not possible to repeat several experiments

at the center point so that the orthogonal property is satisfied. Consequently, the study will present only the rotatable property (CCRD).

To study the sensitivity of the performance parameters, one needs to choose the model factors. In this study, we are going to study the effects of engine speed (RPM), fuel-air equivalence ratio (ϕ), start of combustion (θ_s), compression ratio (r_c), and intake pressure (P_{int}) on SACI engines.

The performance parameters to be analyzed are: indicated thermal efficiency (η_{th}), indicated mean effective pressure (IMEP), NOx molecular concentration (NOx), mean temperature ($\overline{T}_{avg} = \frac{1}{T}\int_T T_{avg}dt$, where $T_{avg} = x_b T_b + x_u T_u$), and auto-ignition timing (AIT). For each performance parameter, the influence of all factors and their linear relations are studied.

Furthermore, the distance between the center point and the star points, α, is calculated by $\alpha = n_F^{1/4}$, where n_F is the number of factorial points in the DoE. Hence, for a CCD with 5 factors $\alpha = 2.378$.

The calculus were performed using the *Statistica* software (version 12). Finally, the most influential parameters are analyzed. Table 4.1 defines the factors (X) and performance parameters' (Y) symbols.

Table 4.1: Factors and performance parameters in the CCRD

Factors (X)			**Performance Parameters (Y)**		
Symbol	**Variable**	**Unit**	**Symbol**	**Variable**	**Unit**
X_1	RPM	rpm	Y_1	η_{th}	-
X_2	ϕ	-	Y_2	IMEP	*bar*
X_3	θ_s	CAD	Y_3	NOx	*ppm*
X_4	r_c	-	Y_4	$\overline{T}_{avg}$	*K*
X_5	P_{int}	bar	Y_5	AIT	CAD

Now that we know the DoE's properties desired and the number of factors involved, we can calculate the total number of simulations. These calculations are shown in Table 4.2.

Table 4.2: CCD number of experiments with 5 factors ($k = 5$)

Type	**Nb. Simulations**
Factorial points (2^k)	32
Star points ($2k$)	10
Center points (n_c)	1
Total	**43**

The chosen values for the distance between the central and the factorial points (and consequently for α) are displayed in Table 4.3.

Table 4.3: ROCCD factor values for 5 factors

	-α (-2.378)	**-1**	**0**	**+1**	**+α (+2.378)**
Engine speed (rpm)	1,000	2,160	3,000	3,840	5,000
ϕ	0.30	0.50	0.65	0.80	1.00
θ_s (^{o}aTDC)	-40	-28	-20	-12	0
r_c	10.0	12.9	15.0	17.1	20.0
P_{int} (bar)	1.00	1.87	2.50	3.13	4.00

Table 4.4 shows the factor's value for each test.

The DoE response with multiple regression's analysis in a second-order polynomial fitted model is expressed in the Equation 4-1.

$$Y = \beta_0 + \sum \beta_i X_i + \sum \beta_{ii} X_i^2 + \sum \beta_{ij} X_i \cdot X_j \tag{4-1}$$

where Y is the predicted response, β_0 is the intercept coefficient, β_i is the linear coefficient, β_{ii} is the quadratic coefficient, and β_{ij} is the interaction coefficient. With the regressions coefficient, it is possible to study the impact of the factors on the response.

Finally, we will present the Pareto Chart, the observed values, the predicted values, and their residuals, for every performance parameter.

The *Pareto Chart* highlights the most important among the large set of factors. It will be useful to prioritize the univariate analysis afterward. The effects of the investigated factors are divided into linear, quadratic, and linear x linear two-factor interactions, with all effects listed in their order of significance. Furthermore, the red line indicates if the factor has a statistically important effect on the respective response. A low p-value, that is, $p < 0.05$, means that the factor has 5 % significant level. We define that a factor is significant if it has more than this 5 %.

The *Observed vs. Predicted Values* and the *Observed vs. Residual Values* diagrams illustrate the quality of the CCRD model. As explained before, this model takes the linear and quadratic's factor effects and linear x linear two-factor interactions into account.

4.2 Engine parameters

It is noteworthy that the only changes made in the simulator were the factors. The basic engine geometry, valves timing, and combustion parameters remain the same for all tests.

The idea was to generate in the simulations data for car engines types. So,

Table 4.4: CCRD Tests

Tests	RPM	ϕ	θ_0	r_c	P_{int}
01	-1	-1	-1	-1	-1
02	-1	-1	-1	-1	$+1$
03	-1	-1	-1	$+1$	-1
04	-1	-1	-1	$+1$	$+1$
05	-1	-1	$+1$	-1	-1
06	-1	-1	$+1$	-1	$+1$
07	-1	-1	$+1$	$+1$	-1
08	-1	-1	$+1$	$+1$	$+1$
09	-1	$+1$	-1	-1	-1
10	-1	$+1$	-1	-1	$+1$
11	-1	$+1$	-1	$+1$	-1
12	-1	$+1$	-1	$+1$	$+1$
13	-1	$+1$	$+1$	-1	-1
14	-1	$+1$	$+1$	-1	$+1$
15	-1	$+1$	$+1$	$+1$	-1
16	-1	$+1$	$+1$	$+1$	$+1$
17	$+1$	-1	-1	-1	-1
18	$+1$	-1	-1	-1	$+1$
19	$+1$	-1	-1	$+1$	-1
20	$+1$	-1	-1	$+1$	$+1$
21	$+1$	-1	$+1$	-1	-1
22	$+1$	-1	$+1$	-1	$+1$
23	$+1$	-1	$+1$	$+1$	-1
24	$+1$	-1	$+1$	$+1$	$+1$
25	$+1$	$+1$	-1	-1	-1
26	$+1$	$+1$	-1	-1	$+1$
27	$+1$	$+1$	-1	$+1$	-1
28	$+1$	$+1$	-1	$+1$	$+1$
29	$+1$	$+1$	$+1$	-1	-1
30	$+1$	$+1$	$+1$	-1	$+1$
31	$+1$	$+1$	$+1$	$+1$	-1
32	$+1$	$+1$	$+1$	$+1$	$+1$
33	$-\alpha$	0	0	0	0
34	$+\alpha$	0	0	0	0
35	0	$-\alpha$	0	0	0
36	0	$+\alpha$	0	0	0
37	0	0	$-\alpha$	0	0
38	0	0	$+\alpha$	0	0
39	0	0	0	$-\alpha$	0
40	0	0	0	$+\alpha$	0
41	0	0	0	0	$-\alpha$
42	0	0	0	0	$+\alpha$
43	0	0	0	0	0

the engine geometry adopted was a four-cylinder 1.8 L. The complete engine specification is presented in Table 4.5.

Table 4.5: Engine Specification for the CCRD tests

Geometric parameters	
Number of cylinders	4
Bore (mm)	83
Stroke (mm)	81.4
Half-stroke to Rod Ratio	0.271
Total Displacement Volume (cm^3)	1,761
Compression Ratio, r_c	**Variable**
Valves timing	
IVO	0ºaTDC
IVC	45ºaBDC
EVO	35ºbTDC
EVC	0ºaTDC
Operating point	
Engine speed (rpm)	**Variable**
Fuel type	Natural gas
Equivalence Ratio, ϕ	**Variable**
$\boldsymbol{P_{int}}$ (bar)	**Variable**
T_{int} (K)	380
T_{exh} (K)	480
Wiebe parameters	
a_W	6.9078
$\boldsymbol{\theta_s}$	**Variable**
$\theta_{d,SI}$	46º
$m_{W,SI}$	3.20
$\theta_{d,HCCI}$	11º
$m_{W,HCCI}$	5.00

To better represent the combustion phase, one needs to set the combustion parameters correctly. It is possible to calculate this parameters with a pressure versus crank angle graph and certain geometry parameters. For this, we must obtain the gross heat release from an experiment in-cylinder pressure data and transform it into the mass fraction burned (HEYWOOD, 1988). The heat release calculation as a function of the heat capacity ratio and the cylinder volume is calculated as showed in Equation 4-2.

$$\frac{dQ_{ch}}{d\theta} = \frac{\gamma}{\gamma - 1} P \frac{dV}{d\theta} + \frac{1}{\gamma - 1} V \frac{dP}{d\theta} \ [kJ/CAD] \tag{4-2}$$

With the gross heat release rate, we can get the mass fraction burned by the following equation:

$$x_b(\theta) = \frac{Q_{ch}(\theta) - Q_{ch}^{min}}{Q_{ch}^{max} - Q_{ch}^{min}} \tag{4-3}$$

With the experimental mass fraction burned calculated above, it is possible to discover the Wiebe parameters that best fit into the Wiebe function by least squares (FAGUNDEZ et al., 2017).

5
Results and Discussion

In this chapter, we will study the influence of multiple factors in the SACI engine performance. It will be divided into four parts. In the first one the engine simulator will be validated for SI and HCCI engines. In the second one (Case Study) we will analyze the central point case in the CCRD. The third one is the CCRD study itself, discovering the most significant factors for each performance parameter. The fourth one is the UA of the main factors for the responses.

5.1
Model Validation

Once the model is ready, one needs to validate it. Only then we can say if the solution represents reality. For that, we chose to validate the model in three different engine specifications, from three authors.

In this validation, we tested the SI and HCCI internal combustion engines: the two techniques that together form the SACI engine.

5.1.1
SI engines

The first engine for comparison comes from an SI engine in an experiment made by Chala et al. (CHALA; AZIZ; HAGOS, 2018). It is a four-cylinder slightly oversquare engine with a 9.25 compression ratio. It has the size of a car engine, with a total displacement volume of 1.761 L, natural gas as fuel, and a stoichiometric fuel-air ratio. The complete engine geometric parameters, valves timing, and operating point are illustrated in Table 5.1.

In order to obtain the combustion parameters, we perform the procedure described in Chapter 4. Setting the efficiency factor to 6.9078, we find the parameter values in Table 5.1.

The fitted Wiebe function can, then, be plotted versus the crank angle with the experimental mass fraction burned in Figure 5.1. The fitted function has an R^2 of 99.96%, meaning it is a great fit.

Now, we can put the combustion parameters as initial data in the Matlab engine simulator and run the model with Engine Specification 1. Figure 5.2 shows the calculated pressure and the experimental in-cylinder pressure. As seen in the graph, the model has a good representation of this type of engine with a R^2 of 99.79%.

Table 5.1: SI Engine Specification 1 (CHALA; AZIZ; HAGOS, 2018)

Geometric parameters	
Number of cylinders	4 (In line)
Bore (mm)	83
Stroke (mm)	81.4
Half-stroke to Rod Ratio	0.271
Total Displacement Volume (cm^3)	1,761
Compression Ratio	9.25
Valves timing	
IVO	32ºbTDC
IVC	64ºaBDC
EVO	59ºbTDC
EVC	17ºaBDC
Operating point 1	
Engine speed (rpm)	3000
Fuel type	Natural gas
Equivalence Ratio (ϕ)	1.00

Table 5.2: Wiebe parameters: engine specification 1

Wiebe parameters	
a_W	6.9078
θ_s	58ºbTDC
θ_d	87º
m_W	3.20

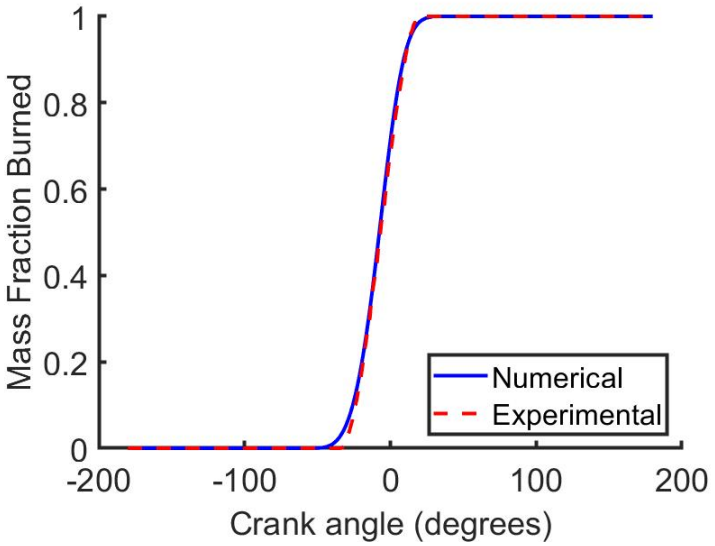

Figure 5.1: Wiebe function optimization, $R^2 = 99.96\%$ (CHALA; AZIZ; HAGOS, 2018).

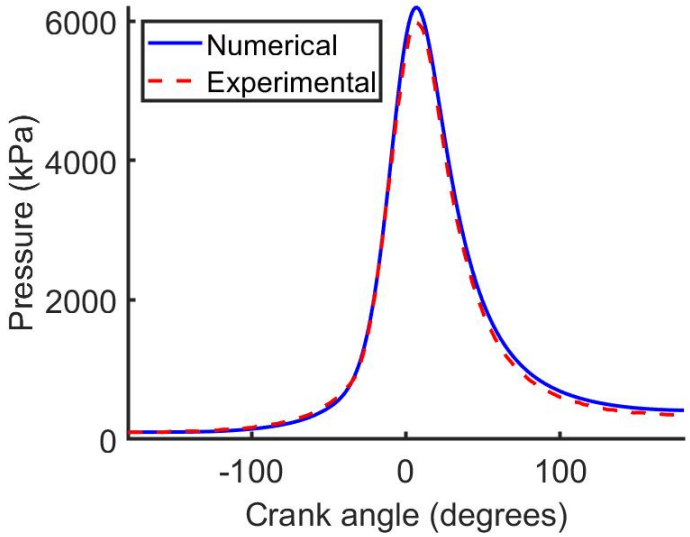

Figure 5.2: Pressure experimental comparison, $R^2 = 99.79\%$ (CHALA; AZIZ; HAGOS, 2018).

One can compare some performance parameters such as maximum pressure, brake mean effective pressure, thermal efficiency, power, and NOx concentration between the numerical simulation and the experimental result. Table 5.3 shows these parameters values and their relative errors. We can note that the maximum pressure has an error of only three percent. The other parameters were calculated in the model as indicated and were transformed into brake with the Chen-Flynn friction correlation model, where the FMEP (bar) is calculated by $FMEP = A + B\ P_{max} + C\ S_f + D\ S_f^2$. In this model, $S_f = \frac{wS}{2}$ and the constants used were proposed by Pipitone (PIPITONE, 2009) for a 2.0 L 4 cylinders SI engine.

One can see that numerical model represented well the experiment, with relative errors less than 1% for IMEP and thermal efficiency and a 4 and 9 % of increase in the Power and NOx concentration at the exhaust manifold.

Table 5.3: Engine comparison 1

Parameter	**Experiment**	**Model**	ϵ
P_{max} (MPa)	5.97	6.20	+3.62 %
BMEP (bar)	7.80	7.78	-0.003 %
η_{th}	28.42 %	28.40 %	-0.0007 %
Power (HP)	52.02	54.47	+4.50 %
NO_X (g/kWh)	4.71	5.19	+9.25 %

So, it is possible to say that the model made a good prediction for this particular SI case, specially in IMEP and thermal efficiency.

The second engine is also a SI engine, from Sremec experiments (SREMEC et al., 2017). It is a single-cylinder oversquare engine with a variable compression ratio (12 to 16). Bigger and much more oversquare than the first one, with a displacement volume of 0.667 L. It works with natural gas and with leaner mixtures ($\phi = 0.71$ to 0.83), Table 5.4.

It was not possible to find the valves timing for this particular engine, so we had to assume all the valves' intake and exhaust timing and their geometry. However, this work shows the engine performance parameters' tendency and sensibility regarding compression ratio and fuel-air equivalence ratio.

Table 5.4: SI Engine Specification 2 (SREMEC et al., 2017)

Geometric parameters	
Number of cylinders	1
Bore (mm)	100
Stroke (mm)	85
Half-stroke to Rod Ratio	0.335
Total Displacement Volume (cm^3)	667
Compression Ratio	12 and 16
Valves timing	
IVO	0^obTDC
IVC	45^oaBDC
EVO	35^obBDC
EVC	0^oaTDC
Operating point 2	
Engine speed (rpm)	2000
Fuel type	Natural gas
Equivalence Ratio (ϕ)	0.83 and 0.71

The two compression ratio possibilities alongside the two fuel-air equivalence ratio points can be divided into four operating points, as shown in Table 5.5. For each of them, the combustion parameters were discovered with the same approach seen in methodology.

Table 5.5: Operating points in SI Engine Specification 2

Operating point	Parameters	Combustion
2.1	$r_c = 12$ and $\phi = 0.83$	$\theta_s = 30^o$bTDC and $\theta_d = 46^o$
2.2	$r_c = 16$ and $\phi = 0.83$	$\theta_s = 20^o$bTDC and $\theta_d = 39^o$
2.3	$r_c = 12$ and $\phi = 0.71$	$\theta_s = 40^o$bTDC and $\theta_d = 70^o$
2.4	$r_c = 16$ and $\phi = 0.71$	$\theta_s = 20^o$bTDC and $\theta_d = 42^o$

The start of heat release and the combustion duration is displayed in the same table. It is possible to see that the combustion duration in SI engines fueled with natural gas is 45-50 crank angle degrees. Furthermore, the spark timing happens around -20 and -30 $°aTDC$, which makes the maximum of heat release close to the TDC.

Table 5.6 exposes the difference between experimental and numerical data from some engine performance parameters (IMEP, thermal efficiency and NOx emissions).

Table 5.6: SI 2 Operating points comparison

	Parameter	**Experimental**	**Numerical**	ϵ
2.1	IMEP (bar)	7.3	10.0	+27.0 %
	η_{th}	35.6 %	39.7 %	+10.3 %
	NO_X (g/kWh)	16.9	30.8	+45.1 %
2.2	IMEP (bar)	7.5	10.9	+31.2 %
	η_{th}	38.1 %	43.2 %	+11.8 %
	NO_X (g/kWh)	25.5	26.5	+3.8 %
2.3	IMEP (bar)	6.0	9.0	+33.3 %
	η_{th}	34.4 %	40.9 %	+15.9 %
	NO_X (g/kWh)	2.2	6.2	+64.5 %
2.4	IMEP (bar)	6.3	9.7	+35.1 %
	η_{th}	36.9 %	44.4 %	+16.9 %
	NO_X (g/kWh)	3.0	6.0	+50.0 %

These results show that the numerical IMEP follows the experimental tendency with the variation of the compression ratio and the fuel-air equivalence ratio. The thermal efficiency presents the experimental tendency for the compression ratio but not for the equivalence ratio. Moreover, the error is significant. If we look at the IMEP, for instance, the mean relative error from all four operating points is +31.6 %. It means that the pressure and the mass inside the cylinder are overestimated. The thermal efficiencies are also overestimated, with a mean relative error of +13.7 %.

Thermal efficiency is highly dependent on pressure, so it makes sense that if one of them is overestimated, the other is as well. Moreover, NOx emissions tend to achieve the concentration magnitude, but it is not precise. This inaccuracy could be explained by the fact that NOx emissions in lean and very lean mixtures are low. So, the program realizes the order of magnitude, but it is not able to be accurate.

These behaviors could be explained by the lack of information regarding the valve's timing, geometry, and intake and exhaust pressures and tem-

peratures. These parameters can change significantly the pressure curve and consequently the performance parameters.

5.1.2 HCCI engines

Finally, for the HCCI validation, the engine studied is bigger (probably with a truck application), and slightly undersquare. A single-cylinder has a displacement volume of 1.132 L. The compression ratio is 18.8. The engine speed is slower, with 800 rpm, and the air-fuel blend much leaner. It is noteworthy that the engine has a supercharger since the intake pressure is 1.6 bar, Table 5.7. Furthermore, only the IVO crank angle degree is displayed. We have to assume, again, other valves times.

Table 5.7: HCCI Engine Specification (ZHAO, 2007)

Geometric parameters	
Number of cylinders	1
Bore (mm)	112
Stroke (mm)	115
Half-stroke to Rod Ratio	0.23
Total Displacement Volume (cm^3)	1,132
Compression Ratio	18.8
Valves timing	
IVO	0^oaTDC
IVC	48^oaBDC
EVO	35^obTDC
EVC	0^oaTDC
Operating point	
Engine speed (rpm)	800
Fuel type	Natural gas
Equivalence Ratio (ϕ)	0.35 - 0.45
P_{int} (bar)	1.6
T_{int} (K)	380
T_{exh} (K)	480

The experimental pressure versus the crank angle is shown in Figure 5.3. We can see the difference in pressure caused by the difference in fuel-air equivalence ratios.

With these three curves, we can obtain the Wiebe function parameters. They are shown in Table 5.8. Interestingly, the combustion duration of the three cases is similar. It displays that the combustion duration in HCCI engines is three to four times faster than combustion in SI engines.

Table 5.8: Wiebe parameters: HCCI engine specification

ϕ	θ_s	θ_d	m_W
0.35	5ºbTDC	12º	5.00
0.40	5ºbTDC	11º	5.00
0.45	6ºbTDC	10º	5.00

As soon as the combustion parameters are known. It is possible to simulate the HCCI engine in the Engine Specification from Table 5.7. The numerical results are also displayed in Figure 5.3.

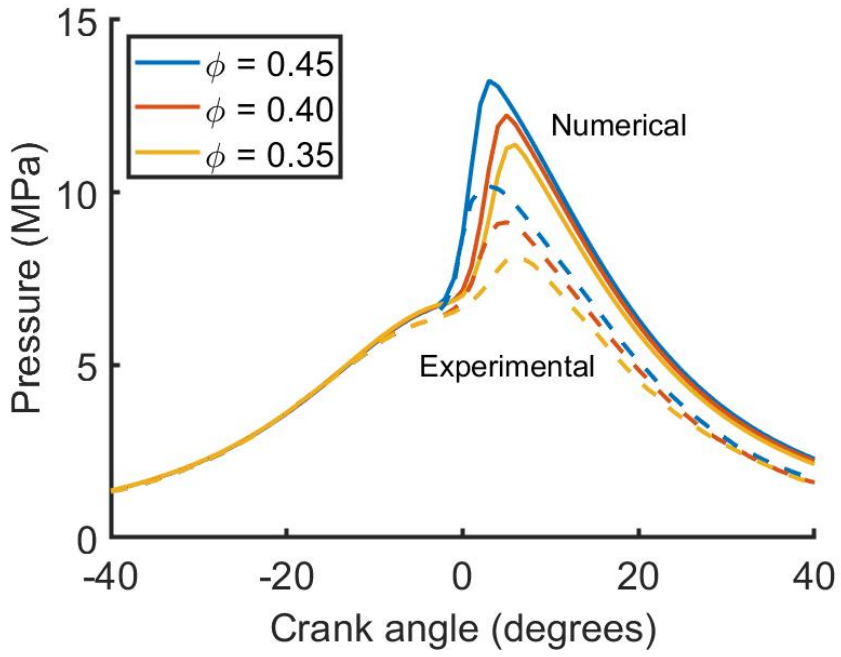

Figure 5.3: Experimental and numerical in-cylinder pressure at different fuel-air equivalence ratios.

The compression phase pressure is similar between the experimental and numerical results. The numerical simulation gets the information of the difference in fuel-air equivalence ratio combustions. However, the pressure rises too much when compared to the experimental results. A probable cause is the heat transfer model, which was made to describe the in-cylinder heat transfer for lower pressures and higher temperatures. Thus, the heat transfer model may not be appropriate to model precisely the HCCI rapid combustion and high in-cylinder pressures.

If we look at the relative errors in Table 5.9, we can notice that the leaner the fuel, the higher the relative error is. So, the model is slightly more accurate for richer air-fuel mixtures, even though it predicts the general behavior of the engine gas.

Table 5.9: Maximum pressure (MPa) at different fuel-air equivalence ratios

ϕ	**Experiment**	**Model**	ϵ
0.35	8.1	11.4	+28.9 %
0.40	9.1	12.2	+25.4 %
0.45	10.2	13.2	+22.7 %

5.2 Baseline Case Study

To understand the SACI mechanism in the ICE's Matlab simulator and study the main responses of this new type of multi-mode combustion, we will study the simulator result for the CCRD center point case. In this configuration, the engine's geometry (r_c), operating point (Engine speed, ϕ, and P_{int}), and combustion parameter (θ_s) are presented in the 43^{rd} test at Table 4.4.

Figure 5.4 illustrates the SACI mass fraction burned (the combustion progress) behavior in function of the crank angle. It is possible to note that the SACI combustion starts like an SI combustion, but when the precursor mass reaches the critical mass to self-ignite, the combustion speed rises, and the unburned gases burn in an HCCI form.

Both validation experiments (SI and HCCI) helped to define the combustion parameters for the SACI combustion with methane as fuel. The combustion duration of the experiments seen in Chapter 3 for SI and HCCI for methane was in the order of 46 CAD and 11 CAD, respectively. That's why the combustion parameters for all cases studied are modeled in this way.

Moreover, we see that the mixture reaches the auto-ignition state right before the TDC. This limit is obtained in $\theta = -2°aTDC$, as suggested by the simulator. In HCCI and SACI engines, the auto-ignition timing is normally considered to happen at the TDC, so this case study is an operating point that is close to the ideal auto-ignition timing (AIT).

Figure 5.5 explains the pressure curve in the presence of the valves timing when compared to the motored pressure and Figure 5.6 focus on the difference between the motored and in-cylinder pressures at the combustion phase.

We can see that in the combustion phase, near the start of combustion, the in-cylinder pressure is lower than the motored pressure. This happens because the motored pressure does not take the gas heat transfer into account. The SACI numerical simulation, however, considers it at every simulation step.

The mass burns almost simultaneously after $-2°aTDC$, exactly when the pressure at the cylinder is at a high value due to compression, resulting

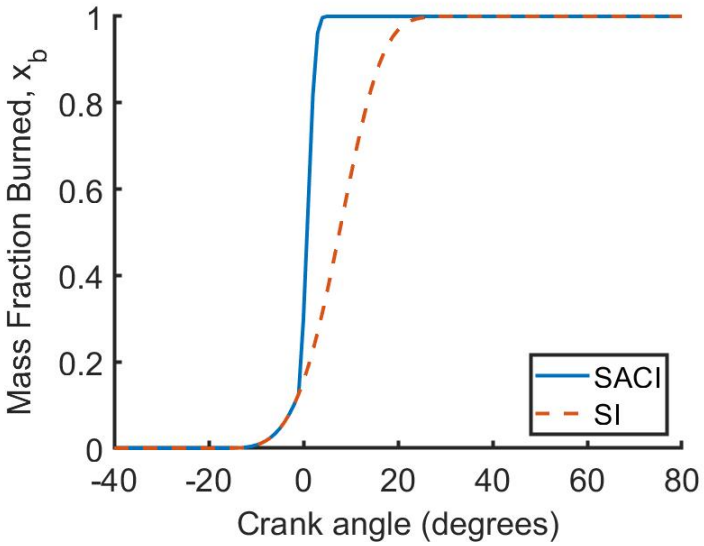

Figure 5.4: Mass fraction burned versus the crank angle in the CCRD central point study for SACI engines.

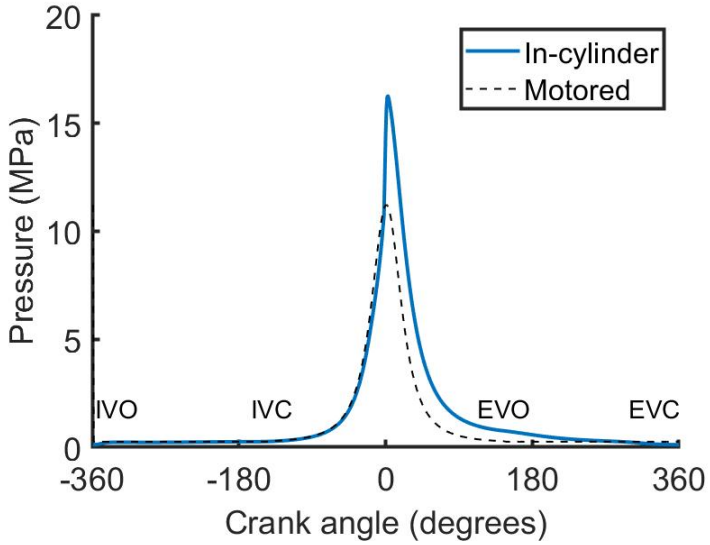

Figure 5.5: Pressure versus the crank angle in the CCRD central point study for SACI engines.

in high maximum in-cylinder pressure. High pressure after the TDC is good for the engine's thermal and overall efficiency. However, high pressure demands robust material, which can be expensive. That's why the industry is constantly searching for the optimization of thermal efficiency, pollutant emissions, and engine materials.

We can also plot the gases' temperatures in the cylinder. Figure 5.7 shows the burned, unburned and average temperatures versus the crank angle. We see that the temperature at the intake is low near the ambient temperature. When the intake valve closes, the unburned gases temperature rises quickly

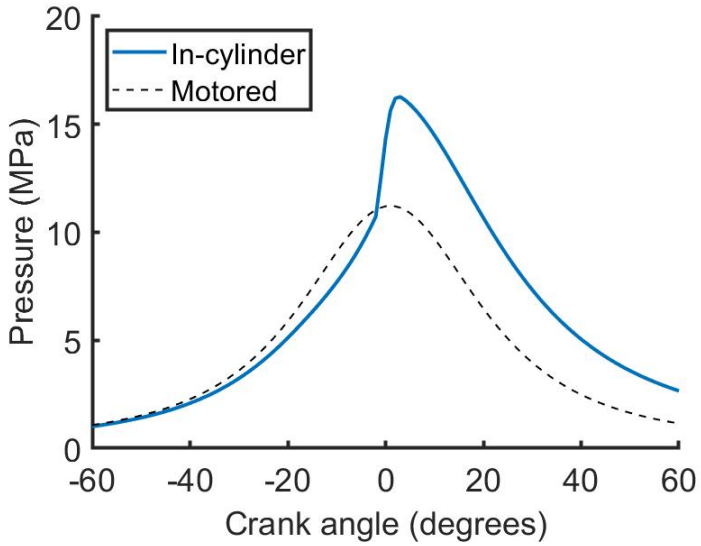

Figure 5.6: Combustion phase zoom of the pressure versus the crank angle in the CCRD central point study for SACI engines.

until it reaches the maximum near the end of the combustion. Then, the heat transfer makes the burned gases' temperature diminishes. Finally, the exhaust valve opening lets the burned gas temperature decrease even more.

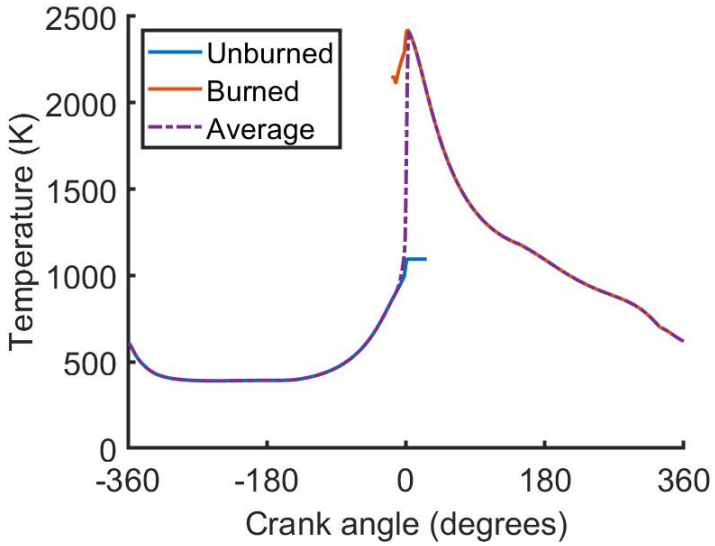

Figure 5.7: Temperature versus the crank angle in the CCRD central point study for SACI engines.

HCCI and SACI combustion modes are low-temperature combustion methods. In this kind of engine, due to the leaner air-fuel mixture, the temperature inside the cylinder is not as high as in SI engines. Comparing this curve temperature with the temperature of Appendix A, we see that even though the maximum in-cylinder pressure is more than three times higher in

SACI engines, the maximum gas temperature is lower in SACI. The mean average temperature, in this case, was 838.2 K.

We can also analyze the classic pressure versus volume diagram. Figure 5.8 shows the PxV diagram for the SACI combustion. The pressure's high increase in a tiny change in volume highlights the influence of the AI. Figure 5.9 illustrates the same PxV diagram but in logarithmic axes. With this scale, we can notice the polytropic compression and calculate the polytropic coefficient of compression. As we can see, this coefficient is 1.36, which corresponds exactly to a value between 1.33 and 1.38, expected for natural gas - air mixtures (QUINTANA; CASTAñO-MESA; BEDOYA, 2017).

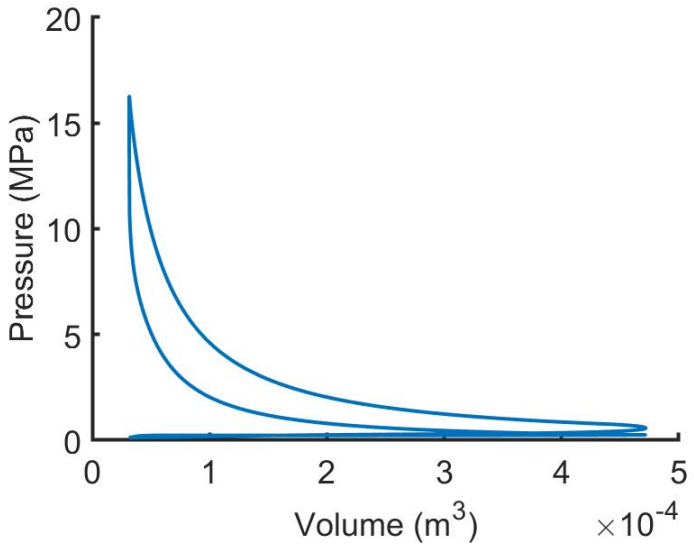

Figure 5.8: Pressure versus volume diagram in the CCRD central point study for SACI engines.

The work and heat plot, in Figure 5.10, illustrates that it is at the power stroke where the gross work is done. Moreover, the gross heat loss happens after the TDC, when the gas average temperature is high. At the end of the cycle, one cylinder produces approximately 0.7 kJ of work and loses 0.3 kJ as heat transfer to the walls and coolant.

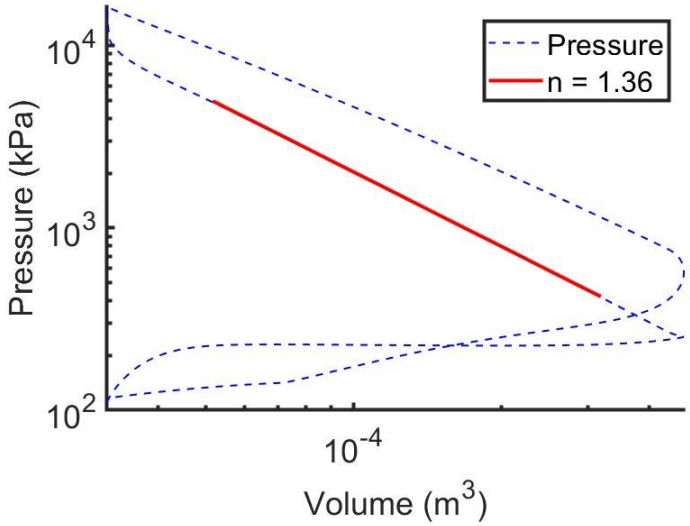

Figure 5.9: Simulated in-cylinder log-log pressure versus volume diagram and its polytropic coefficient at compression.

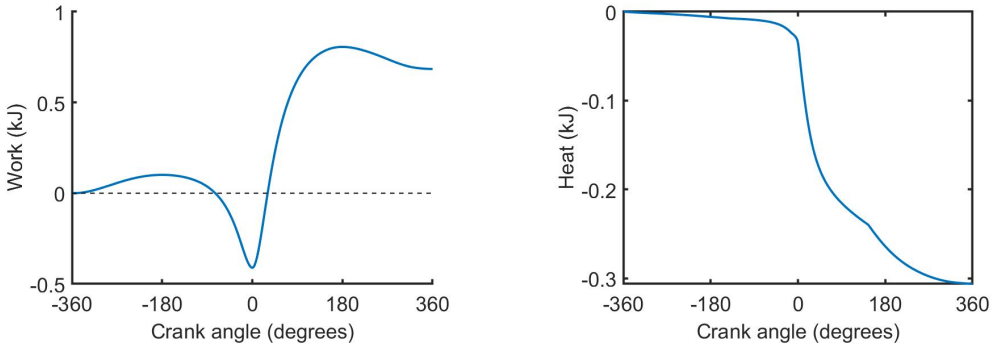

(a) Work. (b) Heat.

Figure 5.10: Work and heat versus crank angle.

We can observe the in-cylinder mass as a function of the crank angle in Figure 5.11. It augments at the intake stroke until it reaches 1 g. Then, it lightly reduces because of the blowby, having 1.27 % less mass at the EVO when compared to the IVC, which corresponds to the blowby mass seen in Chapter 3.

Finally, the major species' molecular fraction during the combustion phase is represented in Figure 5.12. Since the engine has a fuel-air equivalence ratio of 0.65, we expect to find oxygen at the end of combustion. And that's the case in the graph.

Instead of the presence of CO, as we have seen in Figure 3.8b, the SACI combustion in this particular case has a higher molecular fraction of NO due to its lean air-fuel mixture. Furthermore, the chemical species'

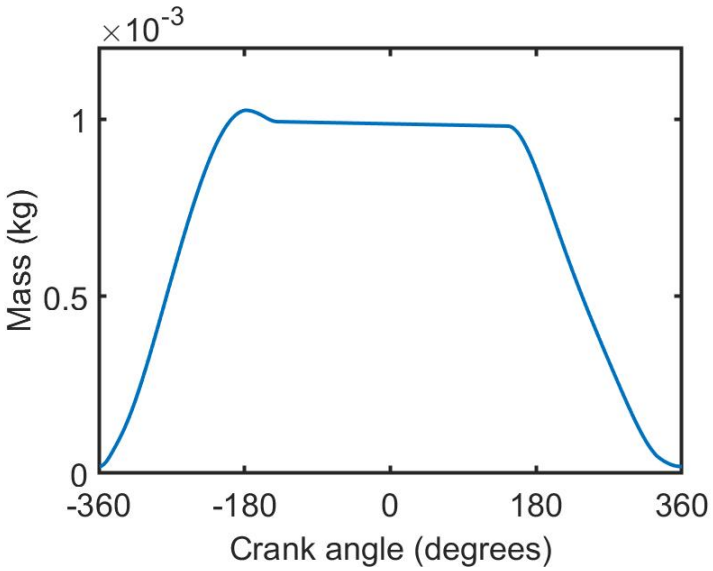

Figure 5.11: Mass in SACI engines.

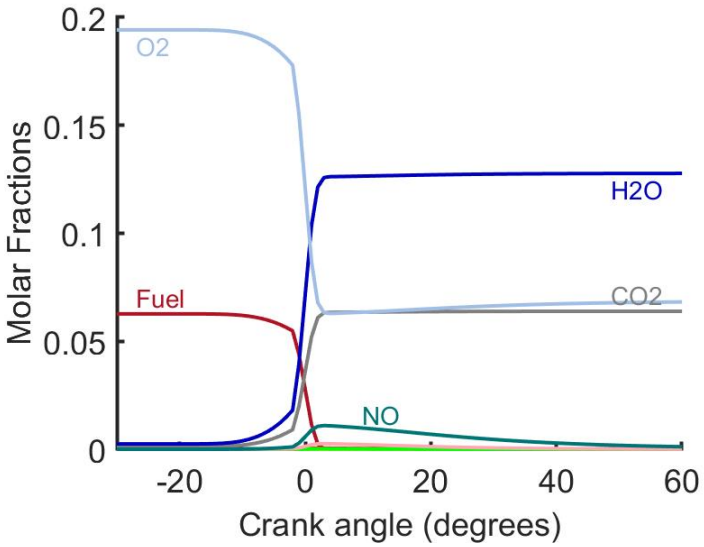

Figure 5.12: Molar fractions in SACI engines.

production/destruction rate change is considered. It happens at the AIT.

Figure5.13 shows the combustion process in the minor species molecular fraction as a function of the crank angle with the fuel as a reference for the combustion timing. The highest minor species are: the radical OH, followed by CO, H_2, and the radical O. As it can be seen, the HCCI combustion affects the minor species molar fractions significantly, as it does on the major species. It is relevant to notice that the minor species with the highest molar fraction is the radical OH in both SI and SACI cases.

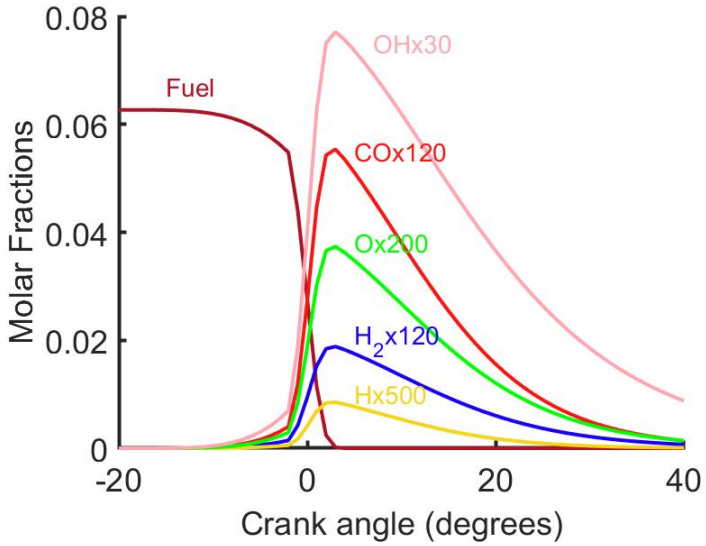

Figure 5.13: Minor species molar fractions in SACI engines.

5.3 CCRD parameter study

In this section, we will study the CCRD model and analyze the five responses for each test performed in Table 5.10.

5.3.1 Thermal Efficiency

The first performance parameter studied was the indicated thermal efficiency. The thermal efficiency simulation values were fitted to the quadratic equation (Equation 4-1), and the following second-order polynomial regression equation was obtained:

$$\begin{aligned} Y_1 = {} & 0.384771 - 0.031600X_1 - 0.009523X_1^2 - 0.015766X_2 - 0.008512X_2^2 \\ & + 0.004119X_3 - 0.004072X_3^2 - 0.000490X_4 + 0.000702X_4^4 - 0.028987X_5 \\ & - 0.001497X_5^2 - 0.009177X_1X_2 - 0.003292X_1X_3 - 0.000977X_1X_4 \\ & - 0.020110X_1X_5 - 0.002685X_2X_3 + 0.000966X_2X_4 - 0.005871X_2X_5 \\ & - 0.000307X_3X_4 - 0.003698X_3X_5 + 0.003719X_4X_5 \ [-] \end{aligned} \quad (5\text{-}1)$$

Figure 5.14 shows the Pareto Chart for this response: it lists the factors from most to least significant. It is possible to notice that three factors are notable to a SACI engine's thermal efficiency: engine speed (X_1), intake pressure (X_5), and fuel-air equivalence ratio (X_2). The engine speed times the intake pressure ($X_1 \cdot X_5$) is also a significant parameter, more considerable than the linear fuel-air equivalence ratio factor.

Table 5.10: CCRD Results

Tests	$\eta_{th}(\%)$	IMEP (bar)	NOx (ppm)	$\overline{T}_{avg}(K)$	AIT $(°aTDC)$
01	41.76	9.93	26	731.2	-2
02	39.39	15.83	28	756.1	-6
03	40.84	9.63	51	724.5	-7
04	38.91	15.45	51	749.7	-11
05	45.51	10.82	8	722.8	21
06	39.47	15.87	12	744.2	4
07	42.37	9.99	30	713.9	0
08	40.44	16.06	48	734.9	-9
09	38.40	14.21	6,509	884.6	-3
10	36.52	22.83	7,157	915.0	-7
11	38.43	14.09	8,425	864.8	-7
12	37.17	22.98	9,217	895.6	-11
13	40.15	14.87	3,517	873.9	16
14	36.75	22.98	4,431	899.8	5
15	39.77	14.59	6,105	857.5	2
16	38.98	24.10	8,499	874.0	-8
17	39.04	9.04	23	782.1	-1
18	31.78	11.37	7	814.1	-6
19	38.75	8.98	45	770.9	-6
20	32.19	11.61	17	806.4	-11
21	42.36	9.78	6	774.8	25
22	30.95	11.06	3	801.6	3
23	38.74	8.97	17	759.5	2
24	33.87	12.23	17	789.2	-9
25	35.92	12.94	5,067	956.0	-2
26	24.46	13.66	1,011	1,082.8	8
27	36.00	12.93	6,277	937.8	-7
28	22.85	13.18	1,359	1,105.6	9
29	36.61	13.19	2,440	942.9	17
30	22.70	12.69	512	1,067.7	-
31	36.29	13.03	3,487	921.8	4
32	20.95	12.11	691	1,083.3	-
33	38.39	15.63	1,812	746.5	-4
34	27.69	9.20	40	936.1	13
35	32.33	6.22	0	649.7	-2
36	34.90	21.04	6,905	1,021.3	-2
37	35.21	14.25	1,339	878.0	-14
38	37.03	14.98	293	838.4	4
39	38.17	15.73	397	863.6	9
40	39.48	15.85	1,464	823.5	-9
41	42.20	6.66	450	808.7	11
42	32.96	20.38	566	889.3	-9
43	38.41	15.55	689	838.2	-2

Poompipatpong, Choi, and Tangsiriworakul show that higher engine speeds have a negative effect on thermal efficiency due to the engine's inability to intake a full charge of air (POOMPIPATPONG; CHOI; TANGSIRIWORAKUL, 2014). The predicted model for SACI engines shows a negative linear engine speed regression coefficient, showing the negative influence in performance at high rotations. Furthermore, this SACI engine's thermal efficiency tends to decrease with the increase of intake pressure ($\beta_5 = -0,028987\ bar^{-1}$), which is different from normal SI engines that augment efficiency with the increase in intake pressure (DIMITRIOU et al.,). This can be explained by the fact that high in-cylinder pressures can trigger early auto-ignition, which is harmful to efficiency.

In a SI engine, thermal efficiency has a maximum value at fuel-air equivalence ratios of 0.7-0.8 (HOEKSTRA; BLARIGAN; MULLIGAN, 1996). The predicted model indicates a negative regression coefficient ($\beta_2 = -0.015766$), confirming that the variation impacts as in SI engines.

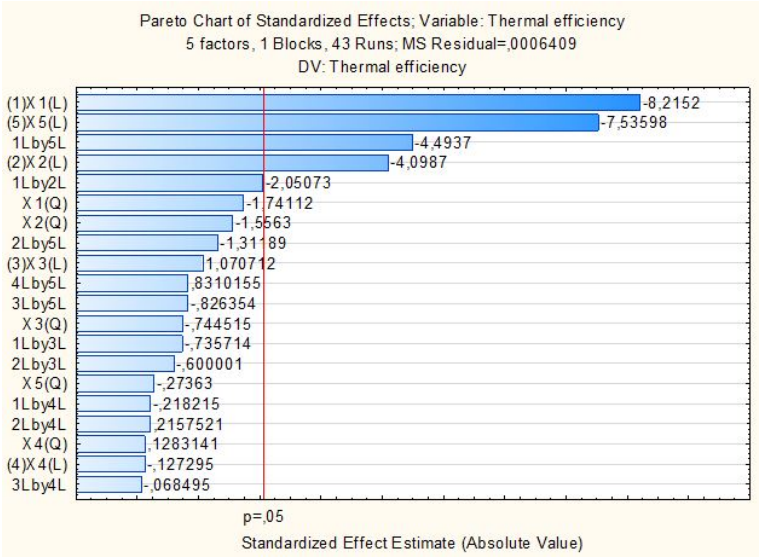

Figure 5.14: Pareto Chart for thermal efficiency in the CCRD.

The CCRD quadratic prediction model is illustrated in Figure 5.15. The left graph shows the observed versus the model's predicted values. The closer the blue points are from $y = x$, the better the model. In this case, thermal efficiency prediction has a R^2 of 89.08 %. The right graph represents the residual observed at each prediction. The residues are also uniformly distributed around the average value of zero, as an expression of the robustness of the model. The highest residual in thermal efficiency was 5%, which agrees with the similarity between the observed and predicted values.

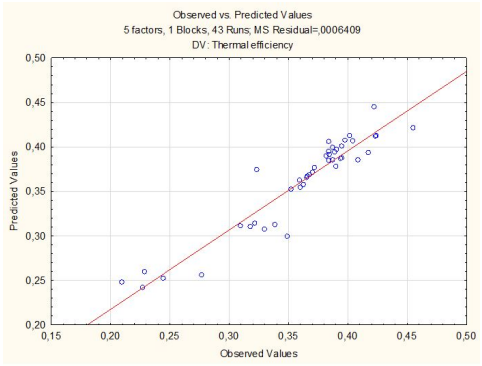

(a) Observed vs. Predicted Values diagram.

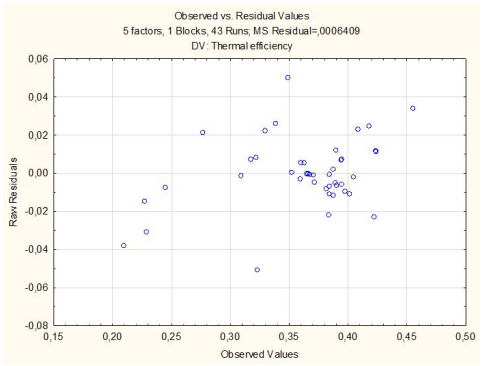

(b) Observed vs. Residual Values diagram.

Figure 5.15: Thermal efficiency observation, prediction and residuals in the CCRD model ($R^2 = 89.08\%$).

5.3.2 IMEP

The IMEP quadratic model is obtained by the following equation:

$$\begin{aligned} Y_2 = {} & 1517.819 - 191.019X_1 - 53.705X_1^2 + 237.821X_2 - 32.253X_2^2 + 12.502X_3 \\ & - 14.856X_3^2 - 2.014X_4 + 5.846X_4^2 + 230.021X_5 - 34.211X_5^2 - 82.446X_1X_2 \\ & - 15.457X_1X_3 - 0.726X_1X_4 - 152.939X_1X_5 - 6.917X_2X_3 + 1.333X_2X_4 \\ & + 7.350X_2X_5 + 2.414X_3X_4 - 10.388X_3X_5 + 12.543X_4X_5 \ [kPa] \quad (5\text{-}2) \end{aligned}$$

The IMEP Pareto Chart, Figure 5.16, indicates the significance of the same three factor but in different orders of importance: fuel-air equivalence ratio (X_2), intake pressure (X_5), and engine speed (X_1). There are also two relevant interactions: engine speed times intake pressure ($X_1 \cdot X_5$) and engine speed times fuel-air equivalence ratio ($X_1 \cdot X_2$).

In this particular case, the two other factors (spark timing (X_3) and compression ratio (X_4)) are less significant than the quadratic form of those three factors.

Analyzing the factors' influence in SI engines, we observe that the higher the fuel-air equivalent ratio is, the higher the IMEP is. The maximum IMEP is achieved at an equivalence ratio of 1.1-1.2 (ROBISON; BREHOB, 1967). Furthermore, IMEP increases with the intake pressure and has a maximum value at intermediate engine speeds, from 2000 to 3000 rpm (HIGASHISONO; TAKEUCHI; HARA, 1982).

The SACI's IMEP quadratic model indicates that it tends to increase with the fuel-air equivalence ratio and with the intake pressure, as happens in

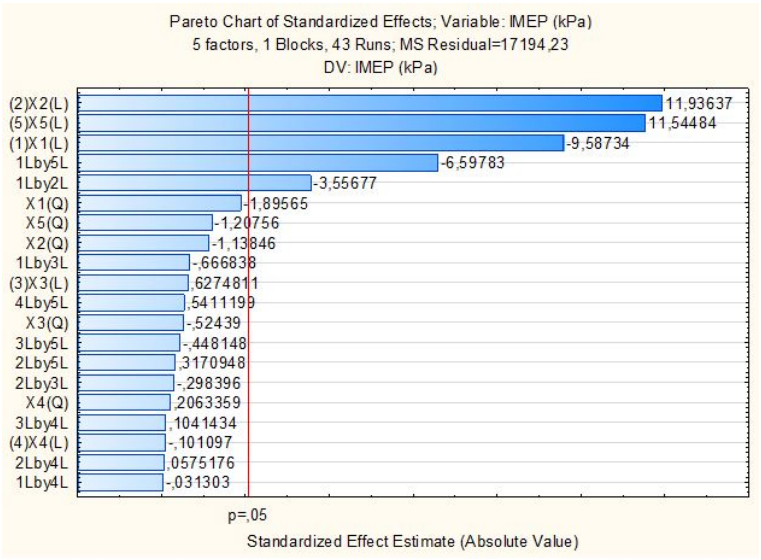

Figure 5.16: Pareto Chart for IMEP in the CCRD.

SI engines. Besides, the engine speed has a negative influence on the IMEP for SACI engines. As previously exposed, this could be explained by the amount of in-cylinder air in the cylinder: at high rotations, there is less in-cylinder mass.

The predicted model for IMEP, Figure 5.17, is better than the one for the thermal efficiency with a R^2 of 95.18%. In the *Observed vs. Predicted Values* graph, one can notice that the red line (least square approximation of the blue points) is close to $y = x$. For the *Observed vs. Residual Values*, the closer the points are from the center of the graph, the better the prediction model is. The IMEP residual values are closer to the center than in the thermal efficiency analysis. We can see it by the R^2 value, proving the quadratic model strength.

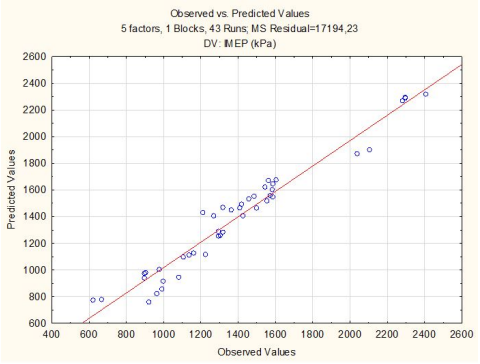

(a) Observed vs. Predicted Values diagram.

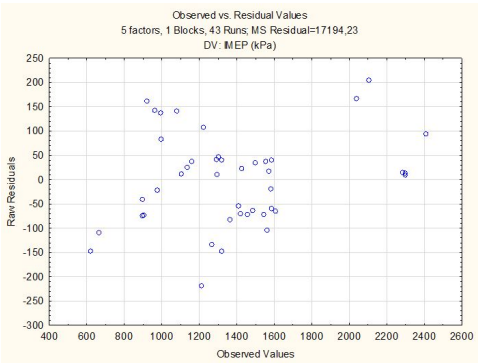

(b) Observed vs. Residual Values diagram.

Figure 5.17: IMEP observation, prediction and residuals in the CCRD model ($R^2 = 95.18\%$).

5.3.3 NOx Emissions

The NOx emissions regression curve is

$$Y_3 = 1722.62 - 862.32X_1 - 1.73X_1^2 + 2094.89X_2 + 444.92X_2^2 - 414.09X_3 - 21.05X_3^2 + 372.11X_4 - 0.83X_4^2 - 200.77X_5 - 75.55X_5^2 - 1028.06X_1X_2 + 68.26X_1X_3 - 246.79X_1X_4 - 578.68X_1X_5 - 476.00X_2X_3 + 414.14X_2X_4 - 279.01X_2X_5 + 73.56X_3X_4 + 193.15X_3X_5 - 3.22X_4X_5 \ [ppm] \quad (5\text{-}3)$$

Figure 5.18 exposes the main factors for SACI NOx emissions. The most important is the fuel-air equivalent ratio (X_2), followed by its interaction with the engine speed ($X_1 \cdot X_2$). The second most significant linear factor, which has two times less influence in NOx formation than the fuel-air ratio, is the engine speed (X_1). Unlike the previous two performance parameters, intake pressure has no great importance for emissions. The sparking time (X_3), however, is the third most significant linear factor. Engine speed together with the intake pressure ($X_1 \cdot X_5$) completes the list of significant two factors relations.

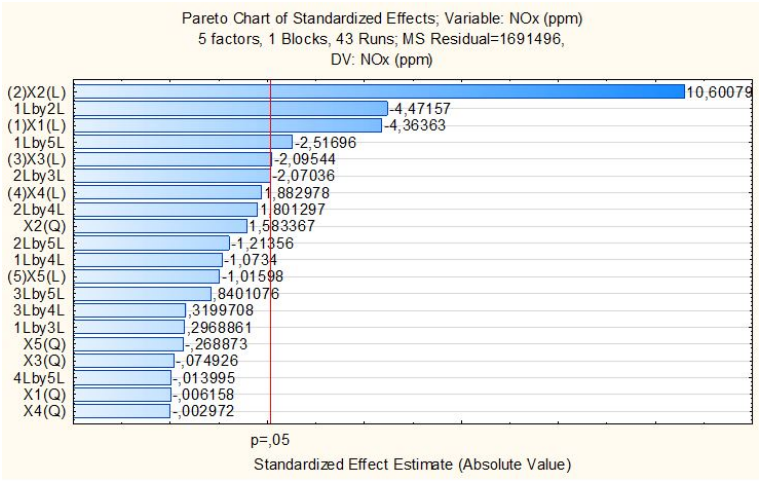

Figure 5.18: Pareto Chart for NOx emissions in the CCRD.

As we have seen in Chapter 3, the SACI simulator is not very precise at predicting low NOx emissions, although it is accurate in its order of magnitude. Figure 5.19 exhibits the quadratic function estimation of the numerical simulations. As it happens in the simulator, the prediction of low NOx emissions is difficult. High NOx emissions estimations have, however, good predictions. The coefficient of determination (R^2) in this case is 89.36%.

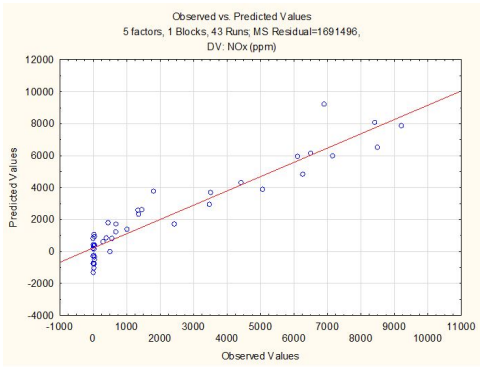

(a) Observed vs. Predicted Values diagram.

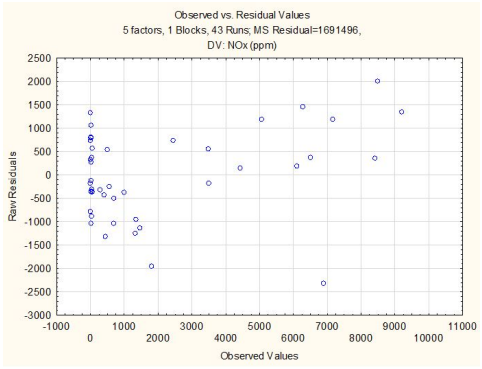

(b) Observed vs. Residual Values diagram.

Figure 5.19: NOx observation, prediction and residuals in the CCRD model ($R^2 = 89.36\%$).

The fuel-air equivalent ratio dictates almost entirely the NOx formation on low-temperature combustion engines like HCCI and SACI. When the fuel-air equivalent ratio is lower than 0.5, the NOx formation in these types of engines goes to the magnitude of 100 ppm, less than 10 % of the NOx emissions of SI engines (KEROS et al., 2009). The NOx quadratic model predicts the positive influence of the equivalence ratio on the NOx formation, with a regression constant of $\beta_2 = +2094.89\ ppm$. On these operating points, the lean combustion does not let the mean in-cylinder temperature rise, so there are less NOx formations.

Also, spark timing is strongly related to NOx formation. The more the spark is advanced in SI engines, the higher will be the NOx concentration at the exhaust (RIBBENS, 2017). The model shows similar behavior in SACI engines with a negative coefficient of -414.09, i.e., delay spark timing will diminish NOx emissions. The increase in in-cylinder pressure by spark advance can be explained by the combustion duration. It leads to combustion near the TDC, which can turn into early auto-ignition and augment even more the combustion chamber's pressure in SACI.

5.3.4
Mean Temperature

The mean in-cylinder temperature quadratic model is the following:

$$Y_4 = 847.4055 + 43.9707X_1 + 0.1592X_1^2 + 89.3770X_2 - 0.8682X_2^2 - 7.1467X_3 + 3.1424X_3^2 - 5.9048X_4 + 0.5626X_4^2 + 25.2387X_5 + 1.5213X_5^2 + 19.1096X_1X_2 - 0.4499X_1X_3 + 2.0367X_1X_4 + 15.8923X_1X_5 - 0.8549X_2X_3 - 0.1300X_2X_4 + 14.6368X_2X_5 - 0.8420X_3X_4 - 1.4368X_3X_5 + 2.3419X_4X_5 \ [K] \quad (5\text{-}4)$$

The mean temperature is influenced by four linear factors and three interactions, as it can be seen in the Pareto Chart of Figure 5.20. The linear factors in order of significance are: fuel-air equivalence ratio (X_2), engine speed (X_1), intake pressure (X_5), and sparking time (X_3). The interactions are: engine speed times equivalence ratio ($X_1 \cdot X_2$), engine speed times intake pressure ($X_1 \cdot X_5$), and equivalence ratio times intake pressure ($X_2 \cdot X_5$). It is noteworthy that the fifth linear factor (compression ratio) is very close to the 5 % red line, which means that it still influences the in-cylinder mean temperature.

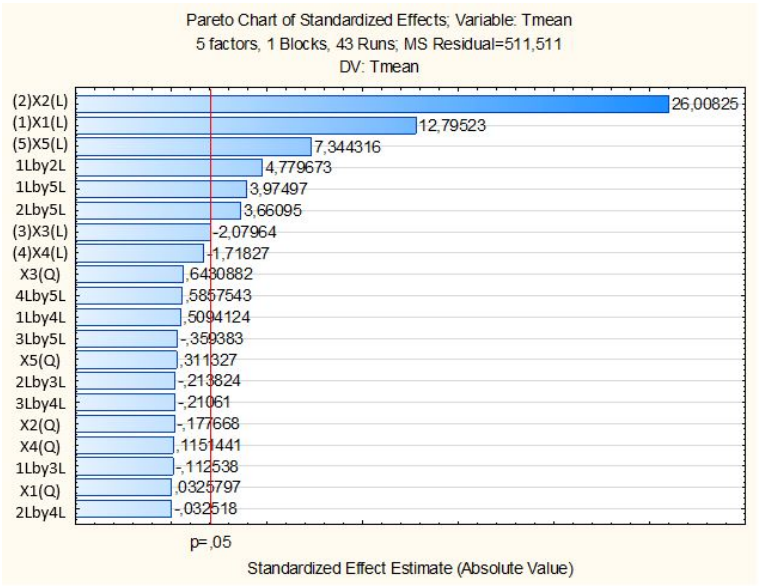

Figure 5.20: Pareto Chart for Mean Temperature in the CCRD.

Studying the influence of these factors in SI engines, we see that the rise in engine speed increases the mean temperature inside the cylinder (AWOGBEMI et al., 2015). The positive regression coefficient for the engine speed factor indicates that the engine speed also positively influences the mean temperature in SACI engines. Furthermore, the mean temperature variation with the fuel-air equivalence ratio reaches a maximum value at lean quasi-

stoichiometric mixtures (HEYWOOD, 1988). Since low-combustion techniques operate with lean mixtures, a positive regression coefficient is what makes the SACI technique similar to the SI, which is the case ($\beta_2 = 89.3770K$). Looking at the intake pressure in SI engines, the higher the pressure in the intake manifold is, the greater the mean in-cylinder and exhaust temperatures are (ANAND; SHARMA; MEHTA, 2011). The model indicates this phenomenon for SACI engines as well, with $\beta_5 = 89.3770\ K/bar$. Finally,

The mean temperature prediction model was the best quadratic fit between the responses, with a R^2 of 97.75%. The red line in Figure 5.21a and the center blue points in Figure 5.21b demonstrate it.

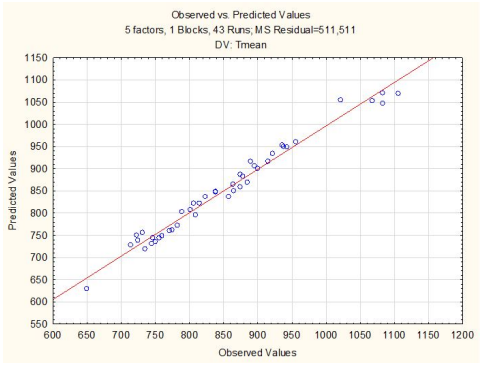

(a) Observed vs. Predicted Values diagram.

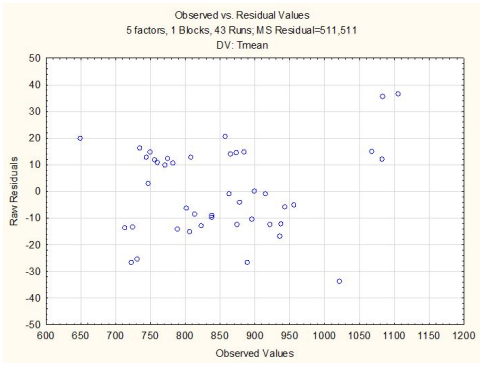

(b) Observed vs. Residual Values diagram.

Figure 5.21: $\overline{T}_{avg}$ observation, prediction and residuals in the CCRD model ($R^2 = 97.75\%$).

5.3.5 Auto-ignition Timing

Lastly, the auto-ignition timing model is:

$$Y_5 = 0.56711 + 3.63472X_1 + 1.04068X_1^2 + 2.23948X_2 - 0.10837X_2^2 + 5.85984X_3 - 0.63870X_3^2 - 4.24372X_4 + 0.24519X_4^2 - 1.86011X_5 + 0.42196X_5^2 + 3.21875X_1X_2 + 1.28125X_1X_3 + 0.53125X_1X_4 + 2.90625X_1X_5 + 1.15625X_2X_3 + 1.15625X_2X_4 + 3.78125X_2X_5 - 2.40625X_3X_4 - 1.03125X_3X_5 + 1.21875X_4X_5 \ [^\circ aTDC] \quad (5\text{-}5)$$

The last response studied in the CCRD is the auto-ignition timing. In the 43 tests, only two cases did not achieve the auto-ignition criteria: Tests 30 and 32. In them, two data adjustments had to be made. Since the response factor is the "Auto-ignition Timing" and there was no auto-ignition, the crank angle

chosen to define the "No auto-ignition" property was the end of SI combustion. So, they were the highest data on AIT, which seems plausible.

Figure 5.22 indicates that there are four significant linear factors and four significant interactions. They are, in order of importance: spark timing (X_3), compression ratio (X_4), engine speed (X_1), fuel-air equivalence ratio times intake pressure ($X_2 \cdot X_5$), engine speed times equivalence ratio ($X_1 \cdot X_2$), engine speed times intake pressure ($X_1 \cdot X_5$), fuel-air equivalence ratio (X_2), and spark timing times compression ratio ($X_3 \cdot X_4$).

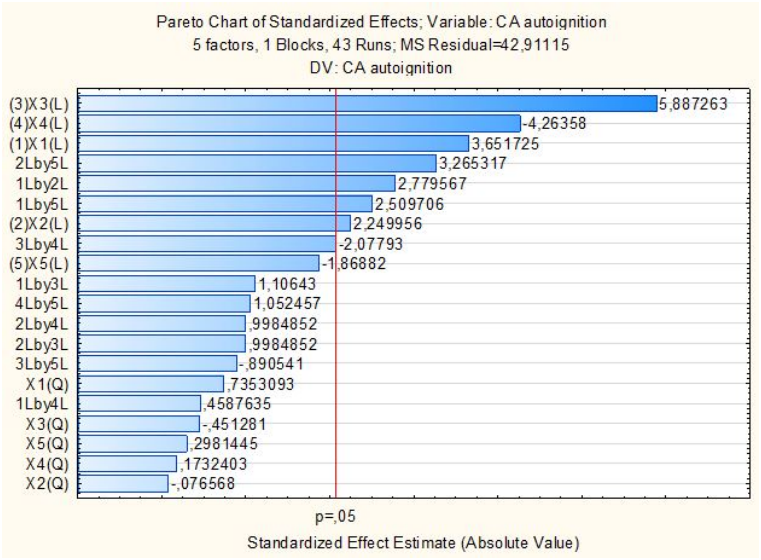

Figure 5.22: Pareto Chart for Auto-ignition timing in the CCRD.

Figure 5.23 highlights the prediction model for the auto-ignition timing. This model is the least accurate indicated by its R_2 of 83.51%. The two adjusted data are the ones with the most residuals. However, it is not trivial to define another pair of values that make physical sense as these do.

To comprehend the AIT in SACI engines we must first investigate the Ignition Delay Time (IDT) and knock in SI engines. The increase in the compression ratio shorts the ignition delay time. Thus, the higher the pressure inside the cylinder is, the faster the mixture self-ignites (TENG; MCCANDLESS; SCHNEYER, 2003). The same behavior happens in SACI engines. The regression coefficient for compression ratio is $-4.24372\ °aTDC$, which means that high compression ratios signify that the auto-ignition happens sooner.

For the fuel-air equivalence ratio, as it gets closer to stoichiometry, it augments the ignition delay time in SI engines (GLAUDE et al., 2011). The model suggests that the equivalence has also a positive influence on the auto-ignition timing in SACI, i.e., mixtures closer to the stoichiometric ratio self-ignite later. This can be explained by the mixture's polytropic coefficient of

compression: lean air-fuel mixtures have higher polytropic coefficients than stoichiometric mixtures (QUINTANA; CASTAñO-MESA; BEDOYA, 2017). So, pressure rises more, and auto-ignition happens earlier in lean mixtures.

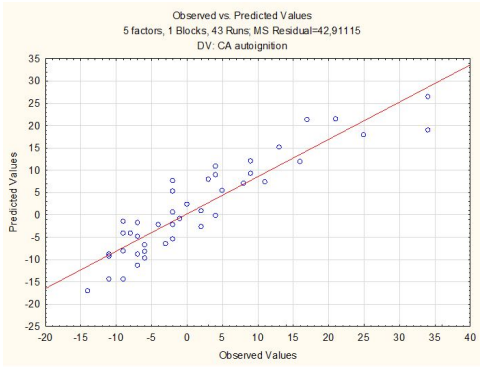

(a) Observed vs. Predicted Values diagram.

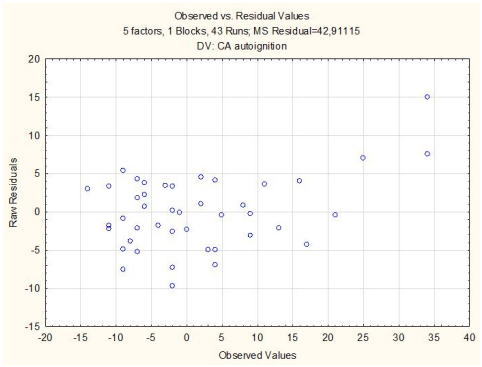

(b) Observed vs. Residual Values diagram.

Figure 5.23: AIT observation, prediction and residuals in the CCRD model ($R^2 = 83.51\%$).

The summary of the most significant factors for each response is displayed in Table 5.11. This overview makes us know that the engine speed and the fuel-air equivalence ratio are important factors to all performance parameters. Additionally, the intake pressure is significant in three of the five responses (thermal efficiency, IMEP, and mean temperature) as well as the spark timing (NOx emissions, mean temperature, and auto-ignition timing). Furthermore, this model indicates that there are no significant interactions on SACI engines and that compression ratio is a significant factor for only one of the responses (auto-ignition timing).

Table 5.11: Most significant factors per response

Response	η_{th}	**IMEP**	**NOx**	$\overline{T}_{avg}$	**AIT**
Significant Linear Factors	RPM P_{int} ϕ	ϕ P_{int} RPM	ϕ RPM θ_s	ϕ RPM θ_s P_{int}	θ_s r_c RPM ϕ
Significant Interactions	RPM $\cdot$ P_{int}	RPM $\cdot$ P_{int} RPM $\cdot$ ϕ	RPM $\cdot$ ϕ RPM $\cdot$ P_{int}	RPM $\cdot$ ϕ RPM $\cdot$ P_{int} $\phi \cdot P_{int}$	$\phi \cdot P_{int}$ RPM $\cdot$ ϕ RPM $\cdot$ P_{int} $\theta_s \cdot r_c$

5.4 Univariate Analysis of the most important factors

To better visualize the factor's impacts and compare them with SI engines, a Univariate Analysis can be done. Thus, five studies are performed:

1. Engine speed variation;
2. Equivalence ratio variation;
3. Spark timing variation;
4. Compression ratio variation;
5. Intake pressure variation.

The subsequent tests are performed with the engine specification from Table 4.5. The naturally aspirated SI and the SACI performed simulations can also help in the comparison of these two different combustion techniques. To make a valid comparison, they will be performing at their normal operating points. Therefore, the factors which do not variate during each UA will acquire the default values from Table 5.12.

Table 5.12: SI and SACI Default Parameters

Parameters	SI	SACI
Engine speed (rpm)	3000	3000
Fuel-Air Equivalence Ratio	1.00	0.65
Spark Timing ($°aTDC$)	-20	-20
Compression Ratio (rpm)	10	17
Intake pressure (bar)	1.0	2.5

5.4.1 Engine speed variation

For the first UA, the engine's performance parameters with an engine speed variation will be studied. Since the engine speed is a factor that is significant to all performance parameters, all of the engine's responses are plotted. Engine speed is ranged between 1,000 and 5,000 rpm, with a step of 500 rpm, enabling the study of its impact on the performance parameters.

The first engine performance parameter analyzed is the thermal efficiency, in Figure 5.24. It is possible to see that SACI thermal efficiency has a maximum value between the engine speeds of 1000 and 5000 rpm, usually around 1500 and 2000 rpm. For the SI engine, we can see that this maximum

value of thermal efficiency occurs at 3000 rpm, at a higher rotation, which is coherent to the litterature value of 2000-3000 rpm (DEMIRCI et al., 2019).

The SACI engine's thermal efficiency drops significantly after 3000 and 3500 rpm, which justifies the SACI strategy implementation at lower engine speeds (WANG et al., 2010). Thus, we can compare SI and SACI efficiencies at lower and higher engine speeds. At lower engine speeds, SACI is about 9 % more efficient than SI. At higher engine speeds, however, SACI can be up to 22 % less efficient.

Moreover, we can see from the graph that the engine speed is much more significant to SACI than to SI. It is noteworthy that engine speed is the most important factor to SACI thermal efficiency after the CCRD analysis.

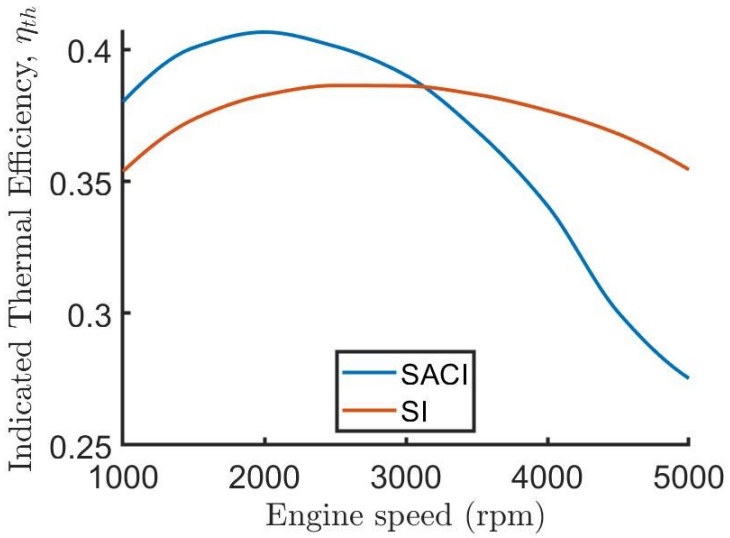

Figure 5.24: Thermal efficiency vs. Engine speed with multiple equivalence ratios.

The mean effective pressure is studied in Figure 5.25. The alteration of the engine speed at the SACI engine is also more significant to SACI than to SI. The IMEP variation can go from -42.4 % from 2000 rpm to 5000 rpm in SACI engines to -15.8 % from 3000 rpm to 5000 rpm in SI engines. Engine speed is only the third single factor of significance in the IMEP. Fuel-air equivalence ratio in the first one, and the intake pressure is the second one, which we will see later.

For SI engines, the maximum value of the IMEP happens at intermediate rotations, near 3000 rpm. Armstrong and Stirrat show, in a similar engine parameter, that the maximum torque is reached between 2500 and 3000 rpm (ARMSTRONG; STIRRAT, 1982)

Furthermore, it is easy to see that the IMEP is very different from SI to SACI engines. SACI's IMEP can be up to 73 % higher at lower engine speeds.

It shows the necessity of having better materials in SACI engines, which can handle higher pressures.

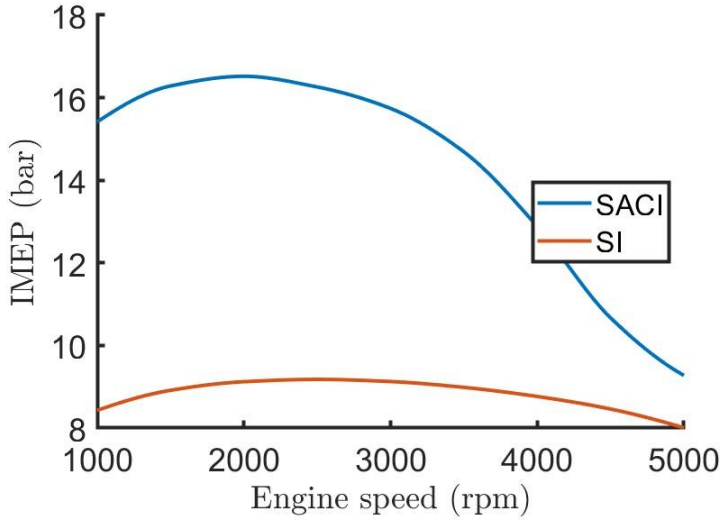

Figure 5.25: IMEP vs. Engine speed with multiple equivalence ratios.

The following important performance parameter is the exhaust air's NOx molecular fraction, in ppm. Figure 5.26 illustrates the effect of engine speed in SACI and SI NOx emissions. As we can see, the increase in engine speed tends to decrease NOx emissions in SACI engines. In SI engines, however, the NOx emissions reaches a maximum value at 3000 rpm. The volumetric efficiency graph, in Figure 5.27, explains it. In SACI engines, the volumetric efficiency decreases significantly after 3000 rpm due to the intake pressure and the mouvement of the valves. Thus, less fresh air enters the cylinder and, consequently, fewer air molecules burn and generate NOx. Additionally, less air means less pressure at the compression stroke and, ultimately, less mean in-cylinder pressure.

In naturally aspirated SI engines, as is the case, the volumetric efficiency does not decrease at the same rate as in SACI engines. It usually have the following values: from 60 % to 80 % (ALAHMER, 2018), So, the thermal efficiency, IMEP, and NOx emissions are not as affected.

The effect of the volumetric efficiency on the SACI engine parameters is noticeable. As we told before, the volumetric efficiency represents the amount of fresh air inside the cylinder, and this physical parameter is sensible for all three performance parameters seen so far. Figure 5.28 shows the direct influence of volumetric efficiency on SACI thermal efficiency. As we can see on the graph, the volumetric efficiency influences the thermal efficiency directly, with a slope of 0.377.

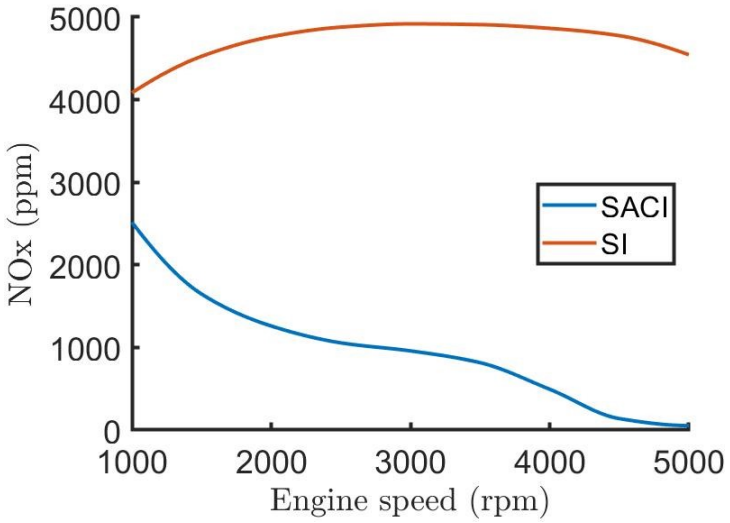

Figure 5.26: NOx vs. Engine speed with multiple equivalence ratios.

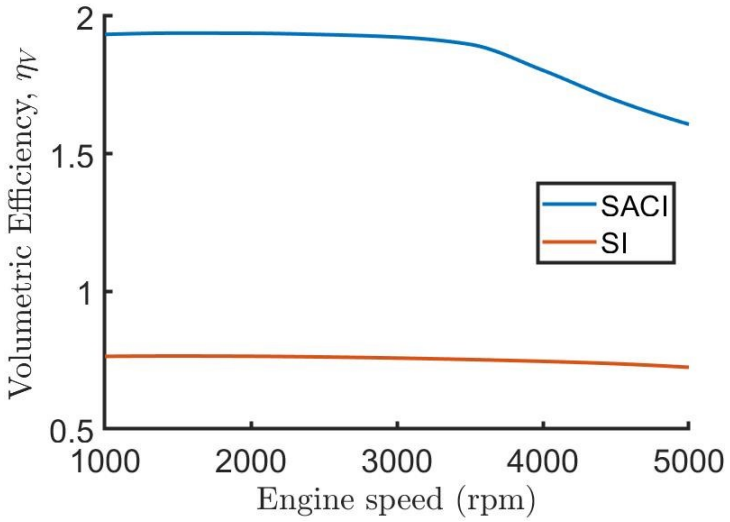

Figure 5.27: Volumetric efficiency vs. Engine speed.

The fourth performance parameter is the mean in-cylinder temperature. Figure 5.29 shows that the faster the engine rotates, the higher its mean temperature is. The heat transfer's comprehension can elucidate this fact. With a higher engine rotation, the air has less time to refresh itself and transfer heat to its surroundings.

In addition, since the volumetric efficiency diminishes with the augmentation of the engine speed, the amount of burned heat inside the cylinder at the end of the intake stroke augments with engine speed. The average temperature of the gases rises, and so does the mean temperature in the cycle. This can be seen in both SACI and SI engines. We can note that SACI has the mean temperature lower than SI, with a difference of almost 200 K.

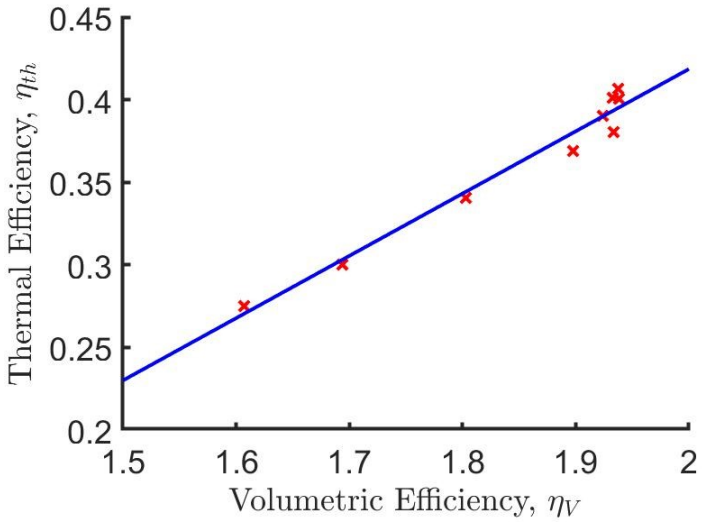

Figure 5.28: Thermal efficiency vs. Volumetric efficiency ($y = -0.335 + 0.377 \cdot x$, $R^2 = 96.86\%$).

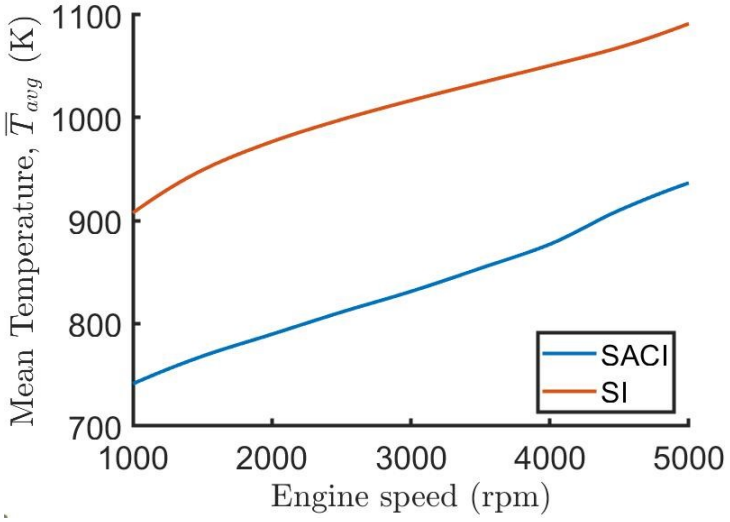

Figure 5.29: Mean temperature vs. Engine speed with multiple equivalence ratios.

HCCI and SACI engines are defined and explained as low-temperature combustion techniques. It comes from the fact that their mixtures are leaner. This technique generates lower in-cylinder temperatures, which are fundamental to decrease the formation of NOx.

Finally, we can study the effects of engine speed on auto-ignition timing. Figure 5.30 tells the influence of engine speed and equivalence ratio on auto-ignition.

We can see that higher engine speeds promote later auto-ignitions. This circumstance could be interpreted again by the influence of volumetric

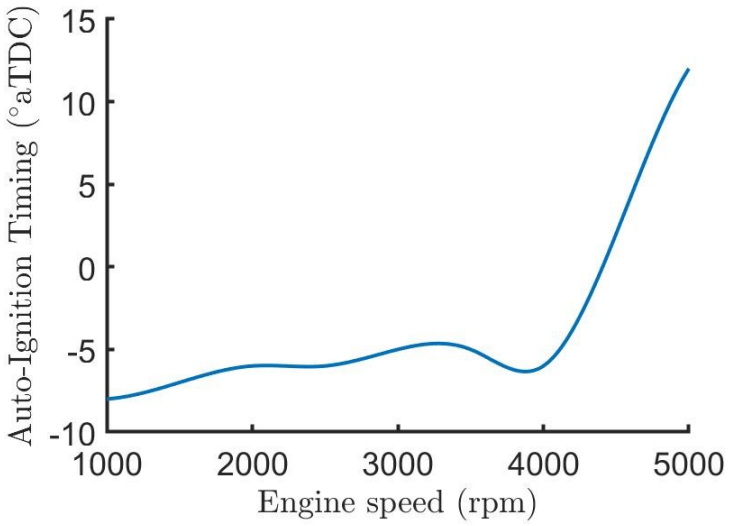

Figure 5.30: Auto-ignition timing vs. Engine speed with multiple equivalence ratios.

efficiency. Since there is less air-fuel mixture in the cylinder, there is less pressure at the end of the compression stroke, meaning that the precursor mass fraction will take longer to generate. In this case, the auto-ignition will happen later. If there is a good amount of air in the cylinder, on the other hand, the pressure at the cylinder will be higher, and the air-fuel mixture will self-ignite sooner.

Figure 5.31 illustrates the influence of different engine speed operating points on the engine's in-cylinder pressure. At lower engine speeds, where the volumetric efficiency does not have relevant variations, the pressure curves are similar (up to 2.9 % of P_{max} difference between 1500 and 3000 rpm). As we told before, the pressure tends to be lower at high engine speeds for SACI engines (-28.9 % from 3000 to 4500 rpm) due to the volumetric efficiency. SI engines, however, show little difference in volumetric efficiency with the engine speed, compared to SACI engines. Hence, the engine's cycle pressures are not very distinct at different rotations.

5.4.2 Fuel-Air Equivalence Ratio variation

To grasp even more knowledge of the influence of fuel-air equivalence ratio on the engine's performance parameters, we have done a univariate study varying the SACI fuel-air mixture equivalence ratio from 0.3 to 1.0, since it operates with lean and very lean mixtures, and SI fuel-air equivalence ratio from 0.9 to 1.1.

By variating the fuel-air equivalent ratio from 0.3 to 1.0 in SACI engines,

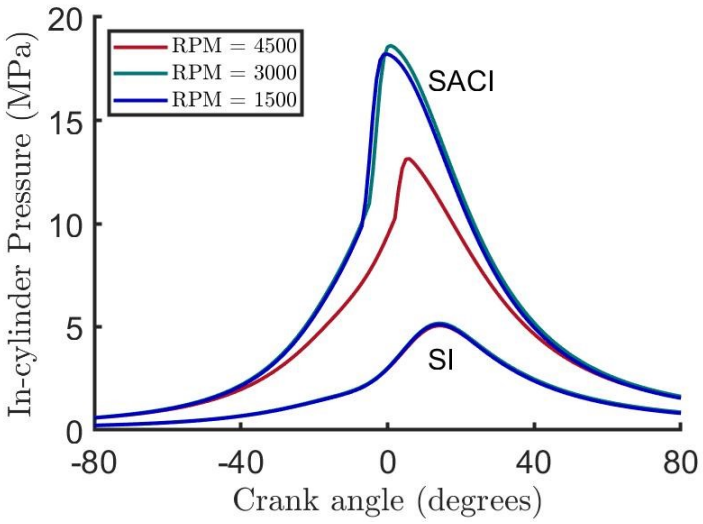

Figure 5.31: In-cylinder pressure vs. Crank angle with multiple engine speeds.

we can see, in Figure 5.32, that there is an optimal point for maximizing thermal efficiency. In this case, the maximum efficiency is obtained at $\phi = 0.5$ with a 40 % thermal efficiency, a value close to what Ortiz-Soto predicted for SACI engines (ORTIZ-SOTO et al., 2019). We can note that this value is 12.7 % higher than the stoichiometric mixture efficiency. That's why, together with the reduction of NOx emissions, low-temperature techniques are commonly studied and applied in the industry.

Furthermore, we can compare the SACI thermal efficiency with the SI. By looking at this graph, one can say that a SACI engine is not much more efficient than an SI engine. However, we must realize that this operating condition is not the optimal one. In fact, it is not efficient at all. At all the operating points, the mixture self-ignited sooner than it is wanted. So, the auto-ignition was harmful to performance. Now, we understand that even at a bad performance point, SACI engines reach the optimal SI thermal efficiency value.

Figure 5.33 illustrates the IMEP as a function of the equivalence ratio. As we can see, the SACI IMEP augments significantly with the fuel-air equivalence ratio. When the engine needs power, the best strategy is to allow more fuel into the cylinder. This procedure provides more usable work since this scheme enables a greater mass of the mixture to burn.

The difference in the IMEP between SI and SACI is, as shown before, big. The mean pressure on the SACI cylinder is almost two times the mean pressure on the SI engine. This shows the evidence perceived by Wang et al., where they realized that IMEP in these configuration would augment about 39 % (WANG et al., 2005).

One can notice that the tendencies exhibited in the previous section

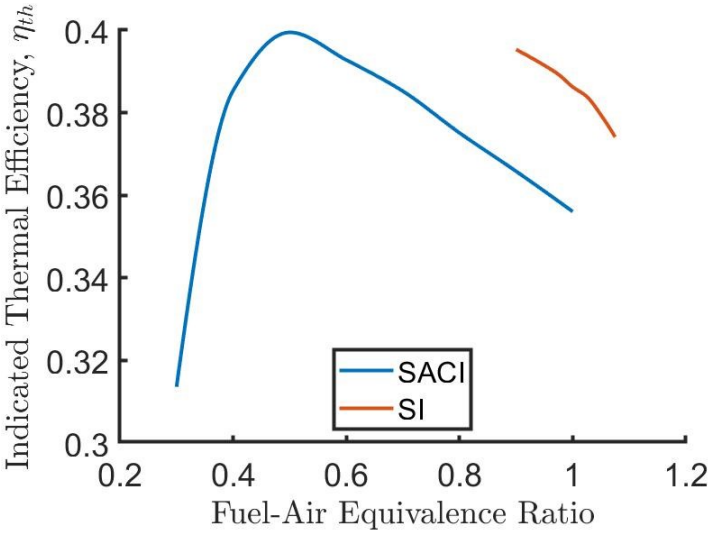

Figure 5.32: Thermal efficiency vs. Equivalence ratio.

are illustrated in these graphs: the SI thermal efficiency increases with lean mixtures and have a maximum value between 0.7 and 0.8 equivalence ratio (HOEKSTRA; BLARIGAN; MULLIGAN, 1996). Plus, the increase in fuel-air equivalence ratio increases the engine's IMEP.

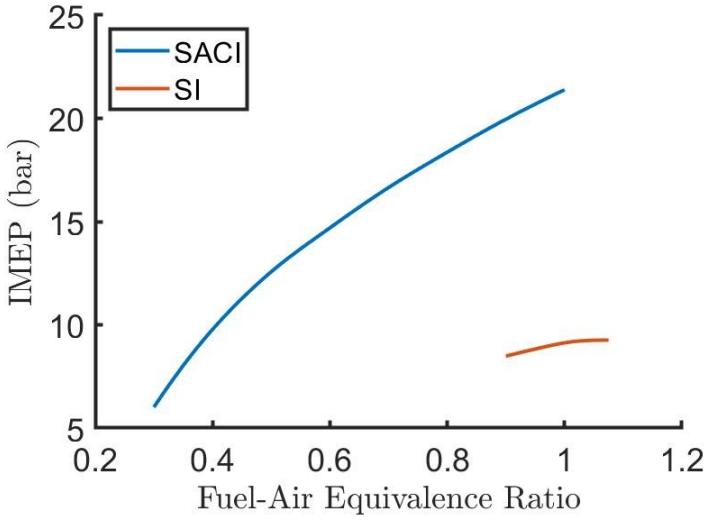

Figure 5.33: IMEP vs. Equivalence ratio.

The outcome of the equivalence ratio of NOx emissions is exhibit In Figure 5.34. The NOx emissions are inferior at low fuel-air equivalence ratios. When we get closer to stoichiometric mixtures, NOx emissions start to increase significantly in SACI engines, as showed Keros et al. (KEROS et al., 2009). That's the main difference between SACI/HCCI engines and the other engines. Since they operate with lean fuel-air ratios, their NOx emissions are low.

NOx emissions have a maximum value in mixtures a little bit leaner than stoichiometry. It is possibly explained by the chemical species' heat capacities and enthalpies, which can emerge in combustion at this equivalence ratio, such as the radical NO which is higher than CO that appears at higher equivalence ratios.

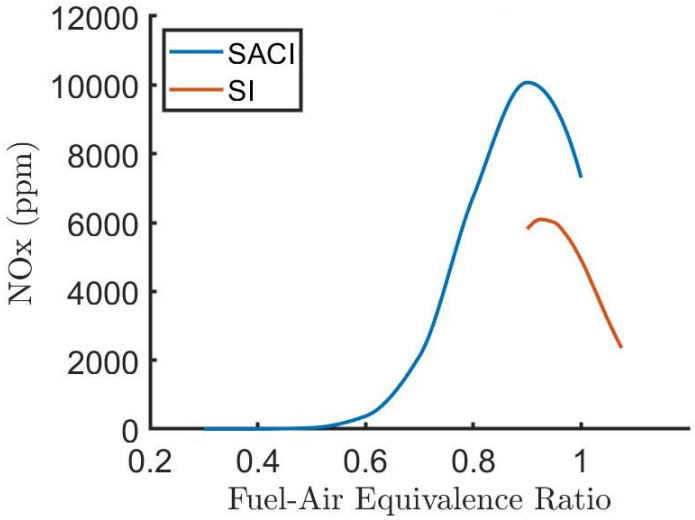

Figure 5.34: NOx vs. Equivalence ratio.

The SACI's mean temperature presents a linear dependence on the fuel-air equivalence ratio. Figure 5.35 demonstrates this tendency and proves why this factor is the most significant for this performance parameter. In these cases, the mean temperature was able to vary +56.9 % from the lower equivalence ratio to the highest. In SACI engines, however, the mean in-cylinder temperature has a maximum value at lean quasi-stoichiometric mixtures, which explains the high NOx formations in these cases.

The auto-ignition timing, however, did not alter significantly in this case. This response exemplifies the considerations done in the previous subsection: this factor has low significance on the auto-ignition timing with these engine's specifications and that the SACI combustion model is not optimized.

Figure 5.37 supports us in the comprehension of these concepts on a pressure versus crank angle graph. The change in the equivalence ratio is not highly significant to the SACI pressure on the compression stroke. The combustion phase, however, changes drastically. Higher fuel-air equivalence ratios allow more of the mixture's mass to burn. This function is illustrated on the maximum pressure point since the more the gases were on stoichiometry, the higher was their maximum pressure. Since the SI fuel-air equivalence ratio does vary like the SACI engine's study, the pressure difference is not as evident as in SACI.

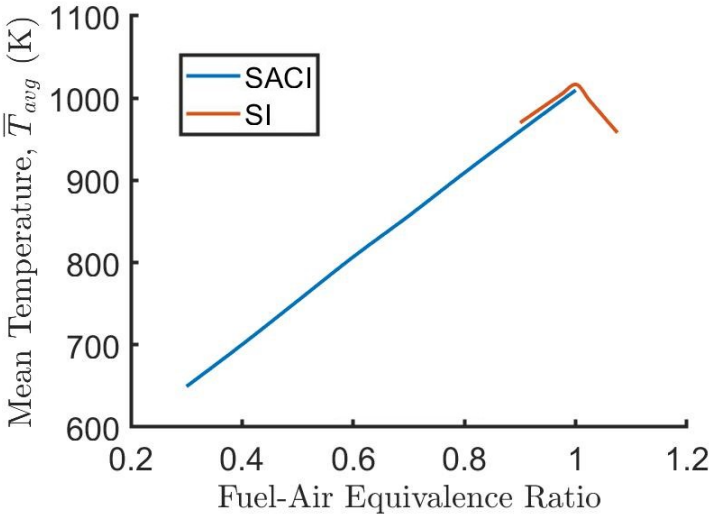

Figure 5.35: Mean temperature vs. Equivalence ratio.

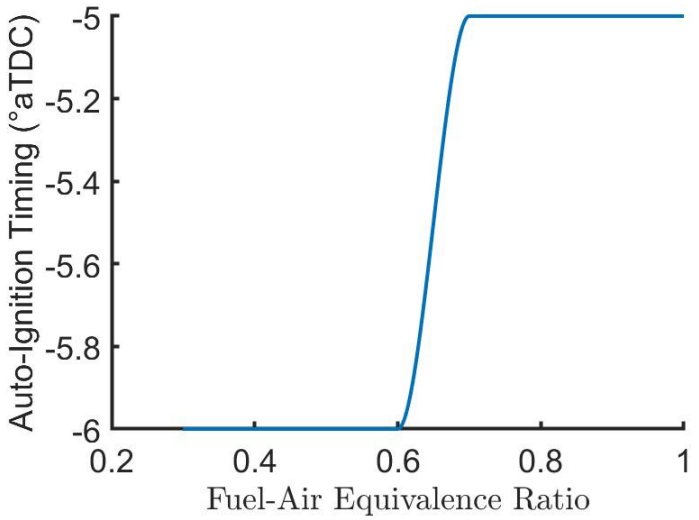

Figure 5.36: Auto-ignition timing vs. Equivalence ratio.

We can also note that not necessarily higher pressure generates higher efficiency. In this case, the most efficient curve has a maximum pressure situated between the lowest and highest maximum pressure.

Besides, we can see that the auto-ignition point of all curves is at the same crank angle. It is clear too that, even though they are simultaneous, the self-ignitions start at different pressures, caused by the SI combustion, which has been taking place for 18 crank angle degrees.

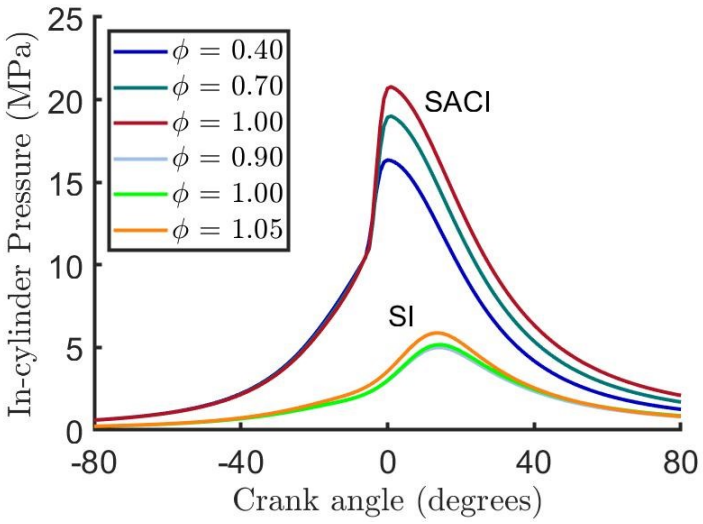

Figure 5.37: In-cylinder pressure vs. Crank angle with multiple fuel-air equivalence ratios.

5.4.3 Spark Timing variation

To understand the impact of the spark timing on the performance parameters, we simulated nine operating points, making the spark timing vary from -40 to 0 $°aTDC$ at both engines. Since the spark timing is a significant factor for NOx formation, mean in-cylinder temperature, and auto-ignition timing, we will only study their influence on these responses.

Figure 5.38 represents the spark timing effect on the NOx concentration. It does not have the same intensity as the fuel-air equivalence ratio. Nevertheless, it has an impact on NOx formation (up to 77.3 %). This influence can be explained by the in-cylinder pressure and the temperature on the combustion chamber.

When the spark happens early, the in-cylinder pressure increases to its maximum values, even though this is not good for thermal efficiency. The high pressure instigates the gas temperature to increase as well. It is on high-temperature combustion that NOx is formed. As the spark timing approaches the TDC, in-cylinder pressure drops, and so does its temperature and NOx emissions. Figure 5.39 exhibits the mean temperature behavior with the change in spark timing here clarified. The explanation serves for SACI and SI engines, although the influence of spark timing on NOx formation in absolute values for SI engines is higher. Moreover, these operating points show that NOx emissions on SI engines are four times higher than in SACI engines. This result justifies the use of this technology for reducing GHG emissions.

The consequence of spark timing in auto-ignition timing is illustrated in

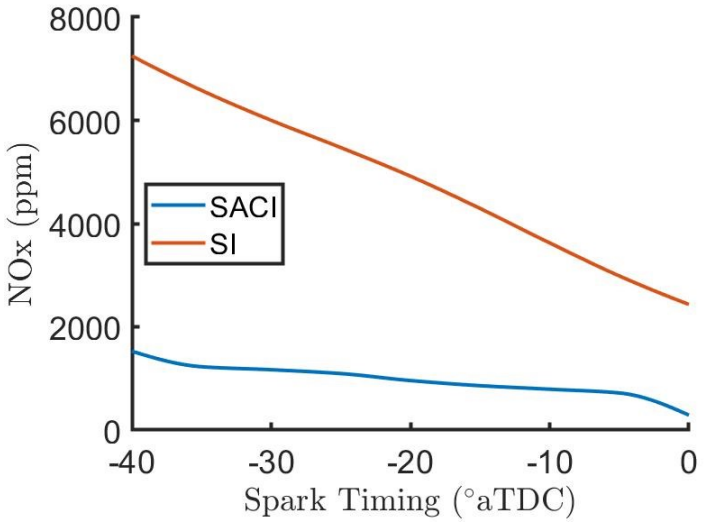

Figure 5.38: NOx vs. Spark timing.

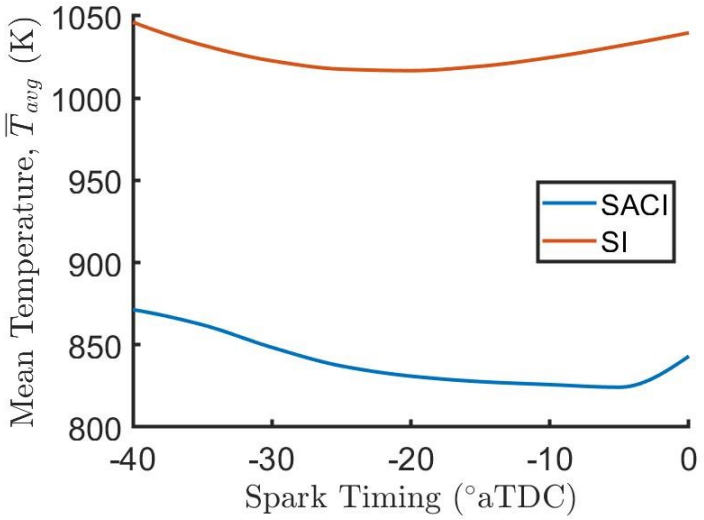

Figure 5.39: Mean temperature vs. Spark timing.

Figure 5.40. The later the spark timing is, the later auto-ignition occurs. The relation between this two parameters is almost direct when the spark timing is away from the TDC. But as it approaches it, the auto-ignition timing starts not to get affected by the spark timing as before. This occurs because the pressure curves with later spark timings are much more alike than the pressure curves whose spark happened early in the compression stroke.

To better understand all these situations, Figure 5.41 plots the in-cylinder pressure versus the crank angle for five different spark timings of each engine type. As mentioned before, the sooner the spark happens, the higher the maximum pressure is, and the earlier the mixture passes the auto-ignition criteria.

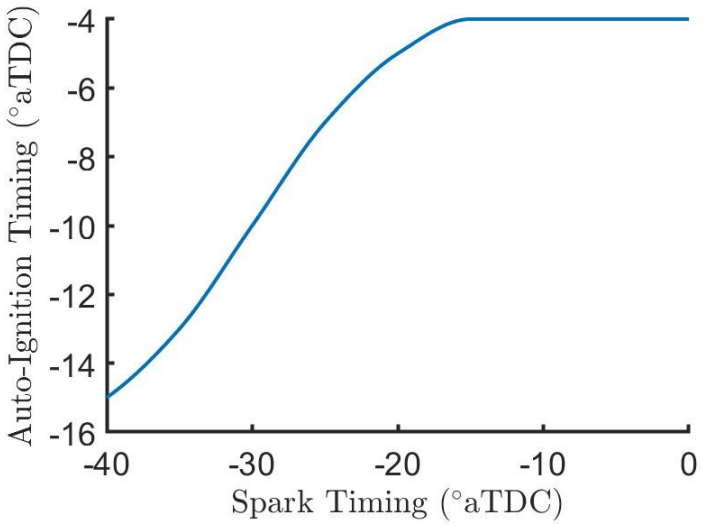

Figure 5.40: Auto-ignition timing vs. Spark timing.

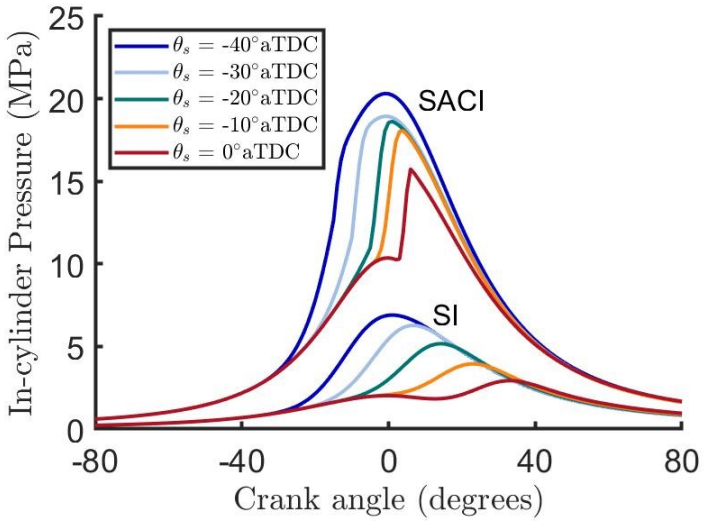

Figure 5.41: In-cylinder pressure vs. Crank angle with multiple spark timings.

Further, later spark timing sets the compression phase to be the same and the extent of precursor mass to be more similar in SACI engines. This condition concludes on auto-ignition occurring closer to each other. For SI engines, the auto-ignition criteria are never reached. The mixture is, then, burned according to Wiebe's function.

5.4.4 Compression Ratio variation

On the contrary to what is expected, the compression ratio is only a significant factor on one response (auto-ignition timing). So, the only factor to be studied with the compression ratio variation is the AIT.

However, to understand this result two graphs are shown in Figure 5.42. They show the influence of compression ratio on thermal efficiency and on the IMEP.

For this investigation, the compression ratio was chosen to variate from 10 to 20 in SACI engines, and 7.5 do 12.5 in SI engines.

As we can see in Figures 5.42a and 5.42b, the compression ratio has an impact on SI engines. We expected that it had a great influence on SACI too. However, this is not what the results point out. If we variate the compression ratio from 7.5 to 12.5 in a SI engine, the thermal efficiency and the IMEP augment 15.5 % and 14.3 %, respectively. In SACI engines, the compression ratio's variation from 10.0 to 20.0 increases these parameters by only 4.5 % and 3.2 %.

This can be explained by the AIT and the pressure curve. In all of these cases, the higher the compression ratio is, the earlier the auto-ignition happens, as seen in Figure 5.43. However, since early burning augments the IMEP and, consequently, the indicated thermal efficiency, early burnings also impact negatively in the thermal efficiency, generating negative work on the compression phase. In the end, these two opposite reactions make the influence of compression ratio less significant in the others performance parameters.

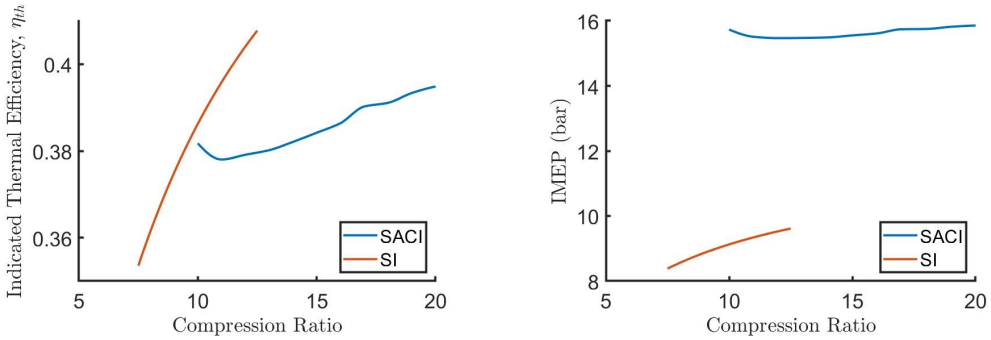

(a) Thermal efficiency vs. Compression ratio.

(b) IMEP vs. Compression ratio.

Figure 5.42: Compression ratio impact on thermal efficiency and IMEP.

Figure 5.43 demonstrates the impact of a SACI engine's compression ratio on the auto-ignition timing. The relation is almost linear, with an approximate linear coefficient of -1.8 $°aTDC$ per unit of compression ratio. This direct connection can be related to the effect of compression ratio to the in-cylinder pressure and temperature. Engines with a high compression ratio augment their pressure rapidly on the compression stroke, facilitating the precursor mass fraction's creation and auto-ignition.

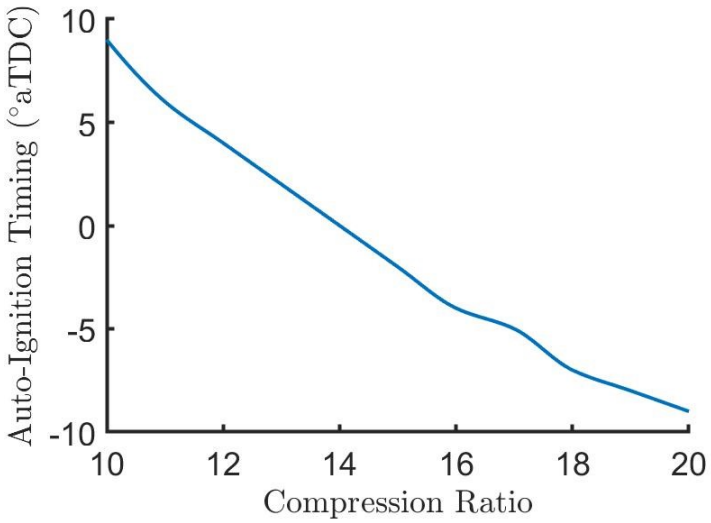

Figure 5.43: Auto-ignition timing vs. Compression ratio.

The graph of the in-cylinder pressure versus the crank angle is shown in Figure 5.44. SACI engines with higher compression ratios have higher pressure and earlier AIT. The other ones, however, show lower pressures, which makes auto-ignition occur later. For SI engines, since the combustion is modeled as being the same, the only change is the maximum pressure and, finally, in the increase of thermal efficiency, IMEP, mean in-cylinder temperature and NOx.

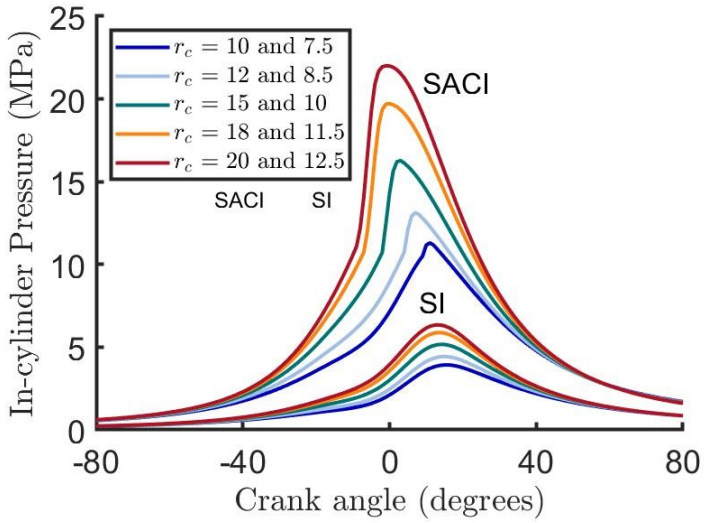

wed

Figure 5.44: In-cylinder pressure vs. Crank angle with multiple compression ratios.

In the compression ratio of 10.0, we observe that the auto-ignition occurs at the end of the SI combustion ($\theta = 9°aTDC$), having almost no effect on the in-cylinder pressure. On $r_c = 20.0$, the AIT is on $\theta = -9°aTDC$, which makes the pressure rise significantly before the TDC and harming the engine's

efficiency. The $r_c = 15.0$, though, has an AIT very close to the TDC, improving thermal efficiency.

5.4.5 Intake Pressure variation

Lastly, we analyze the intake pressure variation, which is a significant factor to thermal efficiency, indicated mean effective pressure and mean temperature in SACI engines. We variate the SACI's intake inlet manifold pressure from 1 to 4 *bar*, and SI from 0.9 to 1.2 *bar*.

Figure 5.45 illustrates thermal efficiency as a function of the intake pressure. With these engine setups, the thermal efficiency decreases with the increase of the intake pressure. This relation could be explained by the fact that all of these cases had a spark timing of $-20°aTDC$. So, all the pressures were high, and the early combustion made them even higher. So, the auto-ignition occurred early in the crank angle, making the SACI combustion work against the thermal efficiency.

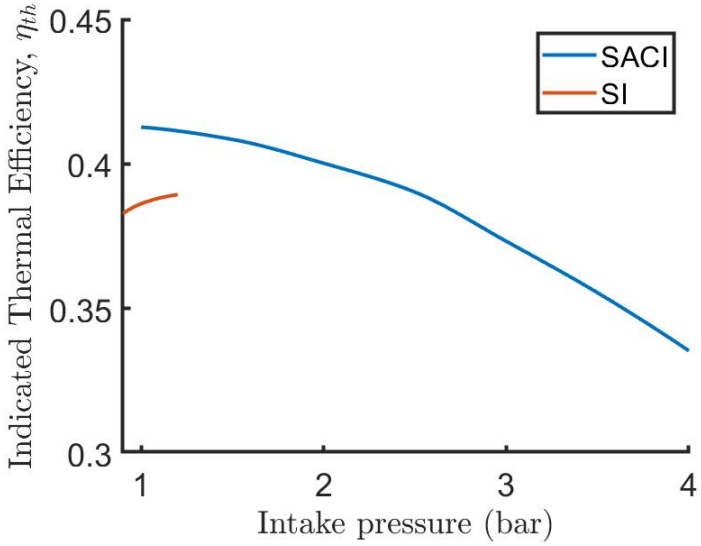

Figure 5.45: Thermal efficiency vs. Intake pressure.

The higher the intake pressure is, the higher the engine's IMEP is, as stated by Figure 5.46. This result agrees with the physical knowledge since the intake pressure increases impact directly the mean pressure of all cycles. This increase can go up to 200 % if the intake pressure augments from 1 to 4 bar.

The mean temperature also increases with intake pressure's raise. The thermodynamic relation between pressure and temperature explicates this behavior seen in Figure 5.47.

NOx emissions as a function of the intake pressure are illustrated in Figure 5.48. In this graph, it is possible to see the difference in emissions

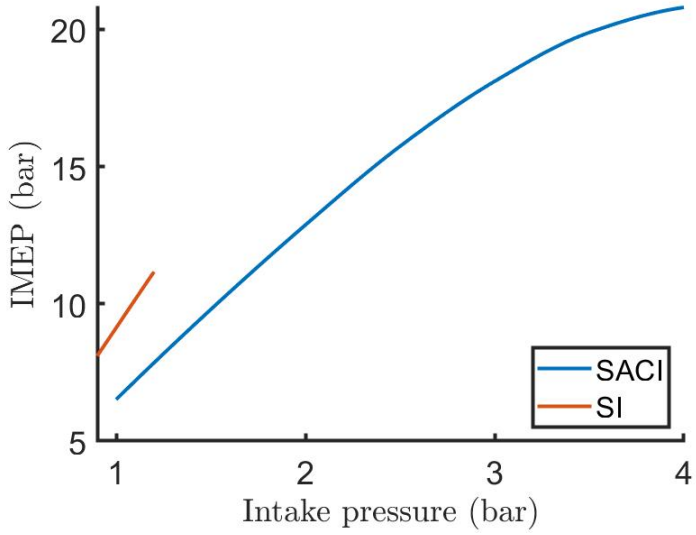

Figure 5.46: IMEP vs. Intake pressure.

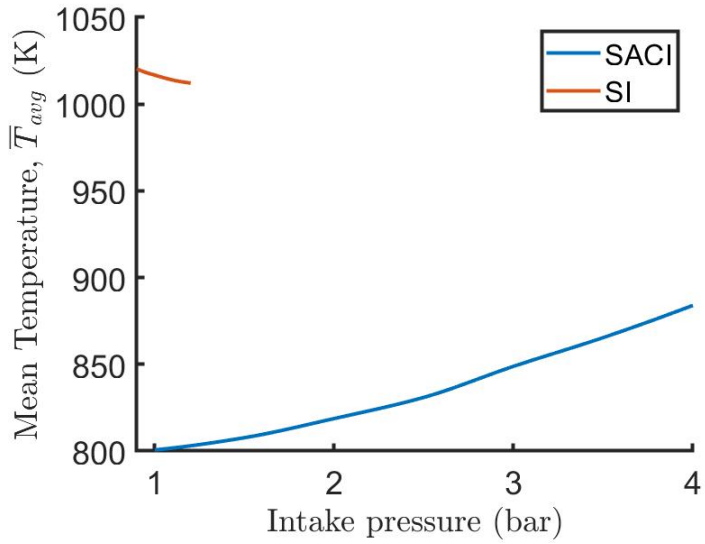

Figure 5.47: Mean temperature vs. Intake pressure.

between SI and SACI engines. SACI engines are at all its range of application four times greener than SI engines.

Ultimately, we can analyze the pressure versus crank angle graph for the five different intake pressures. As it was said previously, Figure 5.49 proves that the auto-ignition occurs earlier at the engines with higher intake pressures. The AIT that happens before the TDC makes the efficiency worst. That's why the thermal efficiency tends to decrease in this engine specification.

However, when applied correctly, the high intake pressure improves efficiency. In the SACI combustion technique, we must impose this transition in the TDC (or at least close to it) so that the engine can benefit from it.

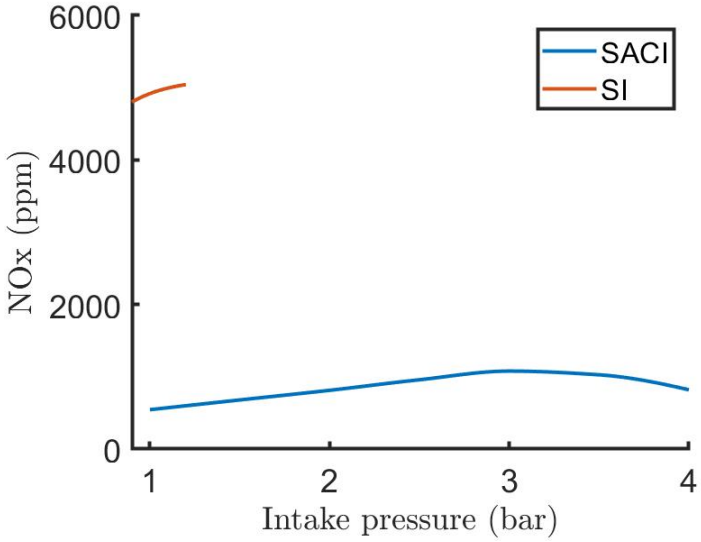

Figure 5.48: NOx emissions vs. Intake pressure.

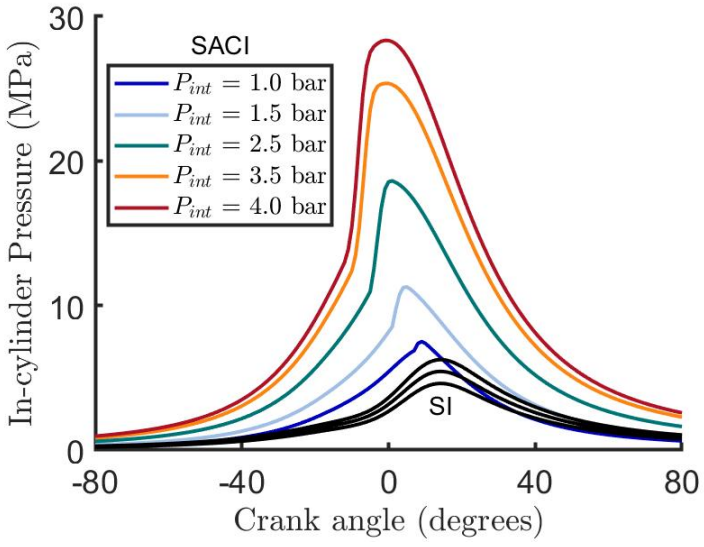

Figure 5.49: In-cylinder pressure vs. Crank angle with multiple intake pressures.

6
Conclusions

In this chapter, we present the main results of this work and outline the perspectives of future studies on the theme.

6.1
Conclusion of the present work

The world has been looking for new technologies to respond to environmental demands and persist in the quest for performance excellence. In the transport sector, researchers appoint that multiple answers serve our current needs and goals. Electric vehicles, hydrogen-based fuel cell vehicles, hybrids vehicles, and internal combustion engine vehicles (with hydrogen fuel or biofuels and new combustion methods) attend different purposes: distinct places and periods in time.

In this work, an ICE simulator was created to predict the main parameters of SI, HCCI and SACI engines. It was built over a two-zone combustion thermodynamic model, and provides 0D simulation information.

With this simulator, it was done a sensibility study to understand the Spark-Assisted Compression Ignition multi-mode combustion and its impact on ICE's performance parameters. The experimental design used was the central composite rotatable design to comprehend the most significant factors and their influence.

The simulations examined the engine's geometric, combustion, and operating parameters in a natural gas SACI engine. We enumerate the main conclusions in the following items:

1. **Effects of engine speed on the SACI performance parameters**: The engine speed was a significant factor in all performance parameters. Since the engine speed is connected to the volumetric efficiency, it dictates the amount of air-fuel mixture that finally enters the cylinder. The SACI combustion method bases itself on the auto-ignition of the unburned gas. So, it is intensely dependent on the mass of fresh air that will self-ignite. SACI engines are more efficient at low engine speed because its thermal efficiency decays significantly at high rotations (up to 42%), that's why they are preferable used in this operating point.

2. **Effects of fuel-air equivalence ratio on the SACI performance parameters**: The fuel-air equivalence ratio was also a significant factor

in all performance parameters. Low-temperature combustion methods, as the SACI, utilizes lean and very lean mixtures so that the cylinder does not reach high temperatures and promote the formation of NOx. In consequence, NOx emissions and the mean in-cylinder temperature are 99 % and 200-300 K lower, respectively, when compared to SI engines. The IMEP augments with the fuel-air equivalence ratio, and the thermal efficiency has a maximum in the lean mixture region, where the mean temperature is low enough to difficult the heat loss to the wall and coolant, and the IMEP is high enough so it can produce work.

3. **Effects of spark timing on the SACI performance parameters**: The spark timing effectively alters the NOx emissions, the in-cylinder mean temperature, and the auto-ignition timing. Both indicated thermal efficiency and mean effective pressure are not sufficiently affected by this factor. The sooner the spark takes place, the higher the in-cylinder pressure will be. High pressures cause high temperatures, which are essential to NOx formation. They also facilitate the auto-ignition process, causing it earlier in the cycle. The spark advance of 20 CAD can generate 11 % of increase in the cylinder pressure between $-20°aTDC$ and $-40°aTDC$.

4. **Effects of compression ratio on the SACI performance parameters**: Remarkably, the compression ratio significantly influences only one of the engine's performance parameters, the auto-ignition timing: at every increase in 1 unit of compression ratio, the auto-ignition timing is advanced approximately in 4 CAD. The difference in pressure at the compression phase caused by the engine's geometric differences impacts the mixture's conditions and auto-ignition. High compression ratios lead to early compression ignitions, which finally remodel the in-cylinder pressure: augment and advance the peak pressure.

5. **Effects of intake pressure on the SACI performance parameters**: The magnitude of the intake pressure defines the pressure's extent across the cycle. When the intake pressure is high, the AIT starts early, which can harm thermal efficiency. Furthermore, it makes the IMEP and the mean in-cylinder pressure increase. High intake pressures make the use of better materials necessary. In the $P_{int} = 4$ bar example, the cylinder had to support pressures up to 30 MPa.

The Spark Ignition and the Spark-Assisted Compression Ignition are two very different combustion modes. Thus, the engine operating points and

the engine geometry are distinct. While SI engines run with stoichiometric mixtures ($\phi \approx 1$), close to atmospheric intake pressure and compression ratios around 10, SACI engines operate at lean/very lean mixtures, intake pressures two to three times higher and compression ratios of 16 to 20. The average thermal efficiency in a SACI engine is 9.0 % higher than in a SI engine. The IMEP is 73 % higher, explaining the necessity of more suitable materials. Finally, the mean in-cylinder temperature is 200 K lower, and NOx emissions are 99.1 % cleaner.

Ultimately, the difference in Homogeneous Charge Compression Ignition and Spark-Assisted Compression Ignition engines is at the start of combustion. Engine's geometry, combustion parameters, compression ratios, and intake pressures are similar. Hence, performance parameters function likewise. The main SACI distinction is the possibility of controlling efficiently the auto-ignition timing, which is not easy to be done in HCCI systems.

6.2 Perspectives

The present work gave an overview of the SACI combustion technology. Nevertheless, additional studies can be performed to investigate other performance aspects and consider new parameters. The following features can be examined in future projects:

1. **Validate and adjust the simulator a with complete experiment data**: It was not possible to fully endorse the generated simulations of the present study due to the lack of main engine information such as valves timing, valves geometry, and conditions at the intake and exhaust manifolds. A group of experiments with a well-known set of parameters could improve the simulator's precision for future studies.

2. **Model valve overlap**: To make the simulator more general, the modeling of valve overlap is an important step. For this, a better model for the engine's initial and final (cycle) gas species is also needed.

3. **Model SACI heat transfer**: A better heat transfer model is needed to account for the cylinder's difference in pressure and temperature compared to regular SI engines. This model can be obtained at the adjustment with complete experimental data.

4. **Model combustion with the minimization of Gibbs free energy**: The combustion modeling can be modified to the minimization of Gibbs free energy. With this method, we can set the wanted burned species,

which permits the analysis of fuels that are not hydrocarbon nor alcohol. However, this approach does not take the intermediate species and the chemical reaction path into account oppositely to the equilibrium constants plan. So, it should have a model for calculating the radical species molar fractions for the calculation of NOx with the Zeldovich mechanism.

5. **Model and simulate different fuels**: The study of SACI with different fuels is interesting. This investigation can lead to the choice of future SACI engines in the industry, considering high thermal efficiencies, low NOx emissions, and low maximum pressures (and IMEP). Another technique that has been drawing attention is the combination of usual fuels and sustainable fuels in an ICE. This procedure supports the idea of gradually substituting fossil fuels with sustainable fuels. The SACI engine can be a strategy done to already existing SI and CI engines for implementing this strategy. Multi-fuel (hydrogen added to gasoline, natural gas, or diesel) combustion on a large scale could reduce GHG emissions in a short period.

6. **Model, simulate and study the effects of stratified air-fuel mixtures**: One SACI characteristic not considered in the simulator is the stratification of the charge. This property indicates that the fuel-air equivalence ratio is not the same at all the cylinder volume. Embedding it on the model and simulating some cases would better outline SACI combustion. Finally, the variation of stratified charge and its intensity could be an interesting object for the performance parameters' univariate analysis.

7. **Model and simulate hydrogen SACI engines**: Hydrogen is seen as the future's fuel. Much research nowadays is done on hydrogen technologies. However, H_2 combustion is not simple to be implemented. Several intermediate species impact the combustion characteristics, and internal aerodynamic studies with an extremelly lighter fuel are not yet robust. Future works could implement the hydrogen combustion reaction and apply it to a SACI engine. This examination can justify hydrogen internal combustion engines with SACI eventually if the performance parameters indicate solid predictions.

8. **Perform detailed parameter study**: Finally, a more detailed examination can be conducted for the other parameters exhibited previously

in this section. It will help the determination of relevant parameters and could serve as a pre-project tool for SACI engines.

7
Bibliography

ALAHMER, A. Performance and emission assessments for different acetone gasoline blends powered of spark ignition engine. **International Journal of Vehicle Structures and Systems**, MechAero Foundation for Technical Research & Education Excellence, v. 10, n. 10.4273/ijvss.10.2.10, 2018. Cited in page 113.

ANAND, K.; SHARMA, R.; MEHTA, P. S. Experimental investigations on combustion, performance, and emissions characteristics of a neat biodiesel-fuelled, turbocharged, direct injection diesel engine. **Biomass and Bioenergy**, Elsevier, v. 35, p. 533–541, 2011. Cited in page 108.

ANTHONY, J. **Design of Experiments for Engineers and Scientists**. Butterworth Heinemann, 2003. ISBN 978-0750647090. Disponível em: <https://www.amazon.com/Design-Experiments-Engineers-Scientists-Antony/dp/0750647094>. Cited in page 80.

ARMSTRONG, D. L.; STIRRAT, G. F. Ford's 1982 3.8l v6 engine. **SAE paper**, SAE, n. 820112, 1982. Cited in page 112.

AWOGBEMI et al. Development and testing of biogas-petrol blend as an alternative fuel for spark ignition engine. **International Journal of Scientific & Technology Research**, IJSTR, n. 2277-8616, 2015. Cited in page 107.

BARROS, S. Implementation of renovabio - brazil's national biofuels policy. **Biofuels, Climate Change/Global Warming/Food Security**, Global Agricultural Information Network, n. BR2021-0008, p. 1866–1890, 2021. Cited in page 23.

BUNTING, B. G. Combustion, control, and fuel effects in a spark assisted hcci engine equipped with variable valve timing. **SAE Technical Paper Series**, SAE International, n. 2006-01-0872, 2006. Cited in page 46.

CBT. **Companhia Brasileira de Tratores: Manual de Motores**. [S.l.: s.n.], 1982. Cited 4 times in pages 9, 31, 32, and 33.

CHALA, G. T.; AZIZ, A. R. A.; HAGOS, F. Y. Natural gas engine technologies: Challenges and energy sustainability issue. **Energies**, v. 11, n. 2934, 2018. Cited 7 times in pages 10, 14, 87, 88, 89, 142, and 147.

CHANG, Y. et al. Effect of ambient temperature and humidity on combustion and emissions of a spark-assisted compression ignition engine. **Journal of Engineering for Gas Turbines and Power**, ASME, v. 139, n. 051501, 2017. Cited 4 times in pages 10, 47, 48, and 49.

CHEN, L. et al. Effects of partitioned fuel distribution on auto-ignition and knocking under spark assisted compression ignition conditions. **Applied Energy**, Elsevier, v. 260, n. 114269, 2020. Cited in page 48.

DEC, J. E. Advanced compression-ignition engines - understanding the in-cylinder processes. **Proceedings of the Combustion Institute**, v. 32, p. 2727, 2009. Cited in page 40.

DEMIRCI, O. K. et al. Performance and emission characteristics of a miller cycle engine. **International Journal of Automotive Engineering and Technologies**, IJAET, v. 7, p. 107–116, 2019. Cited in page 112.

DIGITALSCIENCE. **Dimensions [Software]**. [S.l.]: Accessed on 1 September 2021, 2021. (https://app.dimensions.ai). Cited 2 times in pages 45 and 49.

DIMITRIOU, P. et al. Experimental and simulation analysis of natural gas-diesel combustion in dual-fuel engines. **Frontiers in Mechanical Engineering**, v. 6, n. 543808. Cited in page 102.

ECONOMIST, T. **The death of the internal combustion engine**. TheEconomist.com, 2017. (The Economist). Disponível em: <https://www.economist.com/leaders/2017/08/12/the-death-of-the-internal-combustion-engine>. Cited in page 23.

EIA. **Annual Energy Outlook**. U.S. Energy Information Administration, 2021. (Independent Statistics & Analysis). Disponível em: <http://www.eia.gov/>. Cited 3 times in pages 9, 20, and 21.

EPE. **Brazilian Energy Balance**. Empresa de Pesquisa Energética, 2020. (Ministry of Mines and Energy – MME). Disponível em: <https://www.epe.gov.br/pt/publicacoes-dados-abertos/publicacoes/balanco-energetico-nacional-2020>. Cited 3 times in pages 9, 22, and 23.

EXXONMOBIL. **Outlook for energy: a view to 2040**. ExxonMobil.com, 2017. Disponível em: <https://corporate.exxonmobil.com/>. Cited in page 23.

FAGUNDEZ, J. L. S. et al. Comparative analysis of different heat transfer correlations in a two-zone combustion model applied on a si engine fueled with wet ethanol. **Applied Thermal Engineering**, Elsevier, v. 115, p. 22–32, 2017. Cited in page 86.

FERGUSON, C. R.; KIRKPATRICK, A. T. **Internal Combustion Engines: Applied Thermosciences**. John Wiley & Sons, Ltd, 2016. Disponível em: <https://books.google.com.br/books?id=Lv8kCgAAQBAJ>. Cited 12 times in pages 10, 27, 36, 39, 40, 51, 55, 58, 61, 62, 64, and 79.

FURLANI, C. E. A. **Motores à Combustão Interna**. UNESP, São Paulo, 2006. (Laboratório de Máquinas e Mecanização Agrícula). Disponível em: <http://lamma.com.br/private/docs/c0d4b9692a8c31cab7cda401c9382350.pdf>. Cited 4 times in pages 9, 30, 37, and 39.

GHOJEL, J. Review of the development and applications of the wiebe function. **International Journal of Engineering Research**, IJER, v. 11, p. 297–312, 2010. Cited in page 61.

GLAUDE, P. A. et al. Dme as a potential alternative fuel for gas turbines: A numerical approach to combustion and oxidation kinetics. **ASME 2011 Turbo Expo: Turbine Technical Conference and Exposition**, Proceedings of ASME Turbo Expo 2011, n. 10.1115/GT2011-46238, 2011. Cited in page 109.

HAIRUDDIN, A. A.; WANDEL, A. P.; YUSAF, T. A homogeneous charge compression ignition engine: An introduction. **Journal of Mechanical Engineering and Sciences**, UMP, v. 7, p. 1042–1052, 2014. Cited 2 times in pages 27 and 40.

HAMI, A. E.; POUGNET, P. **Embedded Mechatronic Systems 2: Analysis of Failures, Modeling, Simulation and Optimization**. Elsevier Ltd., 2015. ISBN 978-1-78548-014-0. Disponível em: <https://doi.org/10.1016/C2014-0-04711-9>. Cited 2 times in pages 10 and 81.

HANSON, R.; SALIMIAN, S. **Survey of Rate Constants in the N/H/O System**. [S.l.]: Springer-Verlag, 1984. (Chapter 6 in Combustion Chemistry (W. Gardiner, Jr., ed.)). Cited 2 times in pages 14 and 75.

HAWKINS, T. R. et al. Comparative environmental life cycle assessment of conventional and electric vehicles. **Journal of Industrial Ecology**, v. 17, p. 53–64, 2013. Cited in page 24.

HEYWOOD, J. Pollutant formation and control in spark ignition engines. **Progress in Energy and Combustion Science**, PECS, v. 1, p. 135–164, 1976. Cited in page 75.

HEYWOOD, J. B. **Internal Combustion Engine Fundamentals**. [S.l.]: McGraw-Hill, Inc., 1988. (McGraw-Hill Series in Mechanical Engineering). ISBN 0-07-028637-X. Cited 6 times in pages 14, 37, 39, 67, 85, and 108.

HIGASHISONO, M.; TAKEUCHI, K.; HARA, H. he new isuzu 1.8 liter 4-cylinder diesel engine for the united states market. **SAE Transition**, SAE International, v. 91, n. 820116, 1982. Cited in page 103.

HISTORY. **Climate Change History**. History.com, 2017. Disponível em: <https://www.history.com/topics/natural-disasters-and-environment/history-of-climate-change>. Cited in page 19.

HOEKSTRA, R. L.; BLARIGAN, P. V.; MULLIGAN, N. Nox emissions and efficiency of hydrogen, natural gas, and hydrogen/natural gas blended fuels. **Journal of Fuels and Lubricants**, SAE International, v. 105, p. 761–773, 1996. Cited 2 times in pages 102 and 118.

IEA. **World Energy Outlook**. International Energy Agency, 2020. Disponível em: <http://www.iea.org/weo>. Cited 2 times in pages 9 and 21.

IJER, E. The future of the internal combustion engine. **International Journal of Engine Research**, SAGE, v. 21, n. 1, p. 3–10, 2019. Cited 2 times in pages 25 and 26.

KALGHATGI, G. Is it really the end of internal combustion engines and petroleum in transport? **Applied Energy**, Elsevier, v. 225, p. 965–974, 2018. Cited 3 times in pages 9, 24, and 25.

KEROS, P. E. et al. An experimental investigation of the exhaust emissions from spark-assisted homogeneous charge compression ignition in a single-cylinder research engine. **Proceedings of the ASME Internal Combustion Engine Division**, ASME, n. ICES2009-76083, 2009. Cited 4 times in pages 10, 47, 106, and 118.

KIMURA, T. On dormand-prince method. **Manuales y documentos de la Facultad de Química - UNAM**, UnamAmid Facultad de Química, 2009. Cited in page 78.

MA, H. et al. A new comparison between the life cycle greenhouse gas emissions of battery electric vehicles and internal combustion vehicles. **Energy Policy**, Elsevier, v. 44, p. 160–173, 2012. Cited in page 24.

MALONEY, J. O. **Perry's Chemical Engineer's Handbook**. McGraw-Hill, 2008. Disponível em: <DOI:10.1036/0071511245>. Cited in page 55.

MATHIESEN, K. **Coal to power India for 'decades to come'**. climatechangenews.com, 2017. Disponível em: <https://www.climatechangenews.com/2017/08/28/coal-power-india-decades-come-says-government-planning-body/>. Cited in page 24.

MATSUDA, T. et al. A study of gasoline-fueled hcci engine—mode changes from si combustion to hcci combustion. **SAE TECHNICAL PAPER SERIES**, Nissan Motor Co., Ltd., v. 1, p. 0050, 2008. Cited 2 times in pages 9 and 42.

MAZDA. **SkyActiv-X**. Mazda Motor, 2018. Disponível em: <https://www.mazda.com/en/innovation/mazda-stories/engineers/skyactiv-x/>. Cited 3 times in pages 10, 42, and 49.

MAZDA. **SKYACTIV-X: a revolutionary new combustion engine**. Mazda Motor Europe, 2019. Disponível em: <https://www.mazda-press.com/services/>. Cited 7 times in pages 9, 14, 27, 28, 43, 49, and 50.

MAZDA. **Updated e-Skyactiv X engine makes its debut in the 2021 Mazda CX-30 and 2021 Mazda3**. Mazda Motor Europe, 2021. Disponível em: <https://www.insidemazda.co.uk/2021/03/01/updated-e-skyactiv-x-engine-makes-its-debut-in-the-2021-mazda-cx-30-and-2021-mazda3/>. Cited 2 times in pages 14 and 50.

MCBRIDE, B. J.; GORDON, S.; RENO, M. A. Coefficients of calculating thermodynamic and transport properties of individual species. **NASA Technical Memorandum**, NASA Scientific and Technical Information Program, n. 4513, 1993. Cited 3 times in pages 14, 55, and 57.

MIDDLETON, R. J. et al. The effect of spark timing and negative valve overlap on spark assisted compression ignition combustion heat release rate. **Proceedings of the Combustion Institute**, Elsevier, v. 35, p. 3117–3124, 2015. Cited in page 48.

MILLER, J.; BOWMAN, C. Mechanism and modeling of nitrogen chemistry in combustion. **Progress in Energy and Combustion Science**, PECS, v. 15, p. 287–338, 1989. Cited in page 75.

NATES, R. J.; YATES, A. D. B. Knock damage mechanisms in spark-ignition engines. **Journal of Fuels and Lubricants**, SAE International, v. 103, p. 1970–1980, 1994. Cited in page 41.

NIST/SEMATECH. **e-Handbook of Statistical Methods**. [s.n.], 2012. Disponível em: <https://doi.org/10.18434/M32189>. Cited in page 80.

NORDELöF, A. et al. Environmental impacts of hybrid, plug-in hybrid, and battery electric vehicles—what can we learn from life cycle assessment? **International Journal of Life Cycle Assess**, MODERN INDIVIDUAL MOBILITY, v. 19, p. 1866–1890, 2014. Cited 2 times in pages 9 and 25.

OBERT, E. F. **Motores de Combustão Interna**. Editora Globo, 1971. Disponível em: <https://books.google.com.br/books/about/Motores_de_combustao_interna.html?id=i0BgkQEACAAJ&redir_esc=y>. Cited 3 times in pages 26, 30, and 37.

OLIKARA, C.; BORMAN, G. L. A computer program for calculating properties of equilibrium combustion products with some applications to i.c. engines. **SAE International**, SAE, 1975. Cited 2 times in pages 71 and 73.

ORTIZ-SOTO, E. A. et al. Thermodynamic efficiency assessment of gasoline spark ignition and compression ignition operating strategies using a new multi-mode combustion model for engine system simulations. **International Journal of Engine Research**, SAGE, v. 20, n. 3, p. 304–326, 2019. Cited 5 times in pages 10, 28, 47, 48, and 117.

PERSSON, H.; JOHANSSON, B.; REMóN, A. The effect of swirl on spark assisted compression ignition (saci). **SAE Technical Paper Series**, SAE International, n. 2007-01-1856, 2007. Cited in page 46.

PERSSON, H. et al. The effect of swirl on spark assisted compression ignition (saci). **SAE Technical Paper Series**, SAE International, n. 2008-01-2401, 2008. Cited 2 times in pages 42 and 46.

PIPITONE, E. A new simple friction model for s. i. engine. **SAE Technical Paper**, SAE International, 2009. Cited in page 89.

PIPITONE, E.; BECCARI, S. A comprehensive model for the auto-ignition prediction in si engines fuelled with mixtures of gasoline and methane based fuel. **Journal of Engineering for Gas Turbines and Power**, ASME, doi:10.1115/1.4041675, 2018. Cited 2 times in pages 68 and 69.

POOMPIPATPONG, C.; CHOI, G. H.; TANGSIRIWORAKUL, C. Performance and exhaust emission studies of a large lng-diesel engine operating with different gas injector's characteristics. **International Journal of Advanced Science and Technology**, KMUTNB, v. 7, n. 2, p. 59–66, 2014. Cited in page 102.

QIAO, Q. et al. Cradle-to-gate greenhouse gas emissions of battery electric and internal combustion engine vehicles in china. **Applied Energy**, Elsevier, v. 204, p. 1399–1411, 2017. Cited in page 24.

QUINTANA, S. H.; CASTAñO-MESA, E. S.; BEDOYA, I. D. Experimental study of polytropic coefficient for an air cooled high compression ratio-spark ignition engine fueled with natural gas, biogas, and propane-syngas blend. **Energy & Fuels**, American Chemical Society, n. DOI: 10.1021/acs.energyfuels.7b03063, 2017. Cited 2 times in pages 97 and 110.

RIBBENS, W. B. **Understanding Automotive Electronics: An Engineering Perspective**. Elsevier Inc., 2017. ISBN 978-0-12-810434-7. Disponível em: <https://doi.org/10.1016/C2016-0-00011-6>. Cited in page 106.

ROBISON, J. A.; BREHOB, W. M. The influence of improved mixture quality on engine exhaust emissions and performance. **Journal of the Air Pollution Control Association**, v. 17, n. 7, p. 4–53, 1967. Cited in page 103.

ROWLEY, R. L. et al. Dippr® data compilation of pure chemical properties. **Design Institute for Physical Properties**, American Institute of Chemical Engineers (AIChE), 2007. Cited 2 times in pages 14 and 57.

RYAN, T. W.; MATHEAUS, A. C. Fuel requirements for hcci engine operation. **SAE International**, Spring Fuels and Lubricants Meeting, v. 1, p. 1813, 2003. Cited in page 41.

SAGE. **International Journal of Engine Research**. SAGE, 2019. Disponível em: <s://us.sagepub.com/en-us/nam/journal/international-journal-engine-research>. Cited in page 25.

SREMEC, M. et al. Influence of compression ratio on performance and emissions of natural gas fuelled si engine. **Croatia Science Foundation**, n. 32, p. 1–15, 2017. Cited 2 times in pages 14 and 90.

SRIVASTAVA, S. **MDB Simulation on IC Engine Valve train**. [s.n.], 2020. (skill-lync). Disponível em: <https://skill-lync.com/projects/mbd-simulation-on-ic-engine-valve-train-49>. Cited 2 times in pages 9 and 34.

TENG, H.; MCCANDLESS, J. C.; SCHNEYER, J. B. Compression ignition delay (physical + chemical) of dimethyl ether – an alternative fuel for compression-ignition engines. **Journal of Fuels and Lubricants**, SAE International, n. 2003-01-0759, 2003. Cited in page 109.

UNFCCC. **Paris Agreement**. United Nations Framework Convention on Climate Change, 2015. Disponível em: <https://unfccc.int/process-and-meetings/the-paris-agreement/the-paris-agreement>. Cited in page 19.

UNTV. **Brazil: The Ethanol Revolution**. United Nations TV, 2008. (US in action). Disponível em: <https://www.un.org/webcast/pdfs/unia1136.pdf>. Cited in page 22.

WANG, Z. et al. Combustion visualization and experimental study on spark induced compression ignition (sici) in gasoline hcci engines. **Energy Conversion and Management**, Elsevier, v. 51, p. 908–917, 2010. Cited 4 times in pages 10, 47, 48, and 112.

WANG, Z. et al. Effects of spark ignition and stratified charge on gasoline hcci combustion with direct injection. **SAE Technical Paper Series**, SAE International, n. 2005-01-0137, 2005. Cited 4 times in pages 9, 45, 46, and 117.

WANITSCHKE, A.; HOFFMANN, S. Are battery electric vehicles the future? an uncertainty comparison with hydrogen and combustion engines. **Environmental Innovation and Societal Transitions**, Elsevier, v. 35, p. 509–523, 2020. Cited in page 26.

WEART, S. R. **The Discovery of Global Warming**. Harvard University Press, 2008. (New Histories of Science, Technology, and Medicine). Disponível em: <https://www.hup.harvard.edu/catalog.php?isbn=9780674031890>. Cited in page 19.

WEC. **Global transport scenarios 2050**. World Energy Council, London, 2017. Disponível em: <http://www.worldenergy.org/wp-content/uploads/2012/09/wec_transport_scenarios_2050.pdf>. Cited in page 24.

WHITELEY, M. Is mazda the savior of the internal combustion engine? **Automobile News**, Motortrend, 2017. Cited in page 45.

WOSCHNI, G. A universally applicable equation for the instantaneous heat transfer coefficient in the internal combustion engine. **SAE International**, SAE, n. 670931, 1967. Cited in page 66.

WRI. **Climate Analysis Indicators Tool**. World Resources Institute, 2017. (Center for Climate and Energy Solutions - C2ES). Disponível em: <https://www.c2es.org/content/international-emissions/>. Cited in page 20.

YANG, X.; ZHU, G. G. A control-oriented hybrid combustion model of a homogeneous charge compression ignition capable spark ignition engine. **Journal of Automobile Engineering**, SAGE, v. 226, p. 1380–1395, 2012. Cited 2 times in pages 9 and 45.

YIN, S. Volumetric efficiency modeling of a four sroke ic engine. **Colorado State University**, Thesis for Master of Science degree (Department of Mechanical Engineering), 2017. Cited 2 times in pages 62 and 63.

ZHANG, F. et al. Direct numerical simulation of flame/spontaneous ignition interaction fueled with hydrogen under saci engine conditions. **International Journal of Hydrogen Energy**, Elsevier, v. 42, p. 3842–3852, 2017. Cited in page 48.

ZHAO, H. **HCCI and CAI Engines for the Automotive Industry**. Woodhead Publishing, 2007. ISBN 184569354X, 9781845693541. Disponível em: <https://books.google.com.br/books?id=nQikAgAAQBAJ&hl=pt-BR&source=gbs_navlinks_s>. Cited 3 times in pages 14, 42, and 92.

ZHENG, L.; ZHANG, X. **Modeling and Analysis of Modern Fluid Problems**. Academic Press, 2017. ISBN 978-0-12-811753-8. Disponível em: <https://www.sciencedirect.com/book/9780128117538/modeling-and-analysis-of-modern-fluid-problems#book-description>. Cited in page 77.

ZHOU, L. et al. Effects of applying egr with split injection strategy on combustion performance and knock resistance in a spark assisted compression ignition (saci) engine. **Applied Thermal Engineering**, Elsevier, v. 145, p. 98–109, 2018. Cited in page 48.

A
Appendix A

To understand the simulator plots capabilities and help in the manuscript's numerical modeling explaination, the naturally aspirated SI engine from TableA.1 was simulated. The results are ploted in this Appendix.

Table A.1: SI Engine Specification Example (CHALA; AZIZ; HAGOS, 2018)

Geometric parameters	
Number of cylinders	4
Bore (mm)	83
Stroke (mm)	81.4
Half-stroke to Rod Ratio	0.271
Total Displacement Volume (cm^3)	1,761
Compression Ratio	9.25
Valves timing	
IVO	0^oaTDC
IVC	45^oaBDC
EVO	35^obTDC
EVC	0^oaTDC
Operating point	
Engine speed (rpm)	2000
Fuel type	Natural gas
Equivalence Ratio (ϕ)	1.00
P_{int} (bar)	1.0
T_{int} (K)	380
T_{exh} (K)	480
Wiebe parameters	
a_W	6.9078
θ_s	-20^oaTDC
θ_d	46^o
m_W	3.20

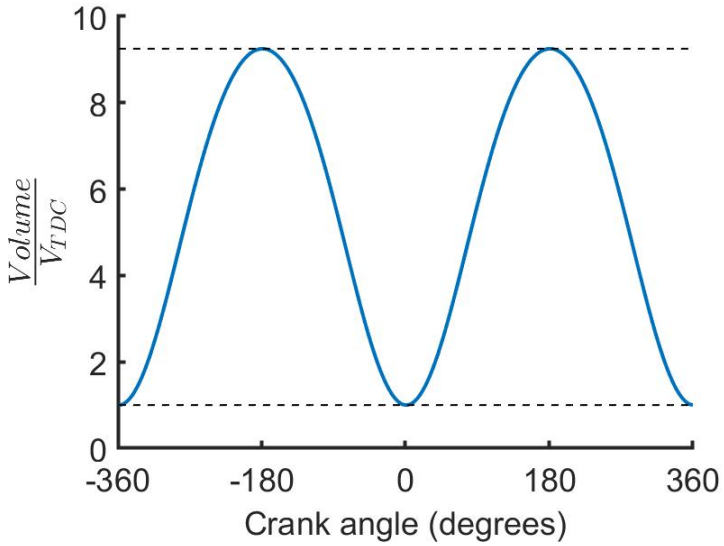

Figure A.1: In-cylinder volume in function of the crank angle.

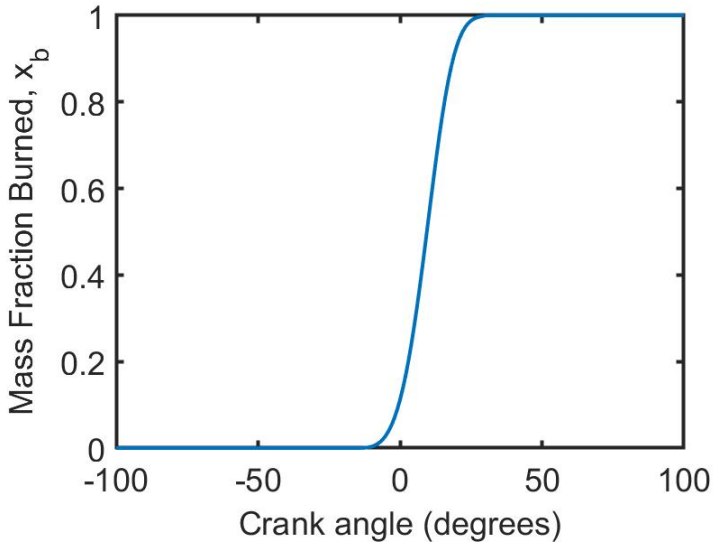

Figure A.2: Mass fraction burned in function of the crank angle.

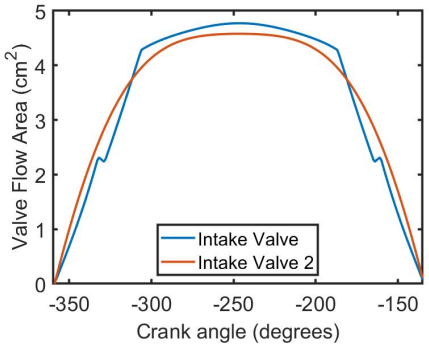

(a) Valve Flow Area at the intake stroke.

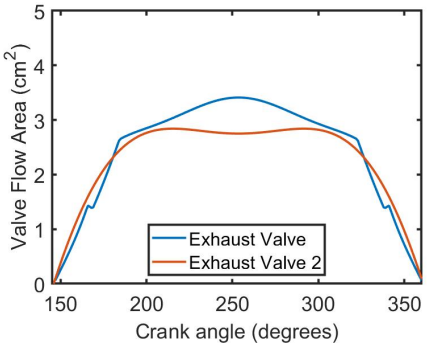

(b) Valve Flow Area at the exhaust stroke.

Figure A.4: Valve Flow Area: (a) Intake; (b) Exhaust.

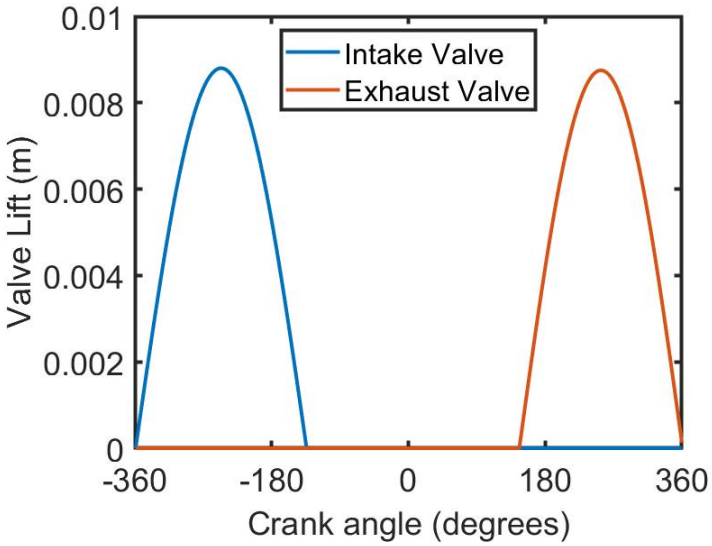

Figure A.3: Valve-lift in function of the crank angle.

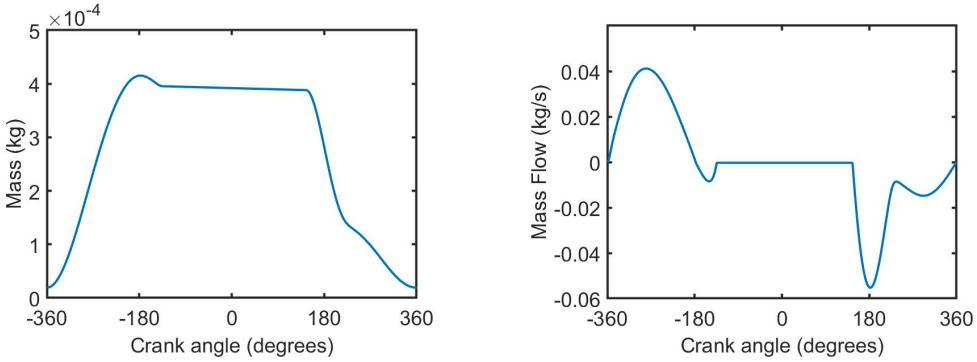

(a) Total In-cylinder Mass. (b) Mass Flow Rate.

Figure A.5: In-cylinder Mass: (a) Total; (b) Mass Flow Rate.

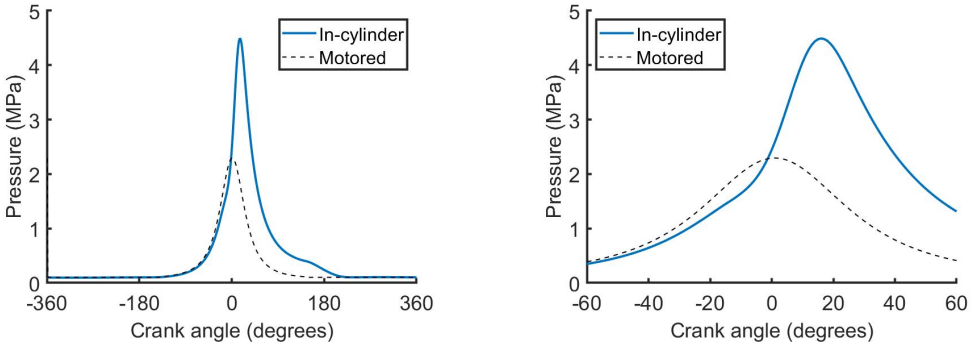

(a) In-cylinder Pressure. (b) In-cylinder Pressure Zoom.

Figure A.6: In-cylinder Pressure

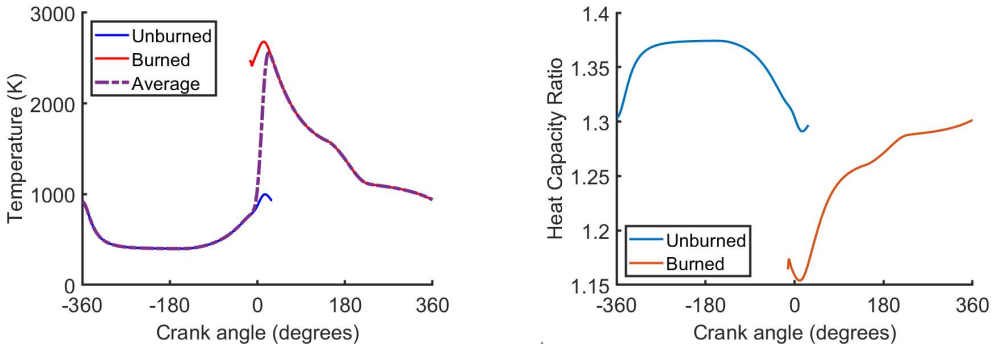

(a) In-cylinder Temperature. (b) Heat Capacity Ration.

Figure A.7: Temperature and Heat Capacity Ratio

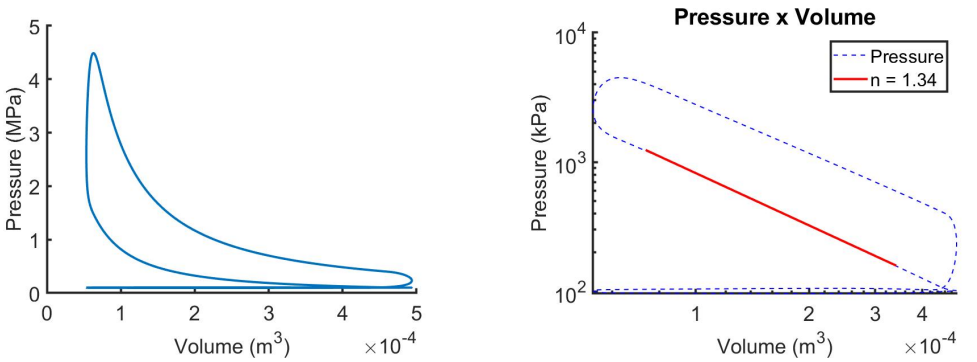

(a) Pressure vs. Volume. (b) Polytropic Coefficient.

Figure A.8: Pressure vs. Volume

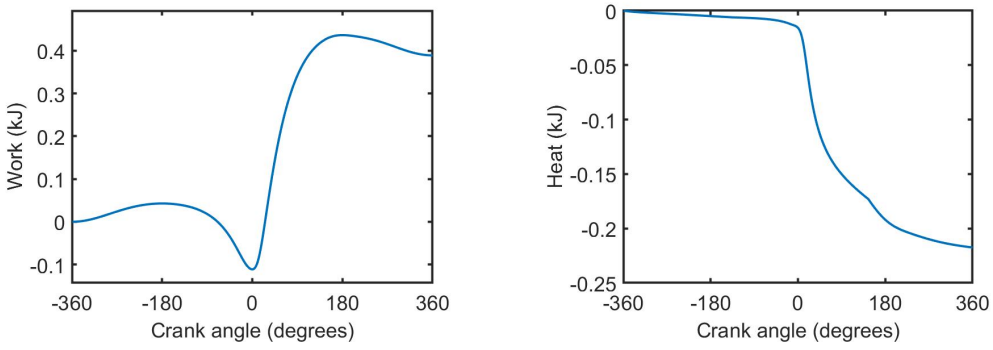

(a) Work. (b) Heat.

Figure A.9: Work and Heat

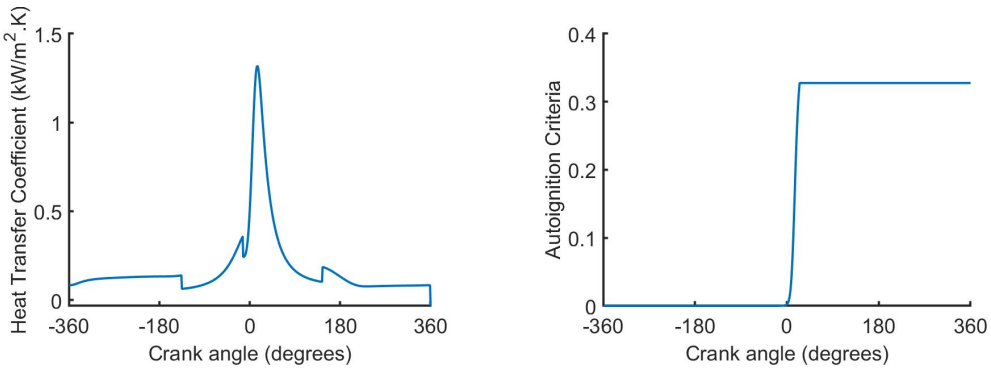

(a) Woschni Heat Transfer Coefficient. (b) Knock Integral.

Figure A.10: Heat Transfer Coefficient and Knock Integral

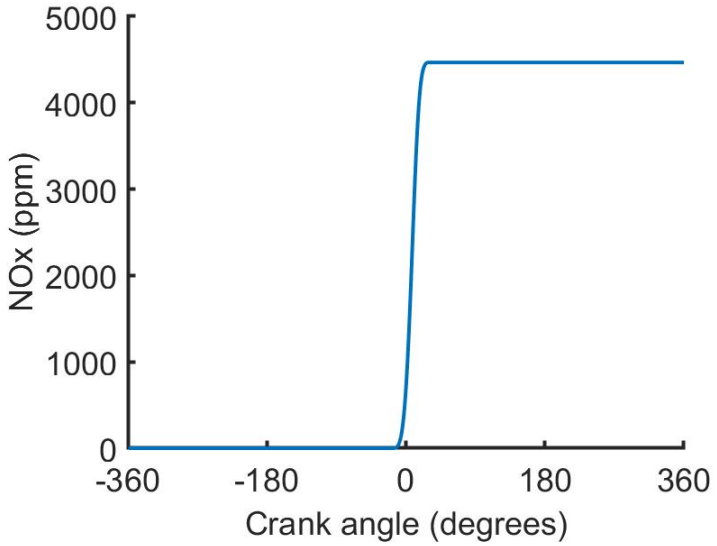

Figure A.11: NOx formation as a function of the crank angle.

B
Appendix B

With the same purpose of the Appendix A, the SACI model engine from TableB.1 was simulated. The geometry chosen was the same one of the SI engines to facilitate comparisons (CHALA; AZIZ; HAGOS, 2018). The results are ploted in this Appendix.

Table B.1: SACI Engine Specification Example

Geometric parameters	
Number of cylinders	4
Bore (mm)	83
Stroke (mm)	81.4
Half-stroke to Rod Ratio	0.271
Total Displacement Volume (cm^3)	1,761
Compression Ratio	18.0
Valves timing	
IVO	0ºaTDC
IVC	45ºaBDC
EVO	35ºbTDC
EVC	0ºaTDC
Operating point	
Engine speed (rpm)	3000
Fuel type	Natural gas
Equivalence Ratio (ϕ)	0.50
P_{int} (bar)	2.5
T_{int} (K)	380
T_{exh} (K)	480
Wiebe parameters	
a_W	6.9078
θ_s	-8ºaTDC
$\theta_{d,SI}$	46º
$m_{W,SI}$	3.20
$\theta_{d,HCCI}$	11º
$m_{W,HCCI}$	5.00

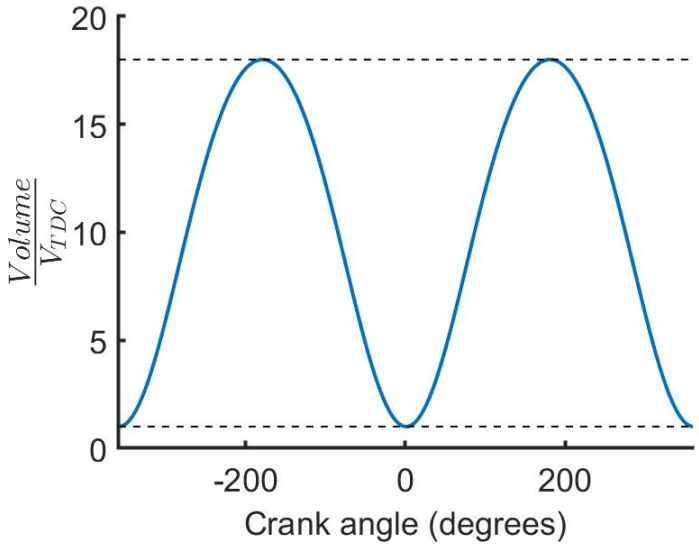

Figure B.1: In-cylinder volume in function of the crank angle.

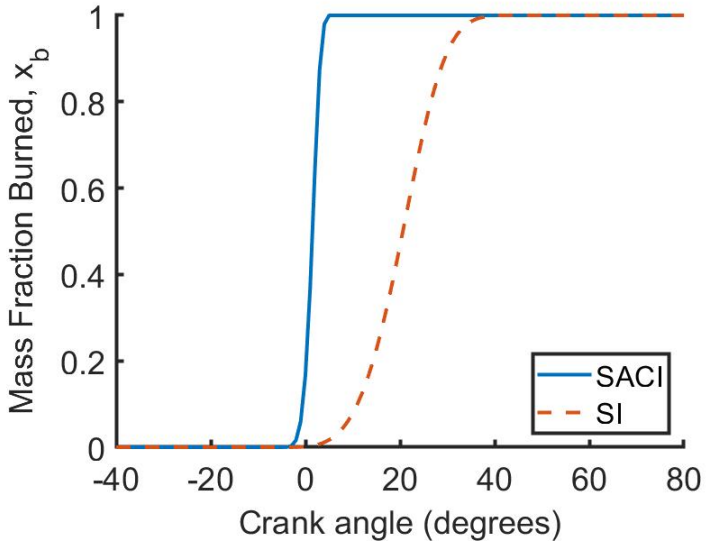

Figure B.2: Mass fraction burned in function of the crank angle.

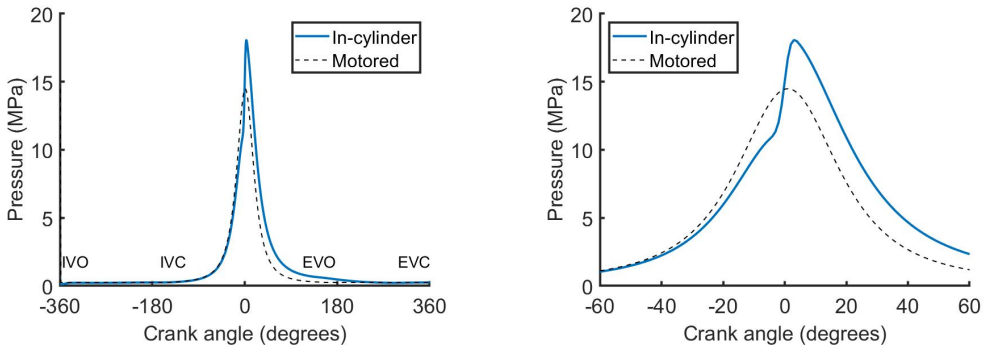

(a) In-cylinder Pressure.

(b) In-cylinder Pressure Zoom.

Figure B.4: In-cylinder Pressure

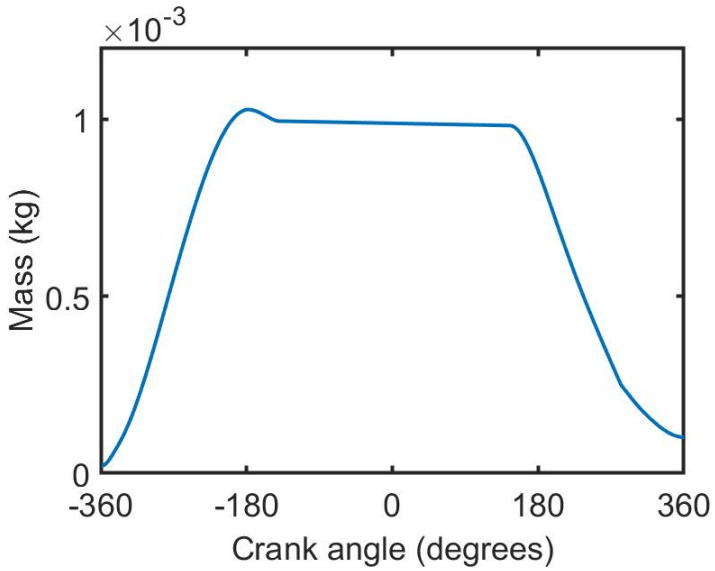

Figure B.3: In-cylinder Mass.

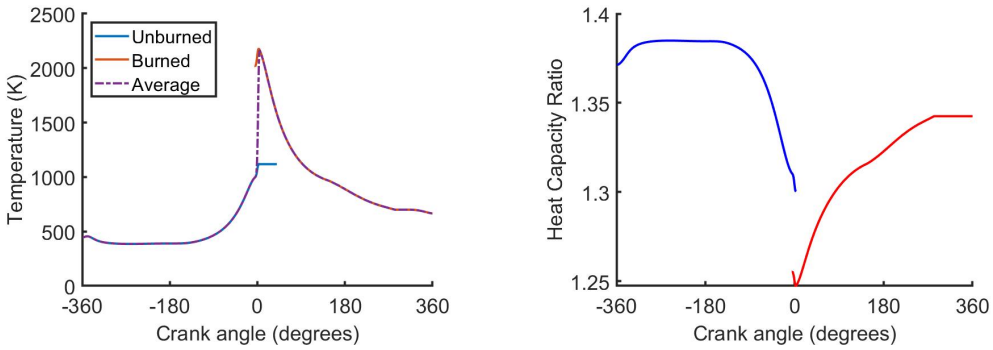

(a) In-cylinder Temperature. (b) Heat Capacity Ration.

Figure B.5: Temperature and Heat Capacity Ratio

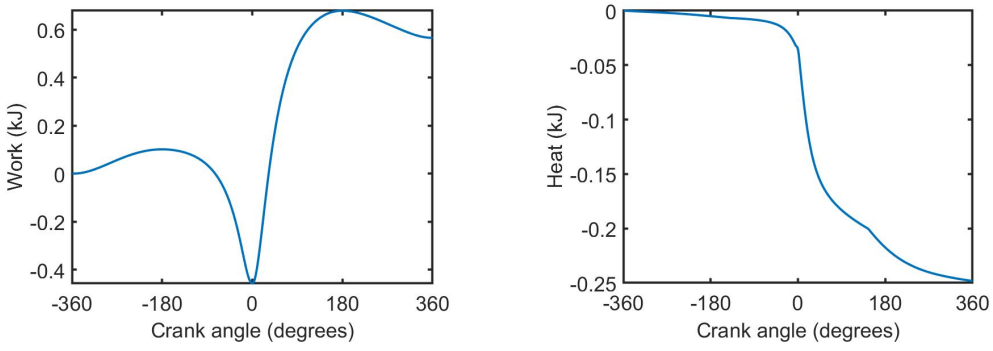

(a) Work. (b) Heat.

Figure B.7: Work and Heat

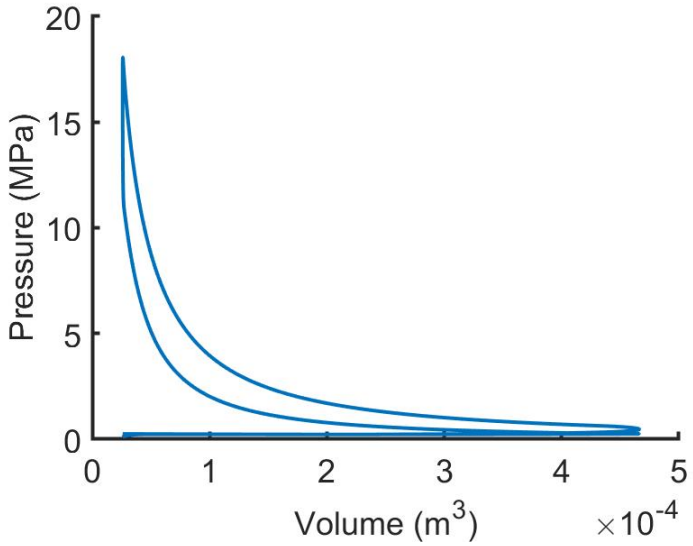

Figure B.6: Pressure vs. Volume.

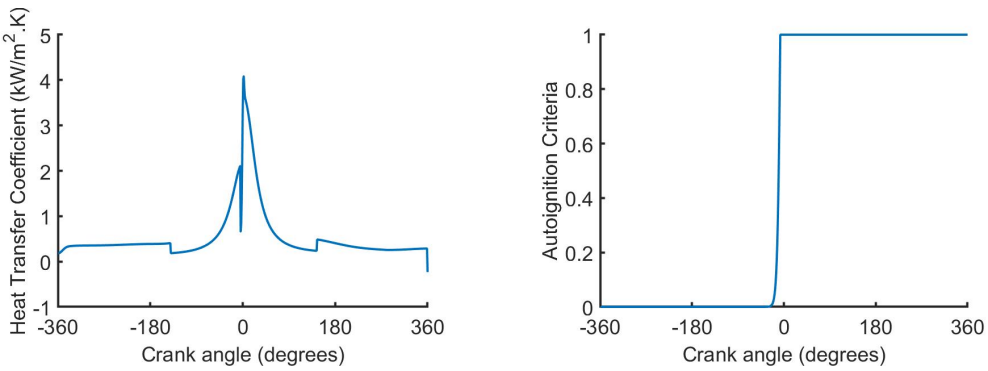

(a) Woschni Heat Transfer Coefficient. (b) Knock Integral.

Figure B.8: Heat Transfer Coefficient and Knock Integral

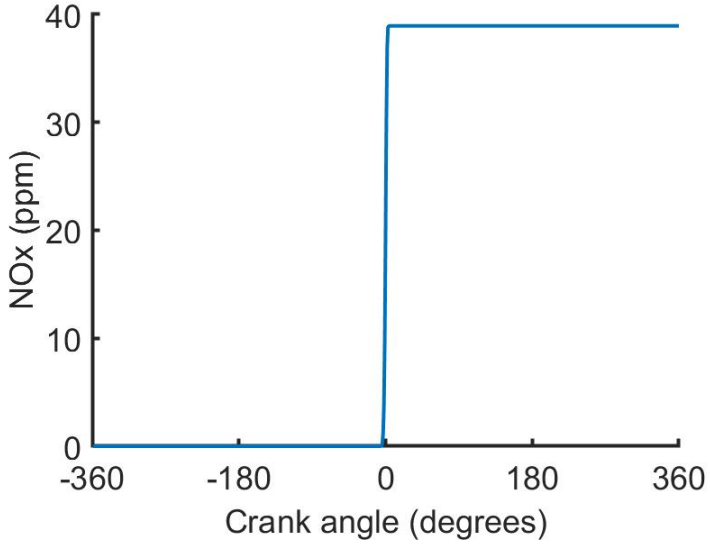

Figure B.9: NOx formation as a function of the crank angle.

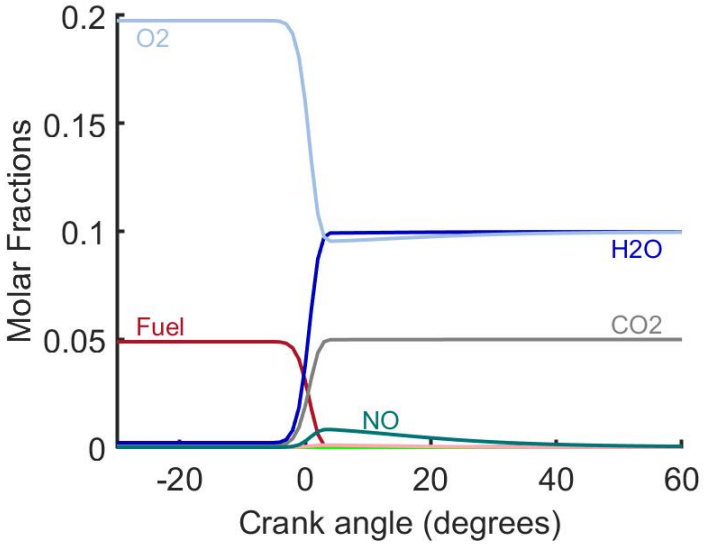

Figure B.10: Molar fraction as a function of the crank angle.